THEORETICAL IMAGE-FORMING QUALITY OF FAST-NEUTRON RADIOGRAPHY

A THESIS

Presented to

The Faculty of the Graduate Division

by

William Howard Wilkie

In Partial Fulfillment

of the Requirements for the Degree

Doctor of Philosophy

in the School of Nuclear Engineering

Georgia Institute of Technology

May, 1970

In presenting the dissertation as a partial fulfillment of the requirements for an advanced degree from the Georgia Institute of Technology, I agree that the Library of the Institute shall make it available for inspection and circulation in accordance with its regulations governing materials of this type. I agree that permission to copy from, or to publish from, this dissertation may be granted by the professor under whose direction it was written, or, in his absence, by the Dean of the Graduate Division when such copying or publication is solely for scholarly purposes and does not involve potential financial gain. It is understood that any copying from, or publication of, this dissertation which involves potential financial gain will not be allowed without written permission.

_____

_____

7/25/68

THEORETICAL IMAGE-FORMING QUALITY OF FAST-NEUTRON RADIOGRAPHY

Approved:

[redacted]

Date approved by Chairman: May 5, 1970

ACKNOWLEDGMENTS

I wish to express my sincere appreciation to my thesis advisor Dr. Don S. Harmer, Professor of Physics and Nuclear Engineering, for his invaluable assistance with the technical and administrative details associated with the research and preparation of the thesis.

I am also especially grateful to Dr. Paul B. Parks, Savannah River Laboratory, for his encouragement and assistance with the technical problems of the research and final editing. I wish to thank Professor Francis W. Chambers and Dr. Geoffrey G. Eichholz, who served as members of my reading committee, for their interest and useful suggestions at all phases of the work. Thanks are also due to Dr. Mark Brown for his assistance with the medical aspects of the research.

I am indebted to the following individuals for their willing advice and help with the use of various items of equipment: Mr. John C. Alderman, Jr., Dr. Robert H. Fetner, Mr. Marshall M. Cooksey, Mr. James E. Garrett, Mr. Jerry W. Segers, and Dr. T. P. Lang. I also appreciate the long-range assistance with the computer code 05R supplied by the Radiation Shielding Information Center and Dr. D. C. Irving at the Oak Ridge National Laboratory.

I am grateful to Dr. Carlyle J. Roberts for his patience and understanding. Thanks are also due to Mrs. Lydia S. Geeslin for her efficient typing and editing, to Mrs. Nelle S. McFather for her cheerful secretarial assistance, and to my graduate student friends whose fellowship was so important.

ACKNOWLEDGMENTS (Concluded)

I appreciate the financial assistance of the Ferst Foundation, the U. S. Public Health Service, and the U. S. Atomic Energy Commission. Special thanks are also due to Dr. Waverly W. Graham, III, for his financial help in the form of part-time employment and for his understanding of and sympathy for the problems of older graduate students.

Finally, I wish to thank my wife, who swapped a house and the Country Club for the "Halls of Ivy," and my children, who patiently waited for new bikes.

TABLE OF CONTENTS

TABLE OF CONTENTS (Continued)

TABLE OF CONTENTS (Concluded)

LIST OF TABLES

LIST OF ILLUSTRATIONS

LIST OF ILLUSTRATIONS (Continued)

LIST OF ILLUSTRATIONS (Concluded)

SUMMARY

Fast-neutron radiography is a virtually undeveloped method of obtaining visual images of the internal characteristics of thick materials. The usefulness of the technique will depend on the informational content and the quality of the visible image. In this research, these factors were examined theoretically for biomedical applications.

Various system components were discussed and judgments were made as to their suitability for radiographic applications. Each component of a radiographic system (radiation source, collimator, and imaging device), together with the object to be radiographed, affects the image-forming quality in a manner that can be quantitatively described using modulation transfer functions. These mathematical functions indicate the percent amplitude response as a function of spatial frequency.

Monte Carlo calculational techniques were used to predict the behavior of fast neutrons from the two most promising sources: 1) ^{252}Cf, and 2) the D-T reaction in a small accelerator. The interaction of neutrons from these sources with biological tissue and with system components was studied.

The validity of the use of modulation transfer functions for examining image-forming quality was established and the mathematical procedures used in the generation of these functions was explained. The modulation transfer functions provide a quantitative measure of the reduction in image-forming quality caused by finite source size, scattering in biological tissue, and multiple detection in the imaging device.

Dosimetry calculations were made for both types of neutron sources for both broad-beam and narrow-beam geometries. Isodose contours were presented for a right elliptical phantom of standard man composition tissue and for a phantom based on a realistic model of a human chest containing muscle, heart, lung, and bone tissues. The significance of these contours was evaluated in relation to neutron radiography, and the implications for the application of this type of calculation to neutron therapy were described.

CHAPTER I

INTRODUCTION

Objective

For many years radiography has played an important role in scientific, medical, and industrial fields. Diagnostic roentgenology is the most common and, generally, the most useful type of radiography, but beams of gamma, charged-particle, and thermal-neutron radiation are being used in complementary techniques for the extraction of information that is unavailable in attenuated X-ray beams. The characteristics of the images carried by radiation beams after penetration of an object depend on the mechanisms of interaction of the radiations with the object. These mechanisms differ greatly among the various radiation beams. A particular type of radiographic examination can be useful only if the technique results in images of sufficient clarity.

This investigation examines the image-forming quality that could be achieved by fast-neutron radiography of biological objects and determines the relative importance of scattered neutrons, geometric unsharpness, and detector characteristics on the quality of the image. A study is also made of the pattern of dose distribution in various biological phantoms so that dose limitations of fast-neutron exposure of living subjects may be determined.

Technological Justification

Background

Radiography is the production of a visible image in the three-step process of: 1) the generation of an appropriate beam of radiation, 2) the formation of a beam image defined by nonuniformities in the physical characteristics of the beam after penetration of an object, and 3) the transformation of the beam image into a visible image.

Radiography Using Photons and Charged Particles. All forms of radiography have the common purpose of visualizing some internal characteristic of an object, and it is useful to review the development of this technology. Roentgenographic images are formed when X-rays interact with electrons in the object. Therefore, X-ray images indicate differences in electron density. The usefulness of this type of radiography was quickly recognized by Röntgen, and many of the basic techniques for both medical and industrial applications were developed by him and his scientific contemporaries in the late 1890's and early 1900's [1,2,3,4].

Other forms of radiography serve generally as complementary procedures which are more useful in specialized situations such as the visualization of characteristics in materials that are opaque or homogeneous to X-rays, or where a high photon background would destroy the X-ray image on the photographic film, or whenever an object must be examined that requires the location of a radiation source in a position that is inaccessible to an X-ray tube.

Isotopic radiography using radium sources was also attempted [5,6] when the similarity between X-rays and gamma rays was recognized. How-

ever, isotopic radiography was not very practical until reactor-produced radioisotopes became plentiful. Isotopic sources have several advantages for radiographic applications. These are: 1) small physical size, 2) greater penetrability of the gamma-ray beam than is possible using conventional X-ray units, 3) smaller cost than X-ray units, and 4) independence from sources of electrical power and water. The disadvantages are: 1) generally lower intensity than conventional X-ray units, 2) short half-life and frequent replacement time, and 3) shielding and storage requirements when not in use. Generally, isotopic radiography is most useful for industrial applications but is also useful medically, especially in portable units. Russell [7] demonstrated that radiographs comparable to those from conventional X-ray sources can be produced using a portable isotopic unit weighing only a few pounds and employing a ^{109}Cd source of 70-mCi activity electro-deposited on the end of a two-millimeter diameter platinum rod.

Radiographic images also can be formed using beams of charged particles. Electron microscopy is the most common example, and an instrument of high quality can resolve dimensions as small as four to five angstroms (within a factor of two to four of the theoretical limit [8]). Another type of electron radiography produces an image on photographic film as a result of the photoelectrons ejected from the surface of the object by x-radiation from tubes operating at 100 to 200 kV [9].

Proton radiography is useful in specific applications where a very high contrast is required over a small range of thickness variation. Even though this is an extremely sensitive method, it is of

limited utility because the proton beam must be produced by a high-energy accelerator. The basic techniques are described in the recent work by Koehler [10] at Harvard and Bell [11] at Harwell. Bell showed that area density fluctuations as small as two to three parts in 10^5 could be detected over an area of 0.5 mm diameter using a cyclotron beam of 147-MeV protons. This sensitivity is two orders of magnitude better than standard methods based on the transmission of radiation from isotopes or X-ray units [11]. The same technique could be used with alpha particles, but no advantages over proton radiography are foreseen.

Neutron Radiography. To a first approximation, the primary difference between radiography with photons or charged particles and neutron radiography is that photon and charged-particle beams are modulated by differences in electron density while neutron beams are modulated by differences in the specific nuclide density. At thermal energies the total cross sections for different nuclides range over more than six orders of magnitude. Therefore, it is physically possible to contrast very small amounts of nuclides having high cross sections in the presence of large amounts of nuclides having low cross sections.

Kallmann [12] initiated the method of thermal-neutron radiography and summarized the most useful principles of detection. Peter [13] also contributed to the early development using a moderated, accelerator source of neutron. Thewlis [14] extended the technology and showed that adequate beams of thermal neutrons were available from existing nuclear reactors. Despite these advances, an active interest in neutron radiography did not develop until the early 1960's with the work of Berger [15], Watts [16], Radwan and Sikorska [17], and Greenfield and

Koontz [18]. With this new impetus, the technology began to expand rapidly and is currently a very useful tool, particularly for the industrial inspection of plastics and organic materials shielded by metal for which x-radiography would be limited and where the high neutron interaction with hydrogen offers a particular advantage. The reader who is interested in this technique is referred to the summary on the subject by Berger [19]. Atkins [20] and recently Brown and Parks [21] and Brown et al. [22] have demonstrated the potential of thermal-neutron radiography in the field of medical research. Thermal neutrons interact more strongly with hydrogen than any other element in biological materials, and therefore images produced with this method indicate variations in hydrogen density of the various tissues. The most significant limitation of this application for thermal neutrons is the short mean free path which prevents the radiographic examination of tissue with thicknesses over several centimeters.

Neutron beams having energies other than thermal have been used in radiography, but these techniques have been of limited usefulness due to one or more of the following factors: 1) difficulty in obtaining a neutron beam of sufficient intensity, 2) limitations due to the physics of the neutron interaction with the object, or 3) lack of a suitable image converter. Most of the effort in this area has been due to Barton's use of both epithermal and cold neutrons. He demonstrated the essential characteristics of epithermal-neutron radiography using 1.4-eV neutrons obtained by diffracting a collimated neutron beam from a nuclear reactor with a large aluminum crystal. This energy was selected because it corresponds to a large resonance peak in indium which

was used as an image converter [23]. A comparison of this technique with thermal-neutron radiography indicated the following advantages: 1) increased penetration due to lower cross sections for most elements, 2) very high contrast for certain nuclides at their resonance energies, 3) the reversal of the order of attenuation between some pairs of elements at epithermal energies compared with thermal energy, 4) possibility of identification of elements having resonance structure by observing their opacity as a function of energy, 5) high selectivity of image converter foils when the energy of the neutron beam is tuned to a resonance frequency, 6) enhanced quality of the radiograph due to reduction in the contamination of the beam by neutrons of other energies and by gamma rays. Spowart [24] has confirmed the advantages of epicadmium neutrons for radiography of materials having high thermal cross sections such as uranium-235 and plutonium.

Barton [25] also demonstrated the technique of radiography with cold neutrons having energies below 0.005 eV. These neutrons were obtained by filtration of a reactor beam using beryllium with bismuth as a gamma shield. This work demonstrated that: 1) increased contrast is obtained for hydrogen and many other elements, 2) the penetration for iron is increased due to the sharp drop in cross section below 0.005 eV, 3) the interference of scattered neutrons is reduced to negligible proportions, and 4) thicknesses less than 0.05 inch of hydrogenous material can be resolved through up to four inches of mild steel.

Relatively little radiography has been attempted using fast neutrons due partly to the necessity of an appreciable investment of effort in development before useful results could be obtained, and also

to indications that fast neutrons would not be useful for differentiation between elements because of the small variations of total cross section. Kallmann [12] made the first fast-neutron radiographs in the late 1930's using a neutron generator as a source and using a layer of paraffin and scintillator adjacent to a photographic film as a detector. The next experimental work was reported in 1961 by Criscuolo and Polansky [26] on the applicability of 14-MeV neutrons for the radiography of large masses of material. Exposures were made of copper, iron, lead, aluminum, paraffin, and masonite using Patterson Type D fluorescent screens and Kodak Type KK X-ray film with one half inch of lead as an X-ray filter.

Anderson et al. [27] reported on the response of X-ray film used for the radiography of two human subjects with 14-MeV neutrons. Although certain anatomical features could be distinguished when ZnS or Fluorazure screens were used with the film, no attempt was made to determine what portion of the observed response was due to primary neutrons and what was due to scattered neutrons and photons.

Tochilin [28] analyzed the feasibility of using photographic film for the detection of fast neutrons and discussed the limitations and difficulties of fast-neutron radiography in general. A series of radiographs was made of cylinders of plastic, Al, Cu, and Pb having holes of varying diameters and depths. Fast neutrons were obtained from the interaction of cyclotron-produced protons or deuterons with a thick Be target. Exposures were made using Kodak Type K and DuPont Type 502 film both with and without plastic scintillator screens for intensification and with varying thicknesses of lead absorbers in front of the

test objects. It was concluded that the buildup of scattered neutrons and gamma rays would prevent successful radiography of material thicker than a few inches if a film-screen technique were employed. In order to eliminate gamma-ray interference and to minimize the effects of scattered neutrons, a transfer technique was tried using the threshold reaction $^{32}S(n,p)^{32}P$. This method was successful but was considered impractical due to the excessively high exposures required. Organic scintillators were judged to offer the best promise as intensifying screens.

Wood [29], using a neutron generator (D-T reaction), found that organic scintillators and copper transfer foils did not give adequate sensitivity with photographic film. The best results were obtained with a Radelin TI-2 screen and Kodak Royal Blue film. It was further concluded that the resolution was limited more by proton recoils in the emulsion and by small-angle scattering of neutrons in the objects than by geometric unsharpness or screen resolution.

Fast-Neutron Technology

The current research is motivated by an interest in studying the feasibility of using fast-neutrons for the radiographic diagnosis of human disease. It has been shown by Parks et al.[30] that low-density tissues shielded by bone, difficult to visualize with X-rays, can be contrasted to some extent with fast neutrons. Radiography with fast neutrons also could prove useful because the long mean free path (~ 10 cm at 14 MeV) of fast neutrons in biological media allows the examination of thick samples.

There is currently an active interest in the use of fast neutrons

for cancer therapy [31]. Many of the technical developments of fast-neutron radiography such as improvements in beam definition, shielding, dosimetry, and adequate source strength are applicable to the technology of fast-neutron therapy. The calculations presented in Chapter V for the dose of both broad and narrow beams of fast neutrons are particularly germane to therapy. It should be noted that the techniques used in these calculations can be extended to particular geometries characteristic of specific therapeutic applications.

Plan of Attack

Possible components for a fast-neutron radiography system are reviewed from the standpoint of their suitability for medical diagnostic purposes. Various sources are examined against the criteria of neutron energy distribution, cost, availability, source strength, and beam contamination. Collimation and shielding techniques are reviewed and detector systems are examined for efficiency and background discrimination.

The evaluation of the image-forming quality of radiographic systems through the use of modulation transfer functions is explained, and the equations for this technique are derived.

Monte Carlo calculational techniques are discussed as they apply to estimates of fast-neutron radiographic performance. The validity of the calculational approach is established for predicting neutron penetration and dosimetry, and procedures are developed for calculating detector response, line-spread functions, modulation transfer functions, and dosimetry. Calculations are evaluated and compared with experimental results where these are available.

CHAPTER II

REVIEW OF SYSTEM COMPONENTS

Sources of Fast Neutrons

Many different sources of fast neutrons are available [19,32, 33,34,35,36]; they may be generally classed as isotopic, accelerator, or reactor sources.

Isotopic Sources

Neutrons from these sources are produced by the reactions (α,n), (γ,n), and spontaneous fission, but photoneutron sources can be eliminated from consideration immediately because these sources do not produce neutrons having energies as great as one MeV [35]. (The most common type ^{124}Sb-Be emits neutrons of 24 ± 3 keV.) Sources of the (α,n) type are intimate mixtures of an alpha emitter and beryllium metal powder. High-yield sources of this type are impractical because of their gamma-ray emission, heat emission, volume, half-life, or cost. Gamma-ray backgrounds from these sources range from 6000 mR/hr at one meter per 10^8 n/sec for ^{226}Ra-Be to four mR/hr at one meter per 10^8 n/sec for ^{210}Po-Be [32].

Californium-252 is an intense spontaneous-fission neutron source whose emission rate is 300 times greater than any other isotopic source currently available [36]. Figure 1 shows a comparison of the energy distribution of neutrons from the fission of ^{252}Cf and ^{235}U [37]. The average energy of the ^{252}Cf neutrons is 2.3 MeV, which is slightly higher

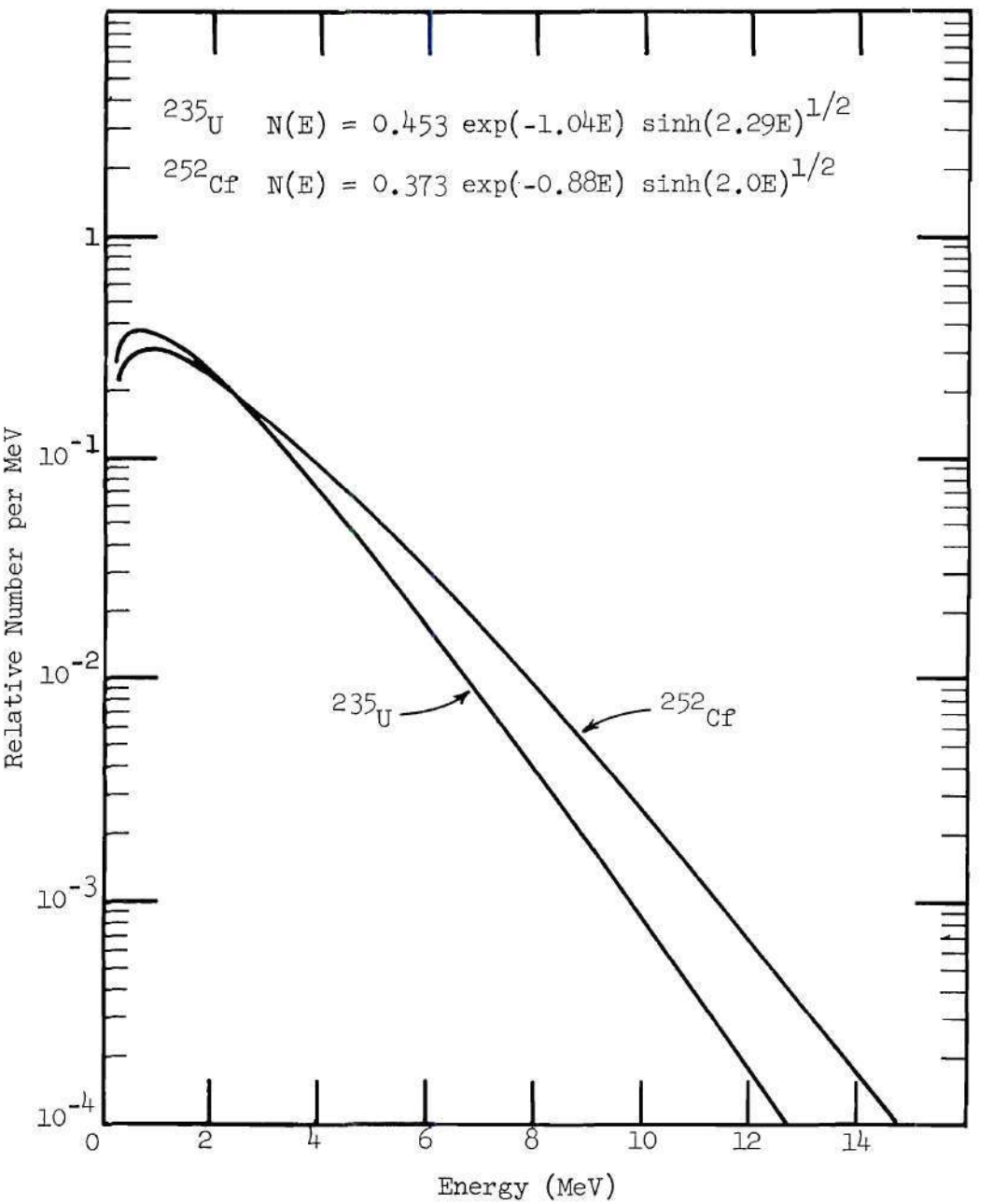

Figure 1. Energy Distributions of Neutrons from Fission of ^{235}U and ^{252}Cf

than the average for ^{235}U of 2.0 MeV. Californium-252 has a high specific yield of 2.34×10^{12} n/sec-gm, and the half-life of 2.65 years is reasonably long. Several advantages of this source make it particularly promising for applications in both fast and thermal-neutron radiography. No additional target material is required, which reduces both the fabrication cost and the volume of the source. It is technically feasible to produce ^{252}Cf sources having high yields but occupying very small active volumes. Table 1 provides a comparison of the yield, cost, half-life, gamma dose rate, heat generation, and probable volume of the various isotopic neutron sources.

Accelerator Sources

Either positive ions or electrons may be accelerated to produce neutrons through the (d,n), (p,n), (α,n), or (γ,n) reactions. The most common reaction and the most useful for fast-neutron radiography is the $^{3}H(d,n)^{4}He$ reaction because: 1) it has a high cross section and therefore a high yield per deuteron ion, 2) a relatively inexpensive accelerator can be employed because the minimum required deuteron energy is about 140 keV (yields of between 10^{10} and 10^{11} n/sec are obtained from machines that cost less than $30,000 when fully operational), 3) neutrons are produced that are nearly monoenergetic and are emitted nearly isotropically. Figure 2 shows the energy of neutrons calculated from the nonrelativistic Q equation as a function of angle for 200 and 400 keV deuterons bombarding an infinitely thin target.

Tritium targets are usually fabricated by diffusing tritium gas into a titanium film that has been vacuum evaporated onto a thin copper disc. Because deuterons of a few hundred keV penetrate only about one

Table 1. A Comparison of Fast-Neutron Sources[a]

Source	Type	Half-Life	Avg. Energy (MeV)	Yield n/sec-Ci	Cost ($) 5×10^{10} n/sec	Gamma Dose Rate (rads/hr @ 1 m per 5×10^{10} n/sec)	Heat Generation (watts)	Approx. Volume (cm^3)
^{252}Cf	S.F.	2.65 y	2.3	4.4×10^{9}	10,700[b]	2.9	0.8	1
^{226}Ra-Be	α,n	1620 y	3.6	1.5×10^{7}		3000[c]		
^{242}Cm-Be	α,n	163 d	4.0	4.0×10^{6}	10,000	0.3	600	2
^{244}Cm-Be	α,n	18.1 y	4.0	3.0×10^{6}	280,000	0.2	600	70
^{238}Pu-Be	α,n	89 y	4.0	2.8×10^{6}	310,000	0.4	550	350
^{210}Po-Be	α,n	138 d	4.3	2.5×10^{6}	20,000	2.0	640	200
^{241}Am-Be	α,n	458 y	4.0	2.0×10^{6}	1,500,000[d]	2.5	750	22,000
^{239}Pu-Be	α,n	24,400 y	4.5	2.0×10^{6}		85[c]		

[a] Reinig [36]

[b] Seaborg [38]

[c] Corompt [32]

[d] Based on the cost of small sources

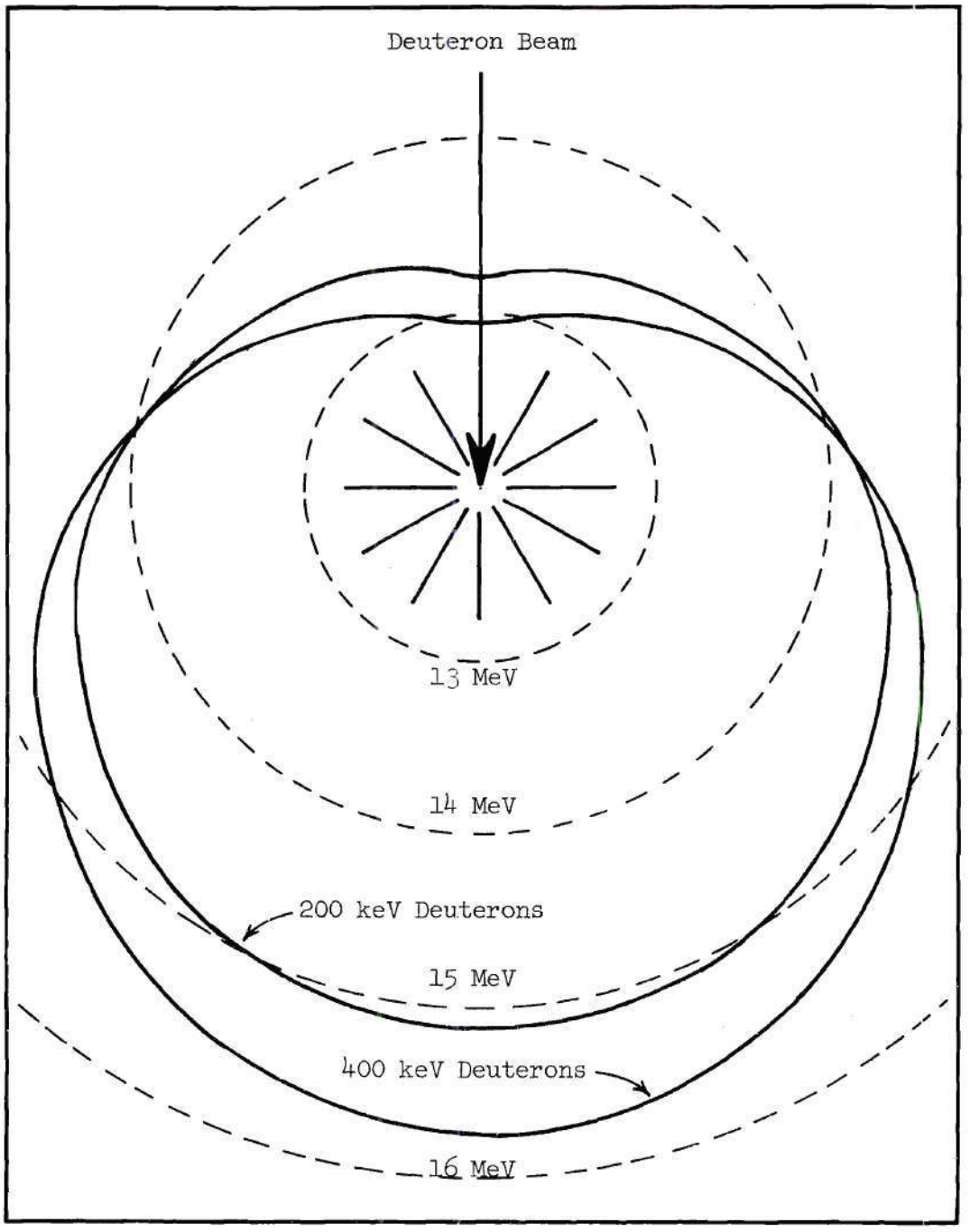

Figure 2. Energy of Neutrons Produced in the D-T Reaction as a Function of Emission Angle

micron into the titanium, the target is infinitely thick and neutrons emitted at a given angle have all possible energies from the calculated thin-target energy to the threshold energy of 14.1 MeV. For a deuteron energy of 400 keV the neutrons emitted in the forward direction will have energies between 14.1 MeV and 15.7 MeV.

The disadvantage of this type of neutron source involves target cooling and target lifetime. Higher yields cannot be obtained with the type of targets that are generally available because of: 1) the high rate of heat generation in the target, and 2) the related outgassing and sputtering with the high ion currents. Recent progress [39] in target design make yields in the order of 10^{12} n/sec possible with target lifetimes in the order of hundreds of hours instead of the several hours generally obtainable at present. Some of the techniques under development are: 1) the rotating annulus target analogous to X-ray tubes, 2) sealed accelerator tubes containing a mixture of deuterium and tritium gases, 3) the mixed-beam approach with unsealed tubes, and 4) the neutron-gun approach based on a plasma of D + T gas that results in a pulsed source. Greene and Thomas [40] have reported the use of a sealed tube containing a D + T gas mixture which is replenished by heating the hydride of the gas in a recharging unit built into the tube. A layer of erbium containing a chemically bound D + T mixture is the target. Several of these tubes which are being developed by the Services Electronic Research Laboratory (England) have been operated in excess of 100 hours at an output of approximately 10^{10} neutrons per second.

Another exoergic reaction $^{2}H(d,n)^{3}He$ with a Q-value of 3.266 MeV

may be employed with the same equipment necessary for the D-T reaction. This reaction is useful for producing neutrons in the 2.6-MeV range, but the yield for deuteron energies up to 500 keV is more than a factor of 10 lower than the D-T reaction and, hence, may be of marginal intensity for radiography purposes. Other accelerator neutrons may be obtained from the $^{7}Li(p,n)^{7}Be$ or $^{3}H(p,n)^{3}He$ positive ion reactions or the $^{9}Be(\gamma,n)^{8}Be$ and $^{2}H(\gamma,n)^{1}H$ reactions resulting from electron bombardment and subsequent bremsstrahlung production in the target. These reactions require the more expensive high-energy machines and, hence, are of limited utility for radiography.

Reactor Sources

Reactors are the most prolific sources of neutrons that can be used for radiography. While they have the common disadvantages with high-energy accelerators of high initial cost, large operating expense, and immobility, reactors have the advantage of being usable for radiography with little interference with concurrent experiments.

Two possibilities exist for the development of a fast-neutron radiography facility at a reactor: 1) a fast-flux beam tube which views a fuel element in the core with few moderating materials intervening, and 2) a small fission converter plate which can be introduced into a thermal beam. The fission mean free path for ^{235}U is about 0.36 mm, and thus, a uranium plate between one and two-mm thick would convert essentially all the thermal neutrons that strike it. Therefore, the maximum fast-neutron yield that could be obtained would be the product of the plate area, the thermal flux density, and the conversion factor of 2.5 n/fission for ^{235}U. Because the yield is directly proportional

to the plate area, the maximum yield is obtained by using the largest plate the facility will accommodate. However, this approach to the problem of obtaining adequate source intensity is untenable from radiographic considerations. Not only must the source intensity be high in order that the time of exposure can be short, but the total unsharpness of the radiographic system must be low enough so that the image definition will be adequate.

Unsharpness is the smearing of the image which means the extent to which sharp boundaries in the object do not appear sharp in the image. All parts of the system contribute to the observed unsharpness, but geometric unsharpness, the reduction in contrast generated by geometric beam problems, tends to predominate.

Geometric unsharpness or penumbra U_F is caused by finite source dimensions. Its exact form depends on the shape of the source and its differential emission rate. Geometric unsharpness is so named because of the optical analogy of shadow formation. If a large object is interposed between a radiation source of finite size and a detector plane, the image will be formed by: 1) a "black" area where all parts of the source are obstructed by the object, 2) a "light" area where no part of the source is obstructed by the object, and 3) by the boundary between the "black" and "light" areas. Geometric unsharpness is usually reported as the width of the "gray" boundary. The same type of unsharpness will be seen for the visualization of inclusions within the large object. A point in the object is imaged as an area whose maximum dimension is the value of the geometric unsharpness. In order to image certain features of an object, a design restriction can be placed on the unsharpness

prior to the development of the facility. If the geometric unsharpness U_F for the reactor converter-plate facility illustrated in Figure 3 is judged to be acceptable, then any converter plate that fits within the cone above the object will give acceptable values of geometric unsharpness. If converter plate (1) has an area of

$$A_1 = \pi \left(x_1 \tan \frac{\theta}{2} \right)^2 \tag{2.1}$$

and a total fast-neutron yield of KA_1 where K is 2.5 times the thermal flux density at the position of the plate, then the neutrons which contribute to imaging the object point will be

$$N_1 = \frac{KA_1}{4\pi x_1^2} = \frac{K \tan^2 \theta/2}{4} \tag{2.2}$$

If a larger converter plate (2) having an area of

$$A_2 = \pi \left((x_1 + x_2) \tan \frac{\theta}{2} \right)^2 \tag{2.3}$$

and a yield of KA_2 is positioned at a distance of $x_1 + x_2$ from the object point, the geometric unsharpness determined by θ and x_o will be the same as for plate (1). The fast-neutron yield has been increased by the factor

$$\frac{(x_1 + x_2)^2}{x_1^2} \tag{2.4}$$

but the neutron flux density N_2 contributing to the formation of the

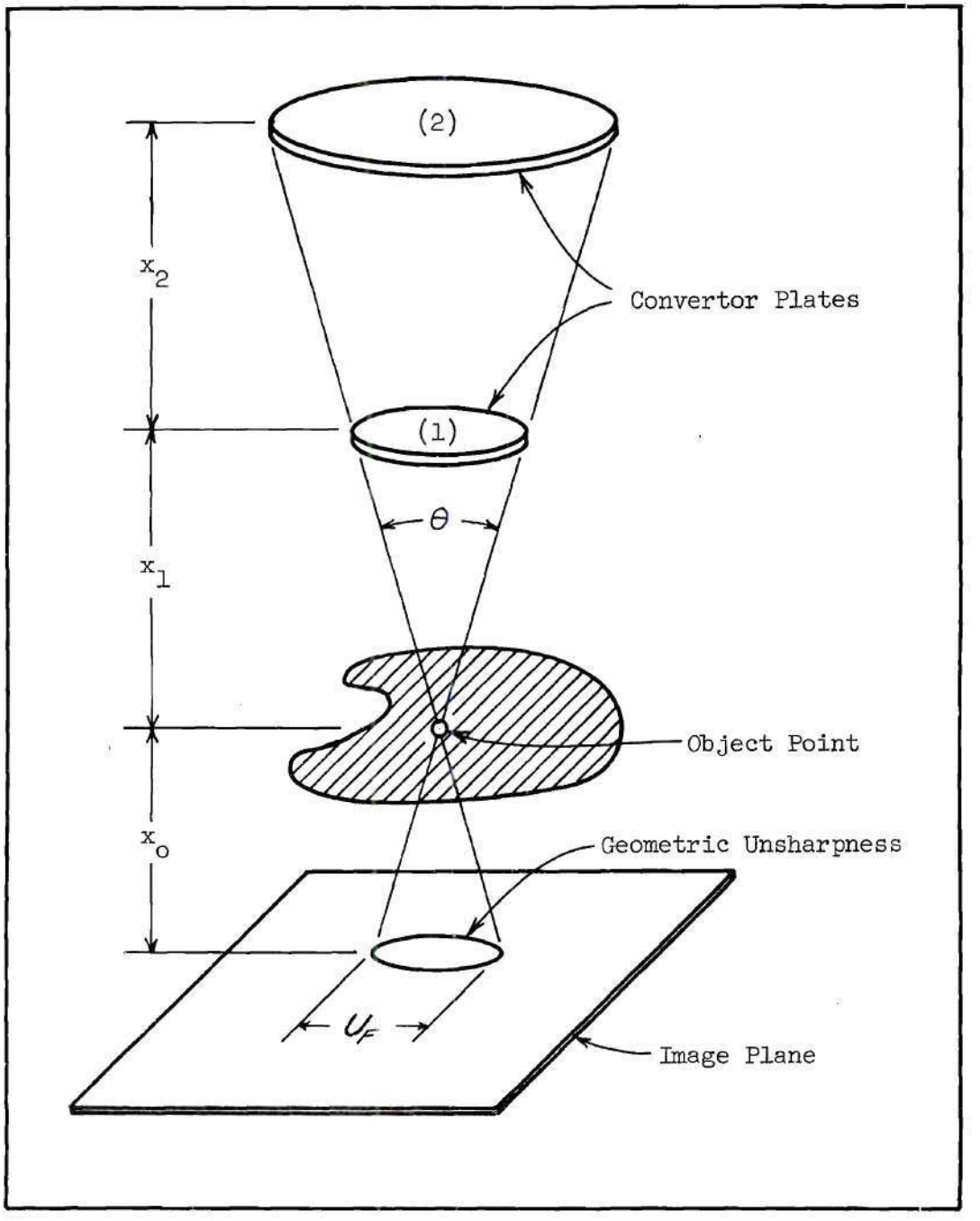

Figure 3. Geometric Unsharpness from Convertor-Plate Sources

image has remained unchanged because

$$N_2 = \frac{K\pi((X_1 + X_2)\tan\theta/2)^2}{4\pi(X_1 + X_2)^2} = \frac{K\tan^2\theta/2}{4} = N_1 \qquad (2.5)$$

Therefore the ultimate limitation on fast-neutron intensity is the thermal flux density at the position of the plate.

A major difficulty with this type of source is the large gamma-ray fields associated with most beam facilities. If the fast neutrons are obtained by viewing the reactor core directly, an additional difficulty would be the beam contamination from neutrons having energies of less than 500 keV.

Comparison of Sources

In conclusion we may make several generalizations concerning isotopic, accelerator, and reactor sources. A small accelerator producing neutrons by the D-T reaction is a reasonable choice of source size if high-energy neutrons are required from considerations of adequate penetration of the object or from considerations of detector response. For the same reasons, a fission spectrum may be more useful for some applications. Except for availability, reactor sources offer no advantage, and a ^{252}Cf source is also a better choice because point-source conditions can be approximated closely.

At the present time ^{252}Cf is expensive and in limited supply. The United States Atomic Energy Commission (AEC) price at the Oak Ridge National Laboratory is $100 per 0.1 microgram with a 1.0 microgram limit per purchaser [41]. However, it is estimated that, after the first production run of 1969-1970 at the Savannah River Plant, 1.0 to

2.5 grams of ^{252}Cf could be made available at a unit price of $15 to $25 per microgram, and by the early 1980's several hundred grams per year could be produced for sale at approximately one dollar per microgram [41].

From an economic standpoint accelerators and californium-252 would then be about equivalent on a capital investment per neutron basis except for the case in which a continuous source is needed. Then ^{252}Cf would be a better investment. Operating expense and maintenance are considerably greater for accelerators.

Collimation and Shielding

The need for collimation and shielding for fast-neutron radiography arises from practical considerations of beam definition, minimization of scattered neutrons, and personnel protection. These problems are neither simple nor straightforward. Beam definition can result in severe contamination of the beam from scattered neutrons which have lower energy and random direction, and the angular distribution pattern of the neutrons becomes complex.

Collimator design is more difficult than bulk-shield design because, for a specific application, there is an optimum combination of geometric arrangement, collimator dimensions and shape, and material composition. For this reason, few collimator studies have resulted in useful generalizations. Straker [42] has reviewed the results of several studies and summarizes the significant results as follows: 1) the liner contributes the most to the scattered flux for long collimators, 2) the scattering is strongly influenced by the choice of lining

material with iron being a better choice than lead or carbon, 3) the collimator should be tapered at both the source and detector ends, and 4) there exists an optimum location for the collimator position relative to the source and detector. With Monte Carlo techniques (05R computer code) Straker analyzed the effects of collimator shaping and lining material on the origin and magnitude of the scattered and transmitted components of the neutron flux for a distributed source and a 2.0-cm detector. These results demonstrated that: 1) for a long cylindrical collimator, most of the scattered component is due to events near the entrance and exit of the collimator, 2) nearly all of the transmitted component enters the air column through the shield near the source, 3) hyperboloid shaping (this shape may be approximated by several conical sections) at the entrance and exit of the collimator can produce a factor of five improvement in the ratio of background fluence to direct fluence, and 4) iron or polyethylene in one eighth inch thicknesses is a better choice of lining material than either lead or aluminum.

It should be emphasized that the restraints placed on the system by the requirements for a particular application will influence the optimum design. For biomedical applications the three most restrictive requirements are those specifying depth-dose characteristics, field size, and acceptable dose rate. For instance, for the clinical application of fast-neutron therapy, the current consensus is [31]: 1) from considerations of treatment time the minimum acceptable dose rate is 10 rads/min with no phantom, 2) from considerations of the dose to healthy tissue the minimum acceptable depth for 50 percent of the surface dose is 10 cm, and 3) the smallest field size (dimension of the

beam at the surface) of clinical interest is five cm. A source-to-skin distance (SSD) of about 125 cm [31] for 14 MeV neutrons appears to meet the second requirement. A source having a minimum intensity of 5×10^{12} n/sec would be necessary in order to meet the first requirement. (This combination of source, SSD, and field size is discussed in Chapter V, section Dosimetry Calculations.)

Two experimental arrangements of biomedical interest are those of Greene and Thomas [40] and Lawson and Watt [43]. Lawson and Watt used a 5.0-cm diameter by 60.5-cm long collimator, an SSD of 75 cm with a 14-MeV generator target shielded by ^{10}B-loaded polythene. Their results based on isodose curves in a 20 x 30-cm right elliptical cylinder with a 16.4 x 16.4-cm field were less than satisfactory. The beam appeared to be very nonuniform with a surface dose ranging from 100 percent at the centerline to 60 percent at the edges.

Greene and Thomas used conical collimators and a 50-cm SSD with a 14-MeV generator target inside a steel shield. Their beam definition was adequate and the results for a 10 x 10-cm field indicated a drop in dose of about 10 percent from the centerline dose at 1.8 and 10 cm depths. Additional experimental evidence on the effectiveness of iron collimators for 14-MeV neutrons has been presented by Rosen and Stewart [44].

Imaging

Object Contrast

The relative opacity of the object can be predicted from physical theory, and hence an estimate may be made of the maximum amount of information that could be extracted from a transmitted beam.

In order to visualize an inclusion in biological objects, there must be a difference in the absorption of the primary radiation along paths that traverse the inclusion compared with adjacent paths that do not traverse the inclusion. This difference can be expressed as object contrast C (sometimes referred to as subject contrast) given by [45]

$$C = \frac{\psi_x - \psi_a}{\psi_x + \psi_a} \tag{2.6}$$

where ψ_a and ψ_x are respectively the total primary fluences that have and have not passed through the inclusion. (The object contrast, which is independent of the method of detection, should not be confused with the radiographic contrast defined as the absolute value of the difference between the photographic densities of two areas on a visible image.) In the case of a monoenergetic source such as 14-MeV neutrons the object contrast may be expressed in terms of the total linear attenuation coefficients μ_a and μ_x as [30]

$$C = \frac{1 - \exp\left[(\mu_x - \mu_a)a\right]}{1 + \exp\left[(\mu_x - \mu_a)a\right]} \tag{2.7}$$

where a is the thickness of the inclusion. Note that the object contrast does not depend on the overall thickness x of the object. In the case of air inclusions, where μ_a is negligible, Equation 2.7 is

$$C = \frac{1 - \exp\left(\mu_x a\right)}{1 + \exp\left(\mu_x a\right)} \tag{2.8}$$

and, in the special case where μ_x and μ_a are nearly equal, Equation 2.7

reduces to

$$C = \tfrac{1}{2}(\mu_x - \mu_a)\, a \qquad (2.9)$$

If the composition of the various tissues and the total neutron cross sections are known, then the linear attenuation coefficients may be calculated and the ideal object contrast determined from Equation 2.7. For 14-MeV neutrons the linear attenuation coefficients for fat (μ_f) and muscle (μ_m) are

$$\mu_m = 0.096 \text{ cm}^{-1}$$
$$\mu_f = 0.097 \text{ cm}^{-1} \ *$$

which means that fat and muscle cannot be contrasted with 14-MeV neutrons. On the other hand, the composition for bone in humans varies greatly among the different types of bone tissue and among the different bones. In the literature the composition for wet cortical bone is most often reported because this tissue is more uniform than is the spongiosa [46]. However, even the composition of cortex shows wide variability. Table 2 shows a comparison based on three of the more reliable determinations.

For the calculations in the current research, bone is assumed to be 50 percent cortex and 50 percent marrow with a linear attenuation coefficient of 0.108 cm^{-1}. The linear attenuation coefficients for 60-keV and 1-MeV X-rays in muscle and bone are**

---

*See Appendix A for the elemental compositions of muscle and fat.

**Calculated using X-ray attenuation coefficients from NBS Circular 583 [47] and the tissue compositions in Appendix A.

Table 2. Elemental Composition of Bone and Linear Attenuation Coefficients for 14-MeV Neutrons

Element	Percent by Weight			
	A	B	C	D
Hydrogen	3.42	6.4	7.9	7.6
Carbon	15.5	27.8	33.0	16.7
Nitrogen	4.0	2.7	3.6	3.7
Oxygen	44.1	41.0	39.0	52.2
Phosphorus	10.2	7.0	6.8	6.8
Calcium	22.2	14.7	10.0	14.8
Density (gm/cm^3)	1.90	1.85	2.05	1.42
	Total Linear Attenuation Coefficients (cm^{-1})			
μ	0.122	0.145	0.176	0.108

A) Woodard [46]

B) NBS Handbook 85 [48]

C) Turner [49]

D) Appendix A -- 50 percent cortex, 50 percent marrow

60 keV	μ_m	= 0.191 cm^{-1}
	μ_b	= 0.389 cm^{-1}
1.0 MeV	μ_m	= 0.067 cm^{-1}
	μ_b	= 0.096 cm^{-1}

The object contrasts of bone in the presence of muscle for 14-MeV neutrons, 60-keV X-rays, and 1.0-MeV X-rays are

14-MeV neutrons	C_b = 0.006 a
60-keV X-rays	C_b = 0.099 a
1.0-MeV X-rays	C_b = 0.014 a

where a is the thickness of the bone in cm. From these considerations it appears that 14-MeV neutrons could effectively image air spaces or lung tissue that is overlaid by bone.

For a neutron source that is not monoenergetic, the object contrast is not independent of the object thickness, and the fluences in Equation 2.7 must be calculated from the integrals of $\psi(E)$ over all neutron energies. Parks et al. [30] have made these calculations for ^{252}Cf for air, bone, and fat inclusions of varying thicknesses in muscle of 10, 15, and 20 cm thicknesses. These results indicate that ^{252}Cf could also image air overlaid with bone and fat. Further calculations indicate that fast-neutron radiography of living humans could be accomplished without unreasonable exposure of the patients if an efficient detector system could be developed.

The object contrast for actual radiography systems is always less than the ideal contrast because useful information in the primary beam is obscured by scattered radiation, geometric, inherent, and motion

unsharpness, and by statistical fluctuations due to the limitation of finite fluence. The degradation of the image by scattering of radiation can be reduced with a narrow-beam, line-detection system [30], but motion unsharpness due to normal biological functions in humans becomes a limiting factor because of the time required for scanning. In order to radiograph regions such as the chest of living humans, the exposure time must be kept within a few seconds in order to minimize the unsharpness due to motion from biological functions. The additional requirement of minimum dose to the patient and the present limits on source intensity mean that the detection system must be highly efficient.

Detection Systems

Maximizing the efficiency and fidelity of the imaging process is difficult. For energies between 1.0 and 14.0 MeV the neutron cross sections of all elements are in the order of a few barns or less, so that the only way to increase detection efficiency for a given type of detector is to increase the neutron path length in the sensitive volume of the detector. This increase in thickness will invariably be accompanied by a proportional decrease in image quality due to geometric unsharpness and multiple detection of the same neutron. Detector development will therefore be an optimization process for these parameters.

Several types of imaging systems could be used for fast-neutron radiography including proton-recoil layers with photographic film, bundles of rods of a neutron scintillator with film or an optical image intensifier, an array of solid state detectors, fission-fragment track registration, and activation-transfer techniques. Scintillation methods appear to be the most promising for efficient imaging, and detector

efficiency will be a limiting factor for examinations of living humans.

Scintillation Systems. An imaging system of this type would convert a fraction of the incident energy of the neutrons into light photons that would be observed optically. An energy loss of a neutron in the detector can be recorded only through the processes of ionization and excitation caused by charged particles set in motion by the neutron. Therefore the total number of photons produced per interaction is a function of the neutron energy transferred to the charged particle. While (n,α) and (n,p) reactions also result in the production of luminescence, elastic scattering with the atomic nuclei in the detector is generally a more efficient light producing process. It is easily shown from the energetics of elastic scattering that the kinetic energy E_t transferred to the recoil nucleus by a neutron of kinetic energy E_n is

$$E_t = \frac{4 M_a M_n}{(M_a + M_n)^2} E_n \cos^2\theta \qquad (2.10)$$

where M_a and M_n are the masses of the nucleus and neutron, and θ is the angle of recoil (laboratory system). This recoil energy E_t is then converted into excitation of the scintillator molecules as the recoiling atom interacts with its neighbors. Organic scintillators are superior to inorganic scintillators for fast neutron detection because: 1) more energy can be transferred in a single elastic interaction with a light nucleus such as hydrogen, and 2) the gamma background detection efficiency of organic scintillators is less than inorganic scintillators [50]. For hydrogen, Equation 2.10 is

$$E_t = E_n \cos^2\theta \qquad (2.11)$$

In organic scintillators, essentially all of the luminescence is caused by the excitations and ionizations produced by knock-on protons from elastic interactions with hydrogen. The scintillation response is related to the energy loss of the protons in a nonlinear manner which will be discussed in Chapter IV, section Synthetic Radiographs.

In order to preserve any contrast inherent in the image, it is essential to maintain a point-to-point correspondence between incident radiation intensity at any point of the detector and the final display of this image. Therefore an imaging system that incorporates a thick organic scintillator would require some provision for channeling the light from the unit volume where it originates to the recording device which could be a photographic film or an image intensification and TV system. The method of channeling or collimation of the luminescence could be accomplished by using an array of plastic fibers or a liquid scintillator containing reflecting channels such as aluminum-foil tubing. The resolution which is possible for such an imaging device would depend on: 1) the practical problems of fabricating small-diameter collimators, and 2) the limitation imposed by the range of the knock-on protons in the scintillator. Generally, a resolution of much less than one millimeter would be difficult to obtain.

Fission Track Registration. Gamma background radiation will always be present due to (n,γ) reactions in all materials in the vicinity of the facility, from gamma emission of the neutron source, and from deexcitation of nuclei following inelastic scattering.

If efficiency can be sacrificed, an imaging system based on

fission can be constructed that is insensitive to photons and that has an inherent resolution of a few microns. When a transmitted beam of neutrons interacts with a thin film of a fissionable element, the fission-product concentration can be detected in an adjacent surface such as glass or plastic by an etching process that chemically removes the surface material at each track of a fission product. The developed image in the form of varying concentration of etched tracks can be observed directly or enhanced by coating the surface with a metal film and viewed by transmitted light. The efficiency of this type of imaging system for thick (~ 13 microns) foils of ^{232}Th, ^{235}U, ^{238}U, or ^{239}Pu has been determined to be $1.16 \pm 0.03 \times 10^{-5}$ fission track per neutron-barn [51]. This efficiency can be increased by adding layers of fissionable foils and detection plates, but in general the maximum practical efficiency will be less than acceptable for radiography of living specimens.

Photographic Emulsions. An imaging system using photographic emulsions can also be employed if efficiency is not important. The inherent unsharpness of less than 100 microns [52] is not a limiting factor, and gamma interference is not a major consideration if 14-MeV neutrons are used. Parks' results [53], which will be discussed in Chapter V, demonstrate that satisfactory radiographs can be obtained for five to 15-cm thick Plexiglas with an incident fluence of 10^9 to 10^{10} n/cm^2 using a fast X-ray film behind a proton radiator. Exposure of the emulsion is caused by the knock-on protons which are either ejected from the surface of a hydrogenous radiator or set in motion within the emulsion or its plastic base.

CHAPTER III

MODULATION TRANSFER FUNCTION AND IMAGE-FORMING QUALITY

Validity of the MTF for Analysis of Image-Forming Quality

A procedure for the analysis of radiographic systems should allow the easy assessment of the overall image-forming quality. In addition, the procedure should provide a means of determining the relative importance of the various image-degrading effects, and it should also allow the unambiguous intercomparison of separate systems. A number of methods have been tried for the evaluation of diagnostic x-radiography systems. Rossman [54] pointed out that the employment of test objects such as wire meshes, screw threads, holes in metal plates, step wedges, etc. leads only to the determination of the ability of the system to image wire meshes, screw threads, holes in metal plates, step wedges, etc. Other methods involve the use of slit mechanisms to image a series of lines and spaces of graded width to determine the resolution defined as the maximum number of lines per millimeter that can be distinguished in a radiographic image. These methods, while useful for standardization, equipment checkout, and development of techniques, have met with only limited success for the analysis of the complete system and suffer from the common fault that the apparent resolution is not independent of the apparent contrast. In addition, the resolution by itself cannot reasonably characterize the image-forming properties of the complete system. A system having good resolution characteristics can produce images having

poor definition and vice versa [55]. Similarly, in the nondestructive testing field, image quality indicators (IQI's) have been used to measure contrast and definition. These take various forms such as step wedges with and without drilled holes, and platinum wires. Feaver [56] has discussed these devices and has pointed out their limitations such as the nonuniformity of response between different types, the dependence of their response on both density and unsharpness, and the necessity of visualization of very small image areas with the attendant difficulties. While IQI's may be quite useful for comparisons of various techniques, quality control, and defect evaluation, their use for interfacility comparisons and overall systems analysis is limited.

In the fields of television, optics, and photography the technology of image evaluation and system optimization is more advanced than in the radiology field. Perrin [57] has described how resolving power has been used by photographic scientists since about 1896 for the evaluation of image-forming properties of photographic materials. It became increasingly apparent in the 1950's that the use of resolving power was fundamentally unsound, and that a method was needed that would serve as a common language for describing the behavior of individual components of a system. This need led to the evolution of the modulation transfer function (MTF) technique which is now one of the more advanced techniques for analysis of image-forming quality. It should be noted that, even if the theory had been developed earlier, this technique could not have been effectively applied because the magnitude of the calculations requires the use of high-speed digital computers.

Derivation of the MTF for Radiographic Systems

The application of modulation transfer functions in the radiographic field has been made only recently. The development and the use of these techniques in this area has been primarily due to the efforts of Morgan [58,59,60], Rossman [54,61], and Rossman and Sanderson [62].

The modulation transfer function may be defined as the Fourier integral transform of the line-spread function where the line-spread function is defined [54] as the intensity distribution in the image plane of an infinitely narrow and infinitely long slit emitting radiation of unit intensity. The MTF is a measure of the amplitude distortion existing in an imaging system. Amplitude distortion is present to some degree in all systems and is caused by scattered radiation, graininess of films and screens, and by motion and geometric unsharpness. Harmonic and phase distortion may also be present, but Morgan [60] has concluded that amplitude distortion is the most important factor influencing the image-forming quality in radiographic systems.

The MTF has two important characteristics which make it a powerful tool: 1) it is not sensitive to such factors as quantum fluctuations and viewing conditions and is therefore independent of contrast, and 2) the effects of various components of a cascaded system may be determined separately, so that these components can be optimized independently according to their relative importance. The second characteristic is derived from the useful mathematical property that the MTF of the complete system is the product of the MTF's of all the component parts provided these MTF's can be determined independently, and provided the components are essentially linear. Calculated MTF's identify in a quantitative

manner the problem areas in systems design. They may also be used as a guide for accepting or rejecting particular radiography systems on the basis of theoretical considerations before any pilot experiments are undertaken.

Instead of thinking of the MTF as a Fourier integral transform of the line-spread function, it is more useful to define the MTF as the percent amplitude response in an image as a function of the spatial frequency of sinusoidal grooves in an object. Intuitively, one might expect that, if the peak-to-valley dimension in the object can be detected in the image, it could be seen most easily when the spatial frequency is low, i.e. the distance between peaks or valleys is great. As the spatial frequency is increased one also might expect that at a sufficiently high frequency the sinusoidal structure of the object could not be seen in the image. This intuitive approach can also be applied to the resolution of lines and spaces of equal width. The distortion that affects the image quality, and that reduces to a uniform blur the image of high-frequency grooves in an object, is a continuous function expressed quantitatively by the MTF as the amplitude response versus spatial frequency. This plot can then be used to indicate the amplitude distortion at all frequencies including the frequency corresponding to the resolution (where the amplitude response is reduced to approximately five percent). The MTF can be measured by imaging several test objects having sinusoidal grooves of different spatial frequencies (Figure 4), and then determining the detector response at the peaks and valleys. This approach has been used [60], but the experimental difficulties are obvious. A better approach is to determine the line-spread function

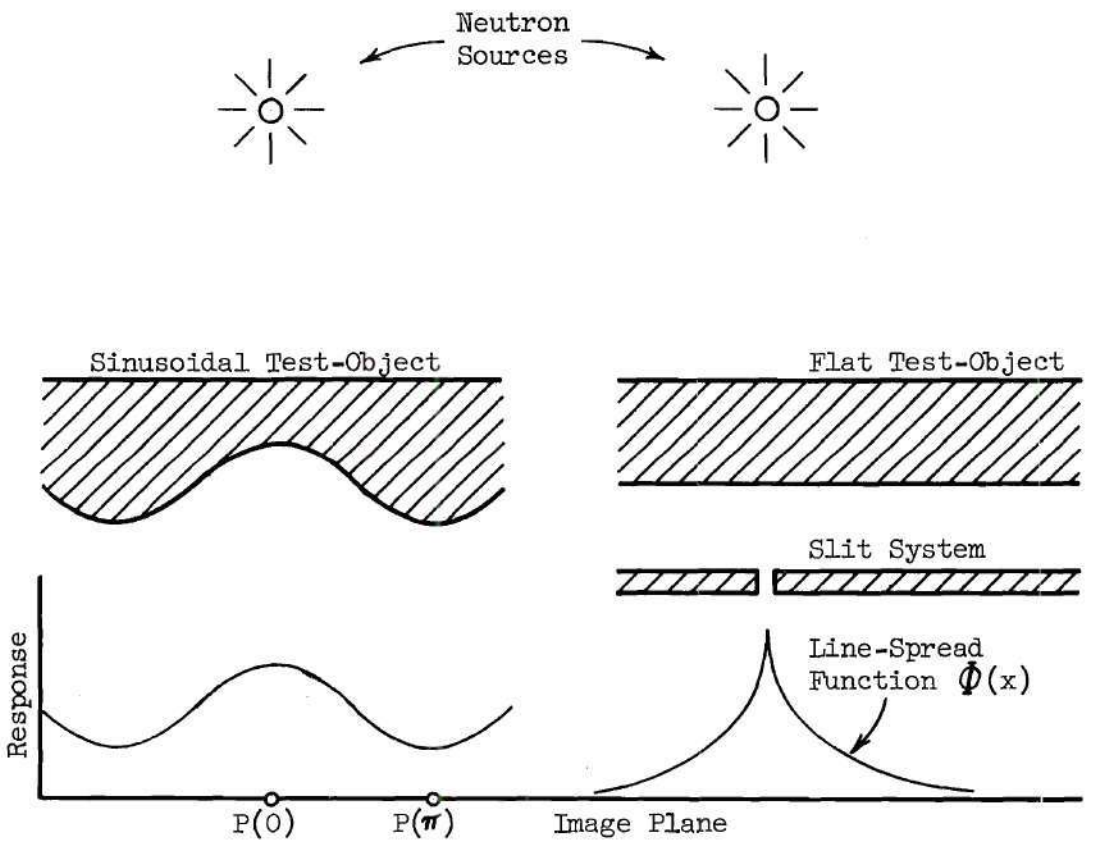

Figure 4. Geometries for Determining Amplitude Response and Line-Spread Functions

and to calculate the MTF for a series of frequencies using the normalized convolution integral

$$A_o = \frac{\int_{-\infty}^{\infty} \Phi(x) \cos 2\pi f x \, dx}{\int_{-\infty}^{\infty} \Phi(x) \, dx} \tag{3.1}$$

where f is the spatial frequency.

Equation 3.1 may be derived from physical considerations as follows. Consider a sinusoidal test object (Figure 4) interposed between a radiation source and an image plane. For exponentially-attenuated radiation, the primary fluence transmitted through the object will vary with the path length y according to

$$F_p = F_o \exp(-\mu y) \tag{3.2}$$

where μ is the total attenuation coefficient. If the peak-to-peak thickness is small (low contrast conditions), Equation 3.2 may be approximated by

$$F_p \simeq F_o(1 - \mu w) \exp(-\mu v) \tag{3.3}$$

where v is the minimum object thickness, w is the peak-to-peak amplitude, and $y_{max} = v + w$; or

$$F_p = F'(1 - \tfrac{1}{2}\mu w(1 + \cos 2\pi f x)) \tag{3.4}$$

where $F' = F_o \exp(-\mu v)$. For a small overall thickness variation we may

also assume that the scattered fluence F_s is proportional to the mean thickness. An image of the test object will reproduce the sinusoidal shape with an accuracy dependent on the amount of amplitude distortion present at the spatial frequency f. The value of the MTF at the spatial frequency f is the difference in image response at points P(0) and P(π) normalized to the condition of no amplitude distortion by dividing by the limit of the response difference for P(0) and P(π) as the spatial frequency approaches zero. Alternately, the same image would result if a series of exposures were taken with a slit system interposed between the object and image plane with the slit position incremented by one slit width Δx in the x direction per exposure. A single exposure produces a line-spread function, $\Phi(x,\Delta x)$, which contributes to the image formation at every point an amount proportional to the fluence at the slit position and to the slit width. The dependence of the response on the slit width may be removed by progressively decreasing Δx until $\Phi(x)$ shows no further change. An integration of the incremental contributions of each exposure at a particular point equals the total response for the condition of a single exposure with no slit. The response at point P is equal to

$$E_p = a_o F' \int_{-\infty}^{\infty} \Phi(x) \left[\left(1 - \tfrac{1}{2} \mu w \left(1 + \cos 2\pi f (x + x_o) \right) \right) \right] dx \qquad (3.5)$$

where a_o is a proportionality constant, and x_o is the distance from point P to the closest point of minimum thickness in the x direction. Obviously, the response will be greatest at points P(0), i.e., where $x_o = 0$, immediately under the thinnest portions of the object, and the

response will be least at P(π), i.e. where $x_o = f/2$ under the thickest portions. The amplitude response A is the difference between $E_{P(0)}$ and $E_{P(\pi)}$,

$$A = a_o F' \left[\int_{-\infty}^{\infty} \Phi(x) \left(1 - \tfrac{1}{2}\mu w(1 + \cos 2\pi f x)\right) dx - \int_{-\infty}^{\infty} \Phi(x) \left(1 - \tfrac{1}{2}\mu w\left(1 + \cos(2\pi f x + \pi)\right)\right) dx \right] \tag{3.6}$$

But since $\cos(2\pi f x + \pi) = -\cos 2\pi f x$, Equation 3.6 reduces to

$$A = -a_o \mu w F' \int_{-\infty}^{\infty} \Phi(x) \cos 2\pi f x \, dx \tag{3.7}$$

Equation 3.7 reduces to Equation 3.1 upon normalizing to A at f = 0 because

$$A_{f=0} = -a_o \mu w F' \int_{-\infty}^{\infty} \Phi(x) \, dx \tag{3.8}$$

The qualitative significance of amplitude distortion is that sharp boundaries in the object are imaged with a blurring that is proportional to the amplitude distortion of all spatial frequencies. If the MTF's of the response of different systems show the same resolution characteristics, superior image quality will be produced by the system having less distortion of the lower frequencies. Calculations of the MTF should define the amplitude distortion over the range of spatial frequencies from about 0.01 cycle/mm, where all useful systems exhibit essentially no distortion, to a sufficiently high spatial frequency that the amplitude distortion is decreased to the order of a few percent.

CHAPTER IV

PROCEDURES

Mathematical Treatment of Neutron Transport

The formal mathematical description of the interaction of neutrons with matter is identical with the description of the interaction of gamma radiation with matter; however, in detail the two are only vaguely similar.

A mathematical description of the steady-state, i.e. time-independent, condition of a system containing a neutron source is an expression of the spatial, directional, and energy distribution of neutrons in the system. This involves the neutron distribution in a differential element $d\tau = dV\, d\Omega\, dE$ in six-dimensional phase space requiring three variables to define position, two to define direction, and one to define energy. Therefore a neutron in $d\tau$ is located in the volume element dV in three-dimensional coordinate space, and is traveling in the direction $\hat{\Omega}$ within $d\Omega$ with energy between E and $E + dE$. The total number of such neutrons is given by $N(\overline{r},E,\hat{\Omega})dE\, d\Omega$. It is this angular number flux density function which must be defined in order to analyze time-independent conditions in reactors, shielding, and radiography. Formally, $N(\overline{r},E,\hat{\Omega})$ is defined in a conservation equation for neutrons in a steady-state system by the Boltzmann transport equation which can be abbreviated as

$$L + (A + S_o) = S_i + s \qquad (4.1)$$

where

L = total leakage of neutrons out of $N(\bar{r},E,\hat{\Omega})$

$A + S_o$ = removal of neutrons out of N by absorption and scattering

S_i = scatter into the range of $N(\bar{r},E,\hat{\Omega})$

s = source term for the generation of neutrons into the range of $N(\bar{r},E,\hat{\Omega})$

Unfortunately a rigorous analytic solution of the Boltzmann transport equation is unavailable for practical applications. Most approximate solutions have been developed in the fields of reactor theory and shielding using the techniques of either: 1) numerical approximations and iterative calculations, or 2) the elimination of one or more of the six variables. Most of these techniques are derived from one or more of the following penetration or transport methods [63,64, 65,66,67]: 1) kernel theory, 2) removal-diffusion theory, 3) moments method, 4) spherical harmonics method, 5) discrete ordinates method, 6) Fermi-age theory, and 7) Monte Carlo method.

The Monte Carlo method is the only currently available technique that can be successfully applied to the problem of the theoretical examination of the image-forming quality of fast-neutron radiographic systems.

The Monte Carlo method is a stochastic method of obtaining estimates of the behavior of a system by computing the average of a large number of individual events. The concept is simple, but a great deal of skill and ingenuity is necessary for the successful application of the method. Credit is generally given to von Neumann and Ulam at

Los Alamos in the 1940's as the instigators of the method for physics and engineering problems.

Despite the early interest in the Monte Carlo method, the development was slow and is only now becoming widely employed. This is due to two factors: 1) the success of the method depends on effective techniques for variance reduction, and 2) the economical solution of any but trivial problems by Monte Carlo techniques requires the use of a high-speed digital computer.

For the solution of neutron transport problems, the straightforward approach of simulating the physical process step-by-step is usually employed. The behavior of neutrons in a system is obtained from the analysis of the histories of a large number of individual neutrons from birth until termination. The parameters characterizing the neutron at any time during its life are determined statistically using a detailed cross-section package to define the various probabilities of interactions, energy loss, scattering angle, etc. Obviously, the accuracy of the method depends on the validity and completeness of the cross section data and the total number of the neutrons available for analysis in a given region.

The use of the Monte Carlo method generally necessitates the employment of variance reducing techniques in order to obtain accurate estimates of the desired parameters without excessive use of computer time. Some of the more common methods for variance reduction are: 1) importance sampling, 2) the use of expected values, 3) Russian roulette and splitting, 4) correlation and regression, and 5) systematic sampling. These techniques have been developed and discussed by Kahn [68,69,70].

Monte Carlo Methods Used in Analyses

The basic computer code used in this research was written at the Oak Ridge National Laboratory [71]. This code, named O5R, provides a statistical solution of the Boltzmann transport equation. The code was revised and expanded by the author for better adaptation to this study. Several significant features are incorporated in O5R which make it the most useful neutron transport code currently available.

O5R allows as many as 36 parameters to be recorded per collision at the option of the user. For most of the analyses in this study, 10 parameters were required. The most useful of these included: type of collision (real interaction with a nucleus, crossing a medium boundary, or escape from the system), coordinates of the interaction, speed squared before and after collision, statistical weight before and after collision, element identification, and region identification. An additional parameter was inserted into the code so that the energy of the recoil nucleus could be recorded after inelastic interactions.

Cross Section Manipulations

Macroscopic cross sections for most elements show a very pronounced resonance structure (see Appendix A). This is particularly true, with the exception of hydrogen, for the light elements which occur in biological tissue. In order to adequately represent these fluctuations, a tremendous amount of data must be sorted and referenced during a Monte Carlo analysis. Obviously, a large number of data points are required to define the cross section values over the energy range from a few eV to 14 MeV. O5R accomplishes its task by processing neutrons in batches of 1000 within fixed energy groups with each neutron being

degraded in energy over the fixed range of energy until none have an energy higher than the lower limit. In this way only the data for a single energy group are needed in the computer core. These data are successively replaced by data for lower energy groups until the batch is completely analyzed. The detail with which the cross sections are described is under the user's control. The range of 77.13 MeV to 0.0701×10^{-3} eV is divided into 40 energy groups by energy boundaries that are a factor of two apart. These supergroups are subdivided into equal energy intervals from two to 1024. Two intervals may be adequate for a gross analysis, but generally 64 to 256 are required for adequate accuracy for most problems. Increased accuracy is always obtained at the expense of longer computation times. Results which are reported in this paper were obtained with 128 points per supergroup. The author found it necessary to double the capability of the code in order to include in the calculations all of the chemical elements that are important in biological media.

Variance Reduction

Any nontrivial Monte Carlo code must have provision for variance reduction. This fact follows from the statistical nature of the method. (The results are derived in the form of averages.) The accuracy of these averages is a function of the number of samples from which the averages are formed. However, the calculation of a single neutron history involves a significant amount of computer time. With all the ingenious variance-reducing devices being employed, many problems for which a Monte Carlo solution is being sought are so complex that only several thousand neutrons can be analyzed in the budgeted amount of

computer time. This often results in estimates having large variances, and herein lies the major disadvantage of Monte Carlo techniques.

The most obvious variance-reducing device that is employed by O5R is the use of a weighting system. This is a type of importance sampling in which each neutron is assigned an arbitrary weight at birth (usually 1.0). At every interaction of the neutron with a nucleus the weight is adjusted downward by the ratio of the macroscopic scattering cross section to the macroscopic total cross section for the medium at that energy. In this manner no neutron is ever absorbed, but absorption is taken into account by reducing the importance of the neutron at each collision by the absorption probability.

Another common method of variance reduction is "Russian roulette," which may be employed at the user's option. Russian roulette is a means of limiting the computer time spent following neutrons that have little statistical importance. If the neutron weight falls below a preset value, that neutron is subjected to a game of chance to determine if the neutron history will be terminated or if the history will be continued with an increased weight. No bias is introduced because on the average, the sum of the weights of neutrons that have been killed is balanced by an equal weight-sum which is distributed among fewer neutrons.

Other more specialized variance reduction techniques such as splitting and angular biasing, which are available in O5R, were not required for this research.

Scattering Angles

Selection of scattering angles is accomplished in one of three ways:

1) Isotropic distribution

2) A distribution having a specified value of the first Legendre coefficient (the P_1 approximation)

3) An anisotropic distribution which is specified by more than one Legendre coefficient.

These options all refer to the center-of-mass system. During the preliminary phases of this study it was ascertained that, for the media and geometries examined in the current research, there was no significant difference in the results of histories generated using the P_1 approximation, i.e. linearly anisotropic, and the results of histories generated using the P_8 approximation, i.e. a nonlinearly anisotropic distribution specified by a nine-term Legendre polynomial. The P_1 approximation is preferred for reasons of computational speed and ease of problem setup. For hydrogen at all energies below 14 MeV and for the other elements at energies below a few hundred keV, elastic scattering is essentially isotropic. The Legendre coefficients used in this study were taken from the O5R cross section library. Because no coefficients were available for phosphorus, isotropic scattering was assumed at all energies.

Inelastic Scattering

The capability to handle inelastic scattering was developed and built into the O5R code by the author. Appendix B gives the kinematics of inelastic scattering. The computer code treats inelastic scattering in two ways. If probability data for discrete-level excitation are available for the energy of a neutron, then nuclear excitation is selected from one of the possible discrete levels. If level data are not

available, or if the neutron energy is sufficiently high, then the inelastic interaction is treated as continuous-level excitation. In this case a statistical model is assumed [72] where the compound nucleus is treated as a Fermi gas of nucleons. According to this model, the energy spectrum of scattered neutrons is a continuous Maxwellian distribution [67] given by

$$N(E)\ dE = \frac{E/\theta\ \exp(-E/\theta)}{G} \qquad (4.2)$$

where

E = energy of inelastically scattered neutron in the center-of-mass system

$\theta = kT = 3.23\ E_o/A$

E_o = energy of incident neutron in the center-of-mass system

A = target mass number

G = factor for normalization to unit area

$$= \int_o^{E_{max}} E/\theta\ \exp(-E/\theta)$$

where $E_{max} = E_o - Q_1$, and Q_1 = the lowest binding energy of the nucleus

In this expression the temperature T is derived from Weisskopf's level-density formula [73]. Equation 4.2 is strictly valid only where the cross section for elastic resonance scattering is small and at energies where many levels of the target nucleus are excited. The angular distribution of the scattered neutrons is isotropic if the compound nucleus is sufficiently excited so that the statistical theory is also valid for

the residual nucleus [74].

For light nuclei the angular distribution is generally anisotropic, and the discrete nature of the energy distribution of the scattered neutrons can be observed [75]. However, to a fair approximation and in the absence of a better alternative, inelastic scattering may be assumed to be isotropic in the center-of-mass system. Appendix C explains the method of selection of the appropriate direction cosines in the laboratory system.

System Geometry

Incorporated into O5R is the provision for handling complex geometries. Almost any system geometry that can be described by a series of intersecting quadric surfaces can be treated by the code. The main limitations involve the size of the computer core, the ingenuity of the user, and the increase in computation time as the complexity of the description increases. The reader is referred to the documentation [71] for the description of the capability of the system.

Dosimetry

For elastic interactions the contribution to the dose is the energy loss of the neutron divided by the mass of the unit volume of the target. The energy loss in MeV is the difference in the neutron speed squared in cm^2/sec^2 divided by the constant 1.9132×10^{18} cm^2/sec^2-MeV. The locally-absorbed dose for an inelastic interaction cannot be obtained directly from the neutron energy loss because a fraction of the excitation energy usually escapes the nucleus in the form of gamma rays from a deexcitation cascade. The energy of these gamma rays cannot be accumulated as locally-absorbed dose. The recoil energy of the nucleus

(see Appendix B) is returned to the output data file as one of the parameters that characterizes the collision.

Neglecting the contribution to the dose by gamma rays from capture and those produced by inelastic interactions, as well as the contributions from (n,2n), (n,α), and similar reactions, results in underestimating the dose by several percent at incident neutron energies up to 14 MeV (see Chapter V, section Dosimetry Calculations). Such an error in the dose calculations is not considered to be significant for this study.

Analysis of Neutron-History Data

Of particular significance is the fact that no analysis is performed by the O5R code itself. This increases the versatility of the code because every problem is unique and often requires special treatment. Consequently, the user must develop all the procedures for the analysis of the neutron-history data. For this study, the neutron-history data were recorded on a large, temporary file on the Univac-1108 FASTRAND drum. The mainline program of O5R was rewritten to call specialized analysis subprograms after completion of the neutron history data file. In this manner a first-order data reduction was performed immediately on the raw data. This eliminated the handling and storage of magnetic data tapes. Second- and third-order data reductions were required for most of the problems, and these operated on the printed output, punched cards, and punched paper tape that were produced by the initial analysis.

Line-Spread Distributions

Four factors that affect the image-forming quality of fast-neutron radiography systems are examined in this research. These are geometric unsharpness, scatter in standard man tissue, intensity spread in thick organic scintillators, and spread in other types of detectors. The effect on the image-forming quality from these factors is examined by calculation of the line-spread functions (LSF) and the corresponding modulation transfer functions (MTF).

As explained in Chapter III, modulation transfer functions are more easily obtained from the appropriate transformation of some other distribution. In experimental measurements the line-spread function is usually determined and the MTF is then calculated from the LSF. The MTF may just as well be derived from a point-spread function (PSF) if the system under study is symmetric. The LSF $\Phi(x)$, defined as the intensity distribution in the x direction of an infinitely long and infinitely thin slit perpendicular to x emitting radiation of unit intensity, is related to the PSF $\psi(r)$, defined as the intensity distribution along the radial direction r of an infinitely small point emitting radiation of unit intensity, by the expressions

$$\Phi(x) = 2\int_{x}^{\infty} \frac{\psi(r)\, r\, dr}{\sqrt{r^2 - x^2}} \tag{4.3}$$

and

$$\psi(r) = \frac{-1}{\pi} \frac{d}{dr} \int_{r}^{\infty} \frac{\Phi(x)\, r\, dr}{x\sqrt{x^2 - r^2}} \tag{4.4}$$

The experimental difficulties of approximating an ideal PSF are obvious, so that this approach is of only academic interest. However, for the theoretical approach, the PSF is just as easily calculated as is the LSF and in fact is preferable from considerations of computer efficiency. For the calculations all of the primary fast-neutron radiation is directed along the same line, or for a finite source all of the primary radiation is directed through the same point between the source and the detector plane.

Geometric Unsharpness

Reasonable estimates of the effect of geometric unsharpness may be obtained analytically if the assumption is made that the source can be approximated by a disc with its axis in the beam direction and having uniform emission rate. The transmission of radiation from this disc source through a point in the object to the detector plane results in a disc-shaped image whose diameter is the value of the geometric unsharpness. The line-spread function then is obtained by integration. Because the PSF $\psi(r)$ is a constant over the image, Equation 4.3 becomes

$$\Phi(x) = 2\psi\int_{x}^{\infty}\frac{r\,dr}{\sqrt{r^2 - x^2}} = 2\psi\sqrt{R^2 - x^2} \qquad (4.5)$$

which ranges from $2\psi R$ at $x = 0$ to 0 at $x = R$. Obviously, the geometric unsharpness depends on the relative locations of the source, object point, and the detector plane. However, the exact arrangement need not be known if calculations are made for a range of values of U_F because an infinite number of geometric arrangements can result in the same value of U_F.

Spread Induced by Scatter in Standard Man Tissue [76]

The purpose of this series of calculations is to examine the effect of scattered neutrons on the image-forming quality. The procedure involves Monte Carlo analyses of the passage of a point beam of neutrons (all source neutrons enter the tissue along the same line) through tissue of various thicknesses. The line-spread functions for neutrons penetrating tissue must be related to some form of detection system in order to have interpretable meaning. As explained in Chapter II, the most promising imaging systems respond approximately as: 1) the number fluence, and 2) the energy fluence. Accordingly, line-spread functions are calculated for both types of imaging devices. For the effect of scatter in the object on the image-forming quality, a perfect imaging device is assumed. Scatter within the imaging devices themselves is examined separately.

Spread in Organic Scintillators

The composition of a typical liquid scintillator for fast-neutron applications is given in Table 3 [77]. The Monte Carlo calculations for organic scintillators are based on these figures.

In order to examine theoretically the effect of organic scintillators on the image-forming quality of fast-neutron radiography systems, it is necessary to know the response in terms of light output as a function of incident neutron energy. The scintillation response L of organic scintillators is known to be nonlinear. Birks and Black [78] proposed a semi-empirical relation which predicts the specific fluorescence dL/dr as a function of specific energy loss or stopping power dE/dr

Table 3. Composition of a Typical Liquid Organic Scintillator

Chemical Compound	Formula	Wt. Fraction
Napthalene	$C_{10}H_8$	0.055
PPO (2.5, diphenyl-oxazole)	$C_{15}H_{11}NO$	0.01
POPOP (1,4-bis-(2-(5-phenyloxazolyl))-benzene)	$C_{24}H_{16}N_2O_2$	0.0001
Xylene	C_8H_{10}	0.9349

Element	Atomic Composition Atoms/cm^3 ($\times 10^{24}$)	Wt. Fraction
Hydrogen	0.048835	0.093
Carbon	0.040038	0.906
Nitrogen	0.000024	0.00063
Oxygen	0.000024	0.00073

$$\frac{dL}{dr} = \frac{S\ dE/dr}{1 + kB\ dE/dr} \tag{4.6}$$

where L is the scintillation response, r is the range of the charged particle in the scintillator, S is the absolute scintillation efficiency, B is a constant, and k is a quenching parameter. B dE/dr is the specific density of ionized and excited molecules along the particle track. Birks [50] describes experimental and theoretical considerations involved in this relation. What is needed for this research is the solution of Equation 4.6 for a proton of energy E that is created by an elastic interaction of a neutron with hydrogen in the scintillator. Prescott and Rupaal [79] evaluated the constant kB as 0.0091 g/cm^2 from electron-proton data using an NE-102 scintillator.* Gooding and Pugh [80] evaluated the response of NE-102 to protons and developed the range-energy relation of

$$dE/r = 17.91\ r^{-0.448} \tag{4.7}$$

where E is in MeV and r is in g/cm^2. Using these values changes Equation 4.6 to

$$\frac{dL}{dr} = \frac{17.91\ S\ r^{-0.448}}{1 + 0.163\ r^{-0.448}} \tag{4.8}$$

The solution of Equation 4.8 is not available in analytical form, but Figure 5 shows the evaluation of dL/dr as a function of energy along with the empirical curve that was fitted to these points

*Product of Nuclear Enterprises, Ltd., Winnipeg, Canada.

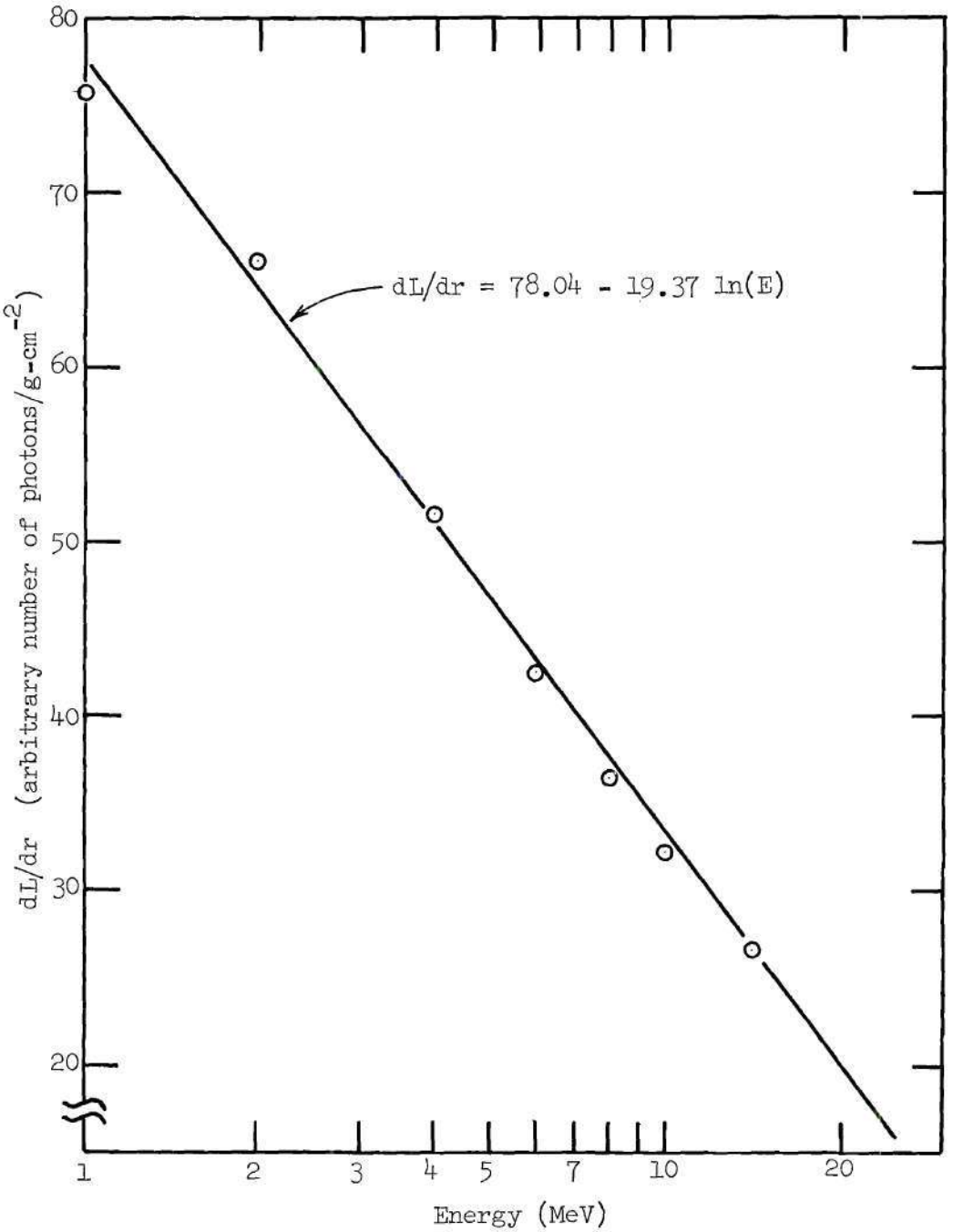

Figure 5. Specific Fluorescence in NE-102 as a Function of Proton Energy

$$\frac{dL}{dr} = 78.04 - 19.37 \ln E \tag{4.9}$$

Substitution of

$$r = 0.001829\ E^{1.816} \tag{4.10}$$

from Equation 4.7 into Equation 4.9 and integration from 0.5 MeV (the lower energy bound for light-producing protons) to E_o results in an empirical relation for the total scintillation response L (number of photons) produced by a proton whose initial energy is E_o

$$L = E_o^a\ (b - c \ln E_o) - d \tag{4.11}$$

where a = 1.8116, b = 0.16232, c = 0.035434, and d = 0.053238. Figure 6 shows a plot of L in arbitrary units as a function of proton energy. The severe nonlinearity over the range from 0.5 to 14 MeV is apparent.

For all the calculations of spread in organic scintillation detectors, the fundamental assumption was made that the inherent unsharpness for these detectors is 0.5 mm. Inherent unsharpness is the contribution of the imaging device to the total unsharpness. For organic scintillation systems this unsharpness is due to the cross sectional area of the fibers or light-collimating channels.

Spread in Other Detectors

The reduction in image-forming quality for other types of imaging systems can also be predicted by the calculation of the appropriate line-spread functions. Imaging systems based on fission track

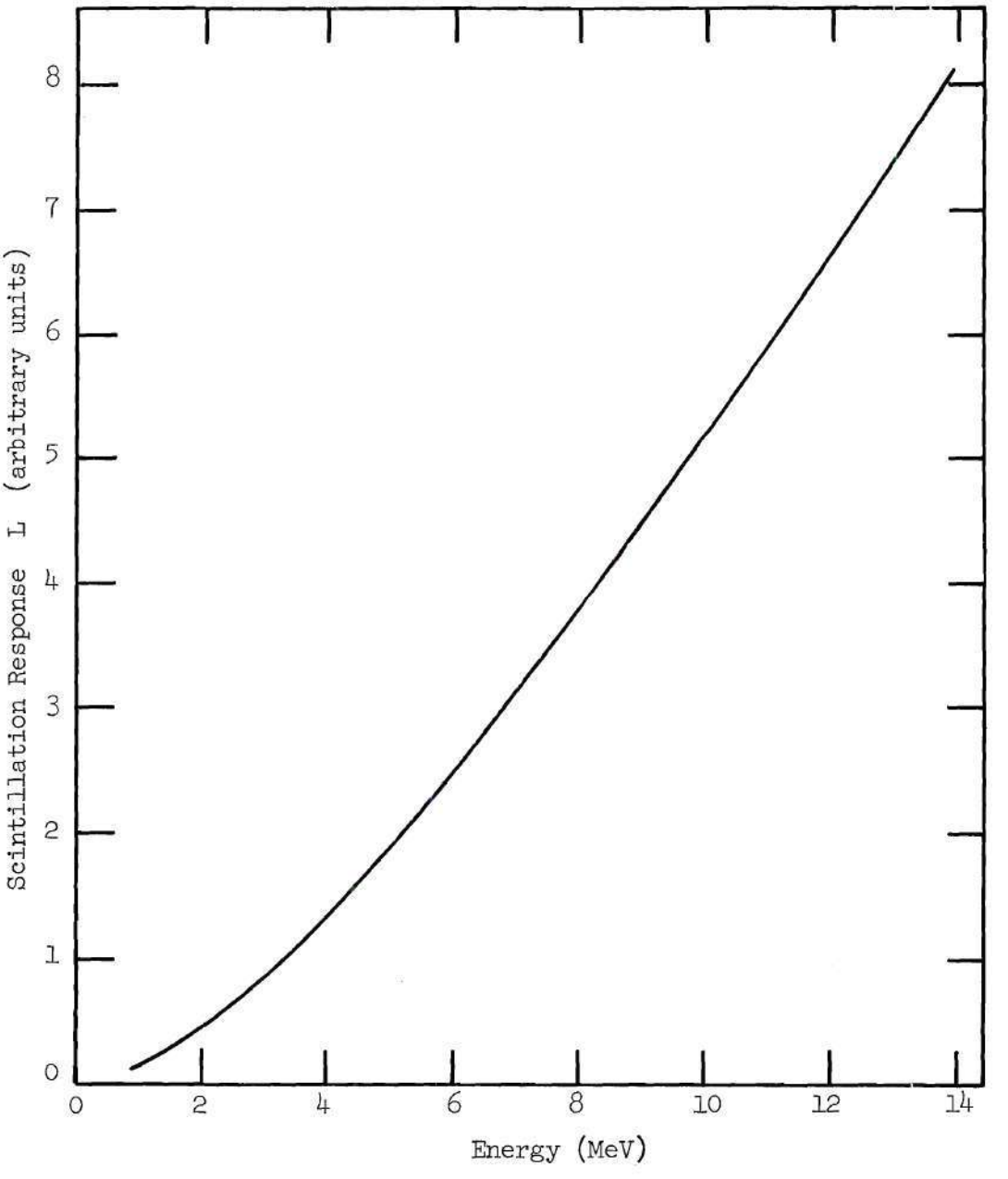

Figure 6. Scintillation Response as a Function of Proton Energy

registration or on the exposure of photographic film to the luminescence produced in a scintillation convertor screen and/or to knock-on protons cause a spread in the image that is small compared with the effects of other image-degrading factors such as scatter in the object and geometric unsharpness. The response of the detection plate to one event can be approximated by a symmetrical point-spread function. The shape of this PSF could be a step function caused by a clump of metallic silver in the photographic film, or the same type of PSF could result from the expansion of an area of damage in a detector plate caused by a fission track. On the other hand, the shape of the PSF could be more complicated in the case of exposure to the light produced in a thin convertor screen. The exact shape will depend on the specific imaging system and on the specific experimental techniques such as developing time. No calculations of these effects have been included in this study because: 1) the spread will be small, and 2) no generally applicable assumptions can be made concerning the shape of the spread functions.

Modulation Transfer Functions

As explained in Chapter III, the MTF is the variation of amplitude response as a function of spatial frequency. It is obtained by evaluating Equation 3.1, the normalized Fourier integral transform of the line-spread function $\Phi(x)$

$$A_0 = \frac{\int_{-\infty}^{\infty} \Phi(x) \cos 2\pi f x \, dx}{\int_{-\infty}^{\infty} \Phi(x) \, dx}$$

(The line-spread functions are obtained from the Monte Carlo analyses of the neutron transport and interaction in the radiographic systems.) Equation 3.1 must be evaluated numerically. In order to do this a computer code was developed in which the interpolation and numerical quadrature are based on third-degree, natural spline functions. Greville [81] has discussed the theory and uses of spline functions, and pointed out that these functions: 1) are relatively easy to calculate, 2) give satisfactory results, and 3) provide the "smoothest" interpolating function between N discrete points on the abscissa at which the value of a function $\Phi(x)$ is known. "Smooth" is used in the sense that each set of adjacent polynomial arcs to the left and right of each x_i have the same values for the ordinate $\Phi(x_i)$ and the first two derivatives of $\Phi(x)$. The code that was developed requires 43,680 words of computer core, but it has the advantages of speed and accuracy. It was found that 12 points per cycle adequately describe the value of the cosine function. However, at low spatial frequencies the number of points that must be evaluated to adequately define the function $\Phi(x)$ cos $2\pi fx$ over a cycle was determined by the line-spread function $\Phi(x)$. For low frequencies the function $\Phi(x)$ cos $2\pi fx$ was evaluated at points x which were separated by the minimum distance between points that defined $\Phi(x)$. The amplitude response A_o was evaluated at a sufficient number of frequencies f to define the MTF over the range of 0.01 to 100 cycles per mm.

Synthetic and Experimental Radiographs

Because any given dynamic experiment can be simulated mathematically provided the physical theory is adequate, it is useful to have a

comparison of the current theoretical methods with an actual experiment. Such a comparison was undertaken with the experimental phase being conducted by P. B. Parks at the Savannah River Laboratory (Aiken, South Carolina).

Two polymethyl methacrylate (Plexiglas) blocks, five and 15 cm thick with 1.905 cm holes in both, were radiographed. Figure 7 shows the geometrical arrangement for the radiographs. The separation of the cassette and the plastic block was varied in order to determine the feasibility of improving the image quality by reducing the interference from scattered neutrons. The image of the cylindrical hole was detected and recorded by the photographic emulsion through: 1) the sensitization produced by recoil protons ejected from a hydrogenous radiator, and 2) from the luminescence of a calcium tungstate screen adjacent to the film.

Experimental Radiographs

A detailed description of the research of Parks [53] on direct 14-MeV radiography using photographic film for the imaging will be published as a technical report of the Savannah River Laboratory. A neutron generator was used to produce 14-MeV neutrons by the D-T reaction. The accelerator was operated at a voltage of 150 kV and at deuteron beam currents of between 550 and 600 microamps which gave a maximum yield (with a new tritium-loaded titanium-copper target) of between 5.5 and 6.0×10^{10} n/sec. Exposures were made in a large, concrete-walled room with no collimation and a minimum amount of scattering material near the target. A Radelin T cassette was used with Kodak Type NS-54T X-ray film with a one eighth inch Plexiglas proton radiator on the beam side and a

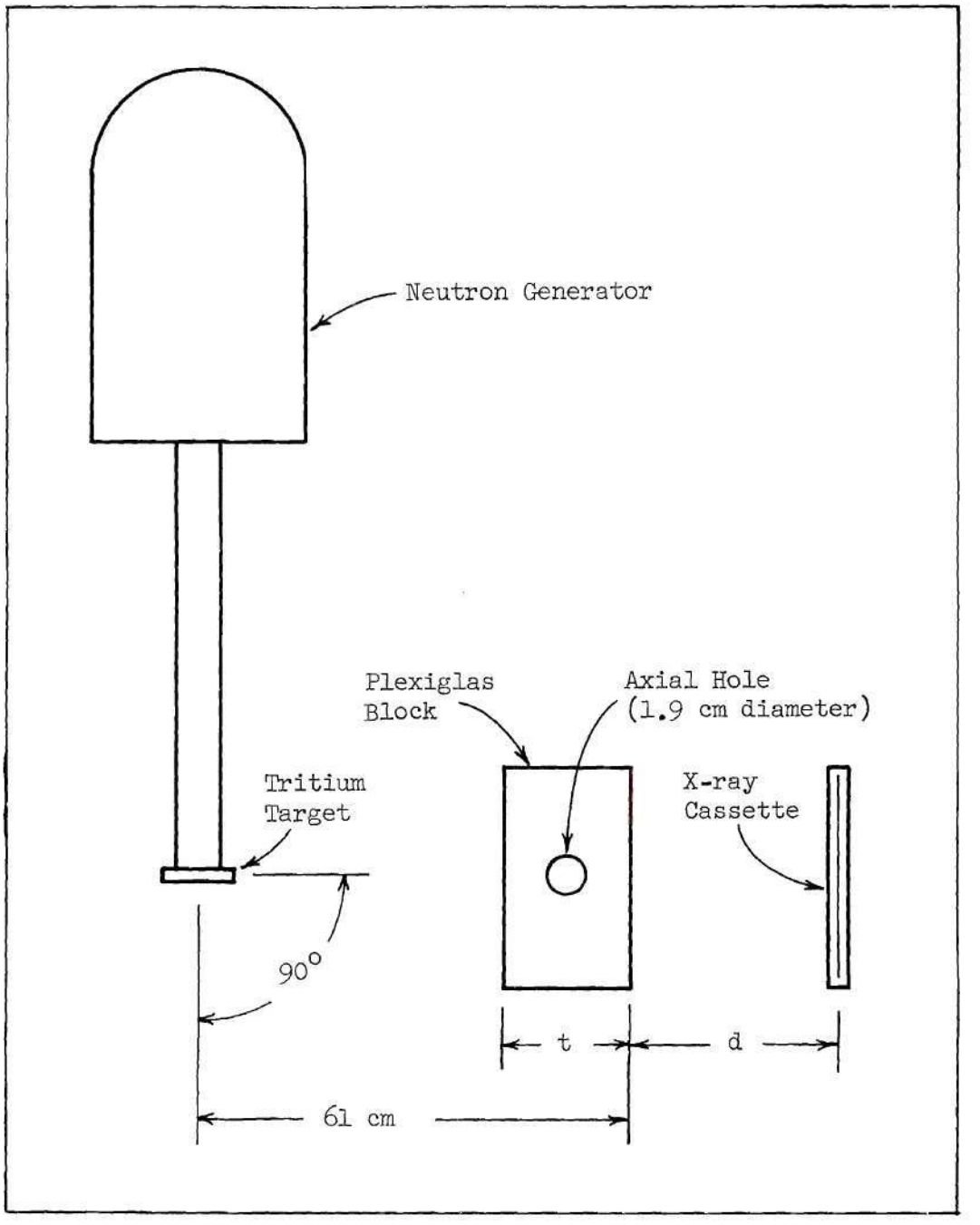

Figure 7. Experimental Arrangement for Neutron Radiographs

$CaWO_4$ convertor screen on the back side. The separations of the Plexiglas block and the cassette were: 1) zero for the condition of maximum interference from scattered neutrons, and 2) 50 cm for a reduction in the interference. The difference in the geometric unsharpness for the two geometries was insignificant.

Successful radiographs were obtained with exposure times in the range of 2000 to 3000 seconds depending on the age of the tritium target and the thickness of the plastic. Standard chemicals and procedures were used for development of the X-ray film.

Synthetic Radiographs

Pseudophotographic images were obtained by recording a computer-controlled oscilloscope display on X-ray film. The formation of the visible image as a photographic negative was the result of a three-step process: 1) the calculation of the image pattern that is formed in the neutron beam emerging from the Plexiglas block, 2) the calculation of the transfer function that relates the neutron image to an absorbed dose image in the emulsion, and finally 3) the conversion of the energy pattern in the emulsion to variations in optical density in the developed negative through the use of the film-response function.

Step (1) was accomplished by the straightforward application of the Monte Carlo method to obtain the specific energy fluence of the neutron penetration of the Plexiglas. In the absence of data for the atomic composition of Plexiglas, data for Perspex, a similar polymethyl methacrylate plastic, were substituted. Table 4 gives the atoms per cm^3 and weight fractions of Perspex [25].

Table 4. Atomic Composition of Perspex

Element	Atoms/cm^3	Wt. Fraction
Hydrogen	0.058×10^{24}	0.0728
Carbon	0.014×10^{24}	0.2094
Oxygen	0.036×10^{24}	0.7175

A point source of 14-MeV neutrons was assumed for the calculation. This is a valid assumption because the images of object inclusions which are symmetric in one dimension are essentially the same for a point source as for a finite but small line source provided the line is parallel with the inclusion symmetry (see Figure 7).

The energy deposition in the emulsion was assumed to be due entirely to the loss of energy by knock-on protons. Elastic interactions of 14-MeV neutrons with hydrogen are twice as probable as the sum of elastic interactions with carbon and oxygen in Plexiglas. In addition, the ranges of the average carbon and oxygen nuclei are less than 5×10^{-3} mm compared to a range of about 0.6 mm for an average knock-on proton [82].

The Monte Carlo solution for the neutron transport from the source, through the Plexiglas phantom to the detector plane, was recorded as a large number of collisions with the detector plane of neutrons each characterized by its weight, energy, and position. The analysis process was designed to convert these neutron data into the line-spread function of the energy-deposition density in the emulsion. Each neutron

was assumed to interact with the thin (2.2 mm) Plexiglas proton-radiator with a probability proportional to the elastic scattering cross section of hydrogen. The depth of interaction, angle of proton recoil, and proton energy were calculated, and if the proton escaped the Plexiglas radiator, the energy deposited in the emulsion at that point was recorded. Because of the symmetry of the axial hole in the Plexiglas block, the energy density in the emulsion could be reduced to a line-spread energy-density function in the direction perpendicular to the axial hole.

Step (3) of the imaging process was accomplished by exposing Kodak Type NS-54T X-ray film to the image produced on a computer-controlled Tektronix Model 515-A oscilloscope. The oscilloscope display was controlled by a Digital Equipment Corporation Model PDP-8/I digital computer through a code that accepted as input the line-spread energy-density function that was the result of the Univac-1108 Monte Carlo analysis. A spot-reading cadmium-sulfide photometer was used to adjust the intensity of the oscilloscope display prior to exposure of the film.

Standard techniques were used for developing the NS-54T film. Next, a one-cm strip of the developed film was removed for densitometer analysis. A Canalco Model F scanning microdensitometer was used to obtain an optical density trace of the image. An estimate of the object contrast could then be obtained by converting the density values to relative exposures from the characteristic curve. The characteristic curve was obtained by successively exposing one-cm bands of film to five oscilloscope traces for each of 1000 increments of vertical deflection.

The result was a step image consisting of relative exposures of 0, 5, 10, 15, 20, and 30 traces per vertical increment.

Scattering Calculations

Scattered radiation that is detected in the image plane causes a reduction in contrast and an increase in unsharpness. Radiographs whose image quality is seriously affected by radiation scattered by the object can sometimes be improved by increasing the distance between the object and the image and thus reducing the intensity of the interference [52].

At the same time this technique reduces the image quality because of the increase in geometric unsharpness from finite sources which is directly proportional to the object-image plane separation. Therefore the method is most effective when the geometric unsharpness is relatively small and the degradation of the image by scattered radiation is severe. For isotropic scattering, such as with low-energy neutrons, the reduction in the intensity of the scattered radiation is inversely proportional to the separation distance raised to a power that approaches 2.0 at large distances. At higher neutron energies the scattering becomes increasingly biased in the forward direction, and the reduction in the intensity is not as strongly correlated with separation.

In order to assess the effectiveness of this separation technique for the improvement of fast-neutron image quality, Monte Carlo calculations were made of the differential fluence of scattered neutrons as a function of angle. The geometry for the calculations is shown in Figure 8. Scattered neutrons having energies below 1.5 MeV were not included in the fluence because these neutrons do not contribute significantly to the emulsion response.

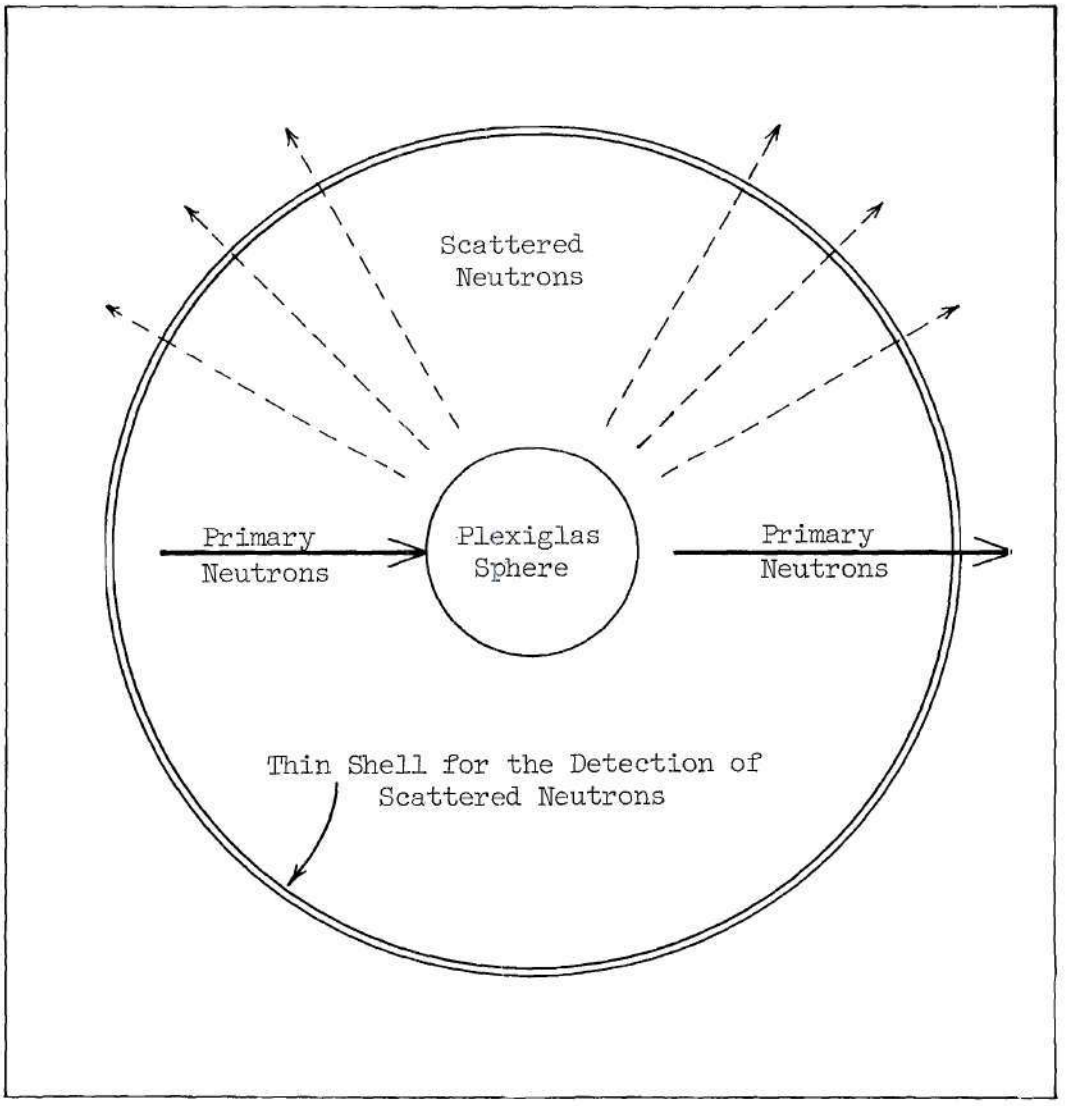

Figure 8. Geometry for the Calculation of the Angular Distribution of Scattered Neutrons

Dosimetry

Neutron Energy Absorption in Biological Materials

Biological media are composed primarily of hydrogen, carbon, nitrogen, and oxygen (see Appendix A). Bone tissues contain the additional elements phosphorus and calcium. Trace elements are present in all tissues, but these elements may be ignored for neutron transport and dosimetry purposes.

Fast neutrons (neutrons having energies above 10 keV) lose energy primarily by elastic and inelastic scattering in tissue. Elastic interactions predominate below 10 MeV, but inelastic interactions become increasingly important above 10 MeV. Nuclear reactions that are significant above 15 MeV can often be ignored at lower energies. For instance, elastic and inelastic interactions account for more than 95 percent of the energy loss of 14-MeV neutrons incident on a thick tissue target [83]. The lower limit of 10 keV for the category "fast neutrons" is chosen for dosimetric reasons because recoil protons having energies less than 10 keV can no longer produce ionization [84] and therefore neutrons of this energy and below cannot be detected by direct ionization measurements. However, this does not mean that the atomic and molecular excitation caused by interactions of intermediate neutrons is of no biological consequence. The fraction of the neutron energy loss due to elastic and inelastic interactions with specific elements in tissue will be discussed in Chapter V, section Dosimetry Calculations.

Fast neutrons that have not escaped or been captured during the slowing down process eventually lose energy and reach thermal equilibrium in tissue. These thermalized neutrons are captured primarily by hydrogen,

by the H(n,γ)D reaction, resulting in the emission of a 2.2-MeV gamma ray and by nitrogen, $^{14}N(n,p)^{14}C$, resulting in the emission of a 0.58-MeV proton and a 50-keV carbon recoil nucleus. The nitrogen interaction results in locally absorbed energy because the proton has a range of less than 10 microns in tissue. The 2.2-MeV gamma ray from the hydrogen interaction may affect any part of the tissue due to the long range of these photons. Obviously, for small masses of tissue (~ one gram or less) the major portion of the dose from thermal neutrons is due to the N(n,p) reaction because the 2.2-MeV gamma ray from the H(n,γ) reaction deposits very little of its energy within one cm of the path length. For larger masses of tissue the contribution of the gamma radiation to the total dose may be the more significant. For fast neutrons from a 14-MeV generator or from ^{252}Cf incident on 20 or 30 cm blocks of tissue, neglecting the gamma contribution to the dose results in underestimates of the dose by a few percent [83]. For ^{252}Cf neutrons the error that results from the neglect of the dose due to gamma and x-radiation originating in the source will be greater.

Calculations

The locally-absorbed contributions to the dose were accumulated as total energy absorbed (in ergs) in the appropriate tissue volumes. After all neutron histories were analyzed, the total energy absorbed in each volume was converted to rads per unit neutron fluence and printed as an array of numbers which could be superimposed on the cross section of the tissue phantom. It is difficult to construct accurate isodose contours from the dose arrays with no further data analysis. Even for 100,000 neutrons per analysis it is difficult to reduce the

volume of tissue below one cm^3 for statistical reasons. For all analyses of broad-beam dosimetry, the assumed volume cell was 60 cm^3 in blocks of one cm^2 cross section oriented parallel to the phantom axis and perpendicular to the beam direction. For narrow-beam geometries, advantage was taken of the circular symmetry of the beam. Comparisons with calculations for square fields indicated no statistically significant difference. The dose was averaged over rings of one cm^2 cross section with outer radii of 0.5, 1.5, 2.5... cm. Isodose contours were derived by a two-step process. First, depth-dose curves were drawn in the beam direction for each traverse at one cm increments from the centerline using the dose points for the appropriate blocks. Next, the 90, 80, ... percent depths were determined from the depth-dose curves, and these points were plotted on the phantom cross section. The isodose curves were then drawn through the series of points corresponding to the 90, 80,... percent depths.

In order to evaluate the validity of the premise that no unacceptable error would result if the calculations of dose neglected contributions from gamma rays and reaction products, a comparison was made with the data of Snyder [83]. These data were also obtained from Monte Carlo calculations but included the contributions of nuclear reactions and gamma rays to the dose.

Standard man tissue composition was used for all homogeneous phantoms (see Appendix A). All of the studies in this series employed right-elliptical phantoms having dimensions of 30 cm major axis by 20 cm minor axis by 60 cm height.

In order to illustrate the disparity that can result when

simulating humans with elliptical, homogeneous phantoms, a heterogeneous phantom was constructed mathematically. (The model was based on Section 26 of A Cross-Section Anatomy, Eycleshymer and Schoemaker [85].) Twenty intersecting surfaces (six planes and 14 quadric surfaces) were required for the mathematical description. These equations are listed in Appendix D. Bone, muscle, and lung tissues were included in the model, and symmetry was assumed in one dimension (60 cm height) in order to simplify the analysis.

CHAPTER V

RESULTS AND DISCUSSION

Line-Spread Distributions

Geometric Unsharpness

Line-spread functions were calculated for disc sources having uniform emission rates. As explained in Chapter IV, the exact geometrical arrangement of source, object, and detector need not be known. Therefore, LSF's were calculated for values of geometric unsharpness ranging from 0.02 mm up to 4.0 mm. Conventional radiographic techniques for thick biological specimens result in geometric unsharpnesses in the order of 0.1 mm to 0.5 mm [52]. These are reasonable values for fast-neutron radiography using ^{252}Cf, but higher values are to be expected from the targets in conventional 14-MeV generators.

Geometric unsharpness is determined by the response of the detector to primary neutrons only. Neutrons that have been scattered lose their original directional identity and must be considered as image-degrading noise.

Spread in Standard-Man Tissue

Line-spread functions were calculated for two thicknesses of tissue of standard man composition for neutrons from ^{252}Cf and 14-MeV sources. For ^{252}Cf neutrons, tissue thicknesses of 5.0 cm transmit 26.0 percent of the primary neutrons, and thicknesses of 20.0 cm transmit 1.6 percent. For 14-MeV neutrons, tissue thicknesses of 5.0 cm

transmit 61 percent of the primary neutrons, and thicknesses of 30.0 cm transmit 5.3 percent. These ranges of tissue thicknesses were used for the LSF calculations and define the approximate ranges for which each neutron source can be used for radiography.

Figures 9 and 10 show the LSF's that were calculated for number-fluence detection and for weighted energy-fluence detection. The LSF's for weighted energy fluence were normalized to 100 at a distance of 0.1 mm perpendicular to the source line. The LSF's for the number fluence are plotted in proper relation to the corresponding energy fluence curves. Note that the separation of the LSF curves is numerically equal to the average energy of the scattered neutrons at each distance from the primary beam. The beam hardening of the scattered neutrons is evident for ^{252}Cf. Figure 11 illustrates the result of the combination of geometric unsharpness of the primary neutrons with the effects due to scattered neutrons in the object on the line-spread function.

Spread in Organic Scintillators

Calculations of the line-spread functions were made for neutrons detected in organic-scintillator imaging devices. Thicknesses of one, two, four, and eight cm were examined for the spread caused by multiple detection of primary neutrons. An inherent unsharpness of 0.5 mm and no geometric unsharpness were assumed for these calculations. Figures 12 and 13 show the results of the calculations for 14-MeV and ^{252}Cf neutrons. These figures illustrate the relative detector response due to the initial interaction of the primary neutron compared with the response due to subsequent multiple detection. As might be expected, multiple detection is more significant for ^{252}Cf neutrons and for the

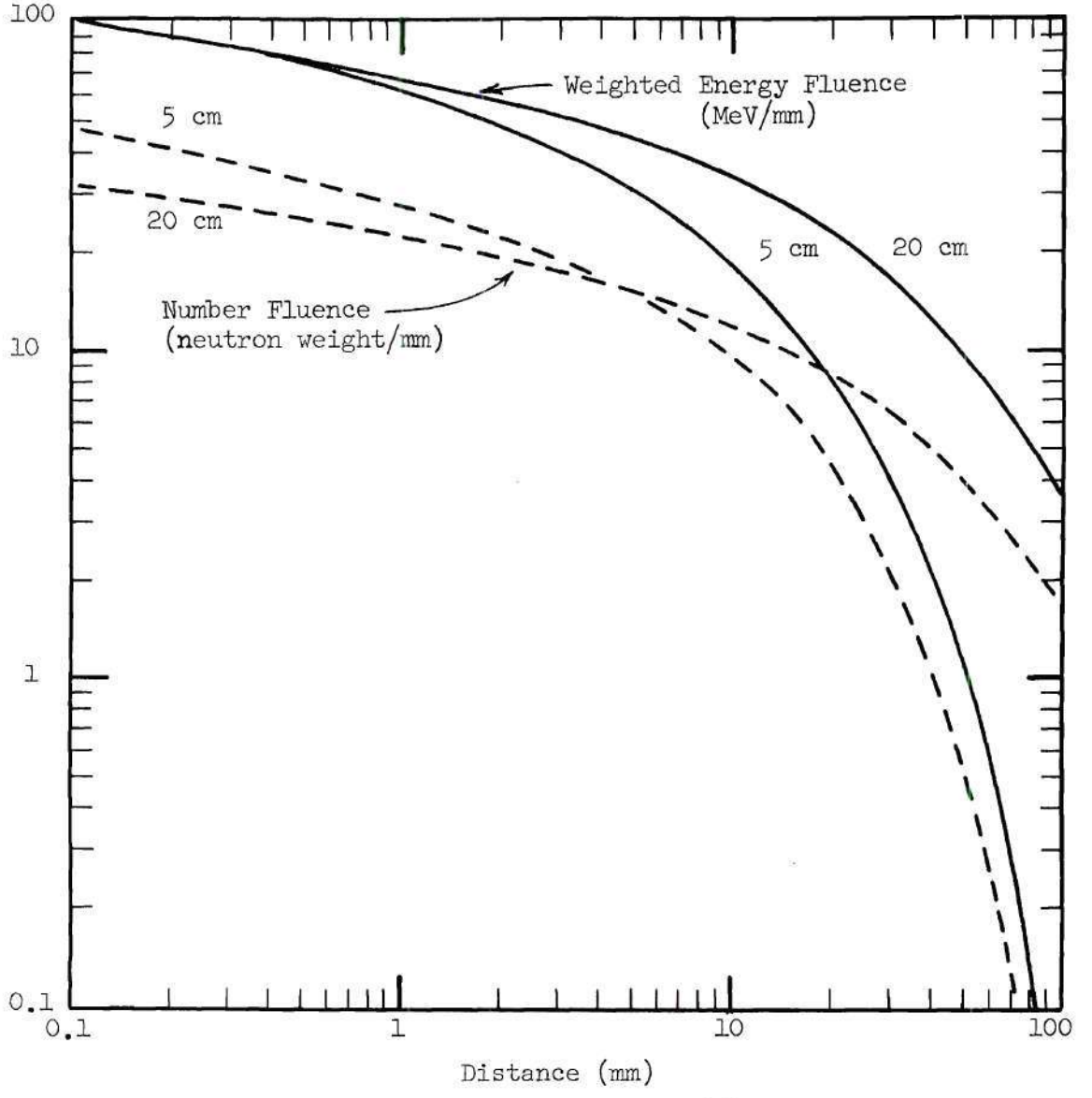

Figure 9. Line-Spread Functions for ^{252}Cf Neutrons Scattered in Standard Man Tissue

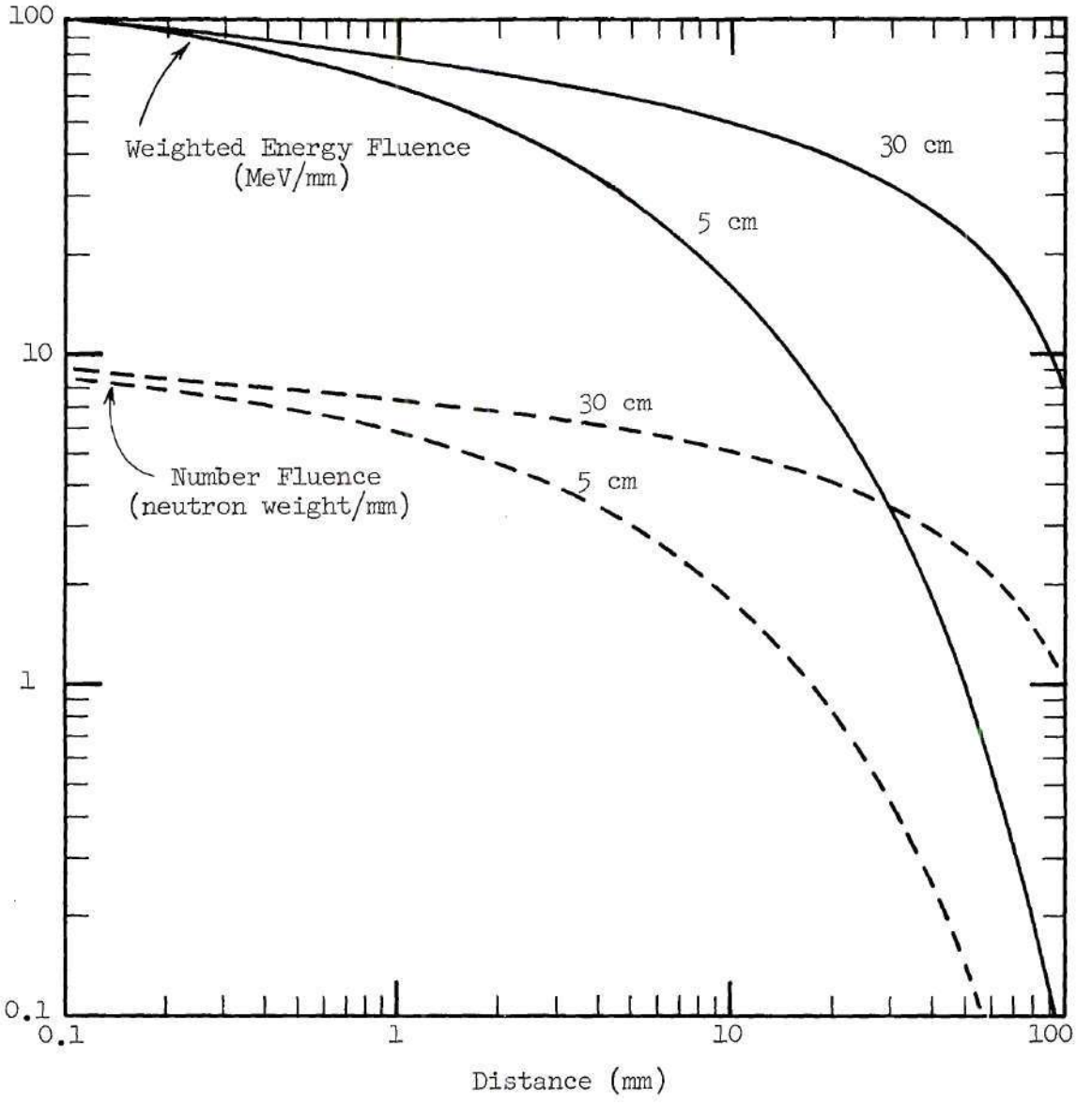

Figure 10. Line-Spread Functions for 14-MeV Neutrons Scattered in Standard Man Tissue

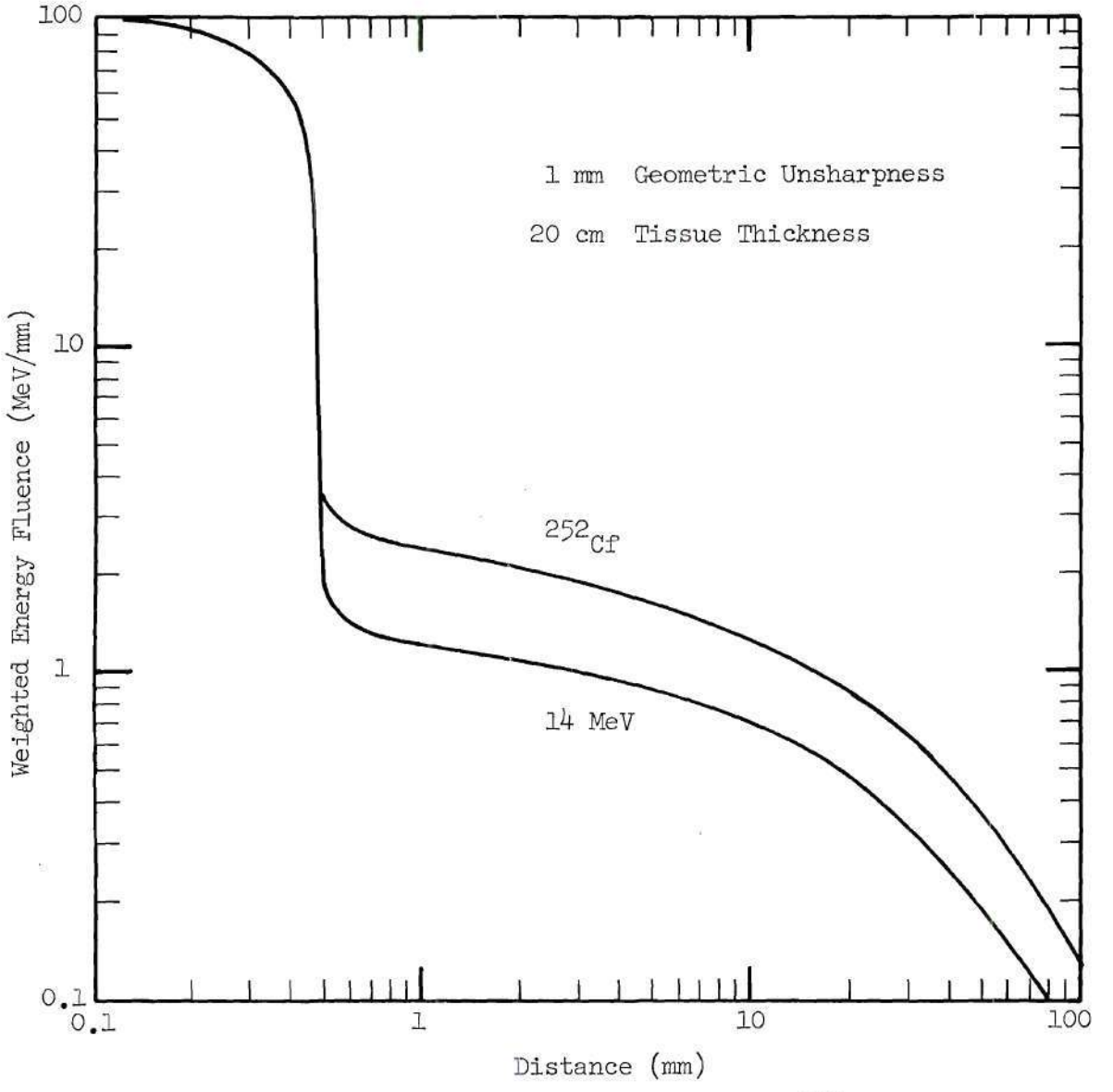

Figure 11. Line-Spread Functions for 14-MeV and ^{252}Cf Neutrons Including Both Scattered Neutrons and the Effect of Geometric Unsharpness on the Primary Neutron Beam

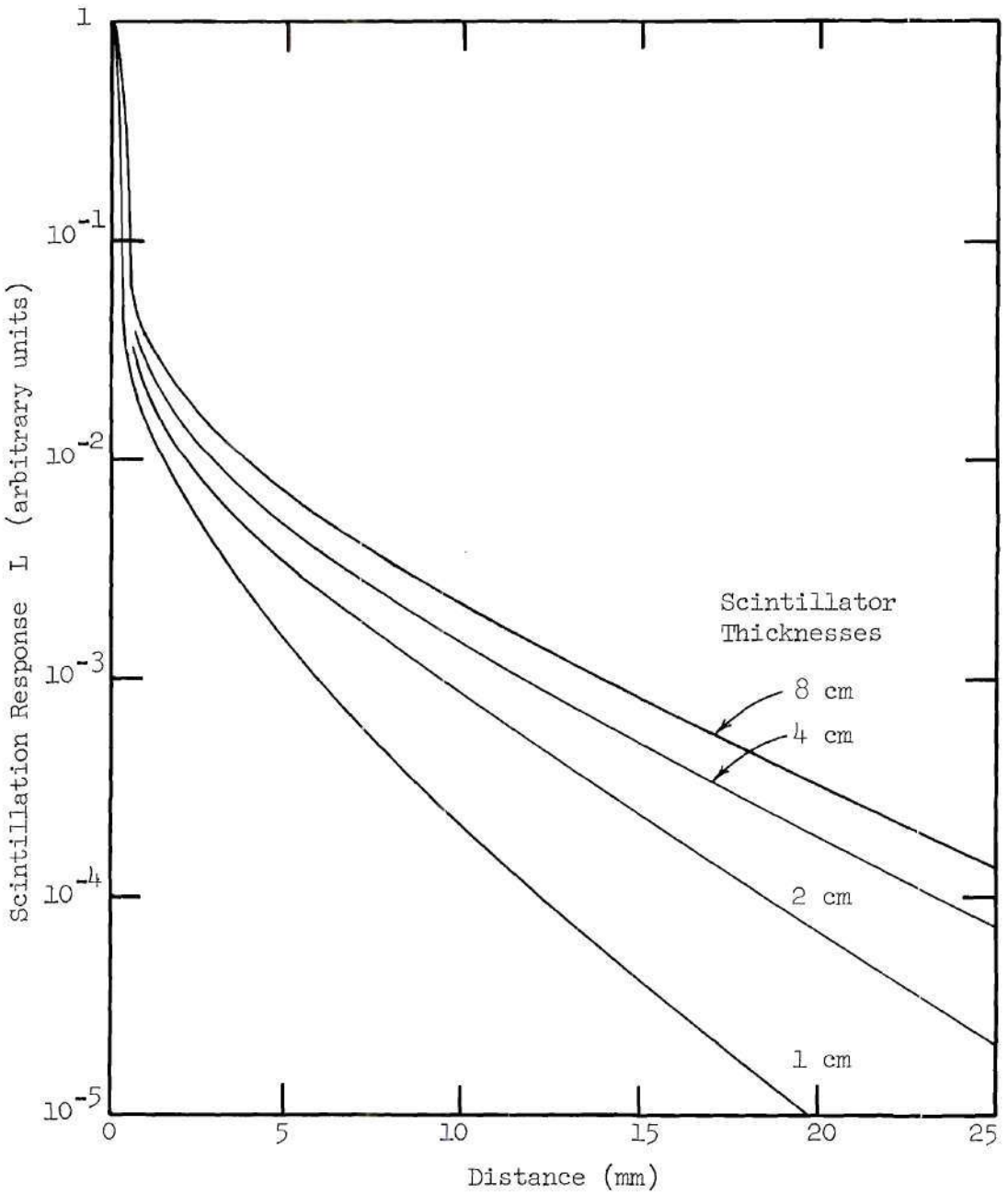

Figure 12. Line-Spread Functions for ^{252}Cf Neutrons Scattered in Organic Scintillators

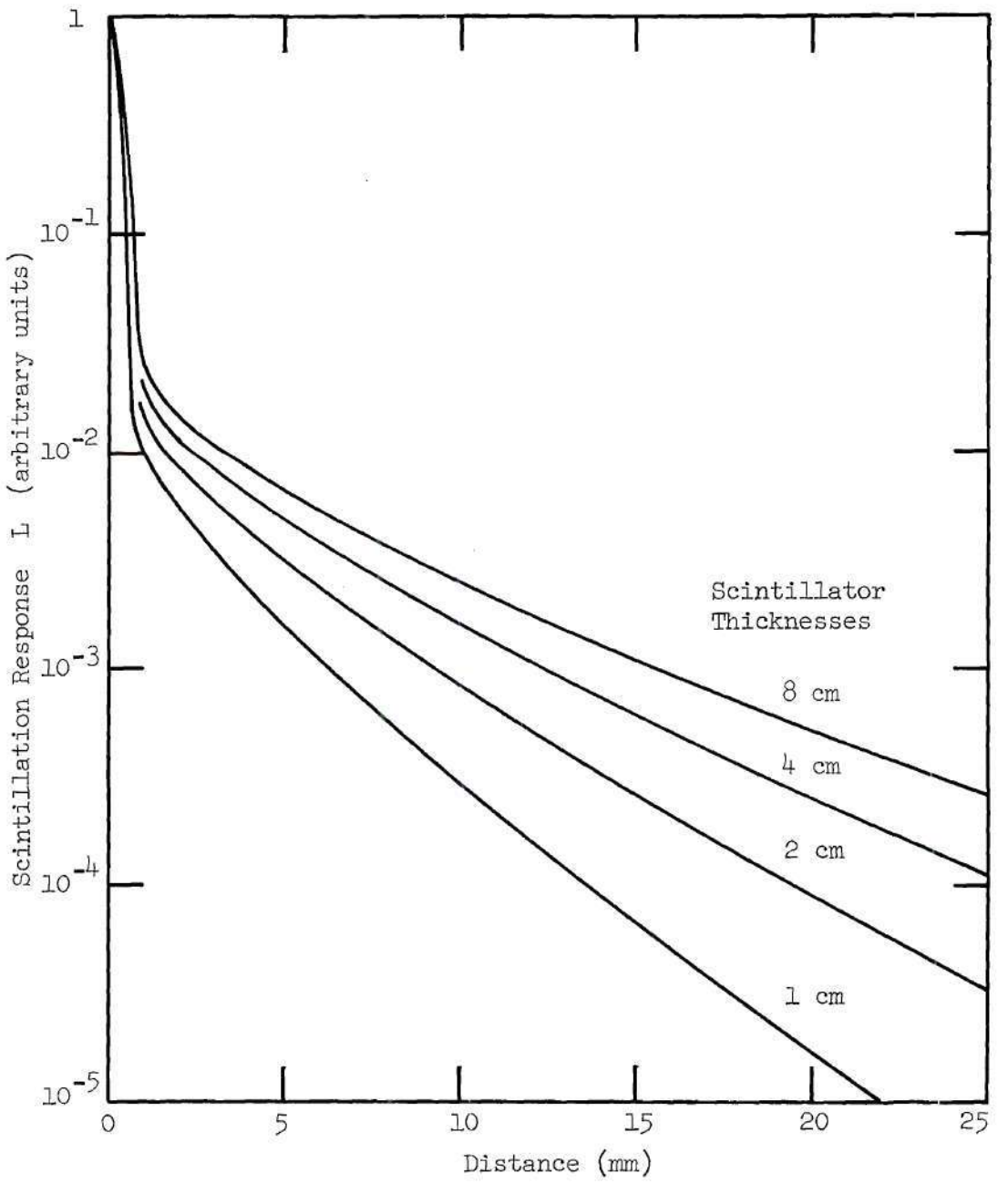

Figure 13. Line-Spread Functions for 14-MeV Neutrons Scattered in Organic Scintillators

thicker scintillators. However, for both types of sources the response from multiply detected neutrons decreases rapidly with distance from the primary neutron direction.

Because neutrons that are scattered in the biological specimen and subsequently enter the scintillator can also be detected (provided their energy is greater than 500 keV), a series of calculations was made to evaluate the relative importance of neutrons scattered by the object compared with primary neutrons that are multiply detected. Calculations were made for 5.0 and 20.0 cm of tissue with a 2.0-cm thick organic scintillator. Figures 14 and 15 show the comparisons for both types of sources. In these figures, the bottom curves, taken from Figures 12 and 13, provide comparisons of the response of the detector from primary neutrons only. It is evident that multiple detection of primary neutrons is considerably less important than the detection of neutrons scattered in the object if the detector thickness is less than one mean free path.

Modulation Transfer Functions

Calculations from LSF's

Figure 16 shows the series of modulation transfer functions corresponding to values of geometric unsharpness from 0.02 mm to 4.0 mm. As might be expected, the shape of these MTF's on a log-log plot is invariant, and the MTF for any value of U_F may be obtained by the proper shift of the frequency scale.

Figure 17 shows the MTF's calculated from the line-spread functions (see Figure 9) for ^{252}Cf neutrons after scattering in tissue. Two

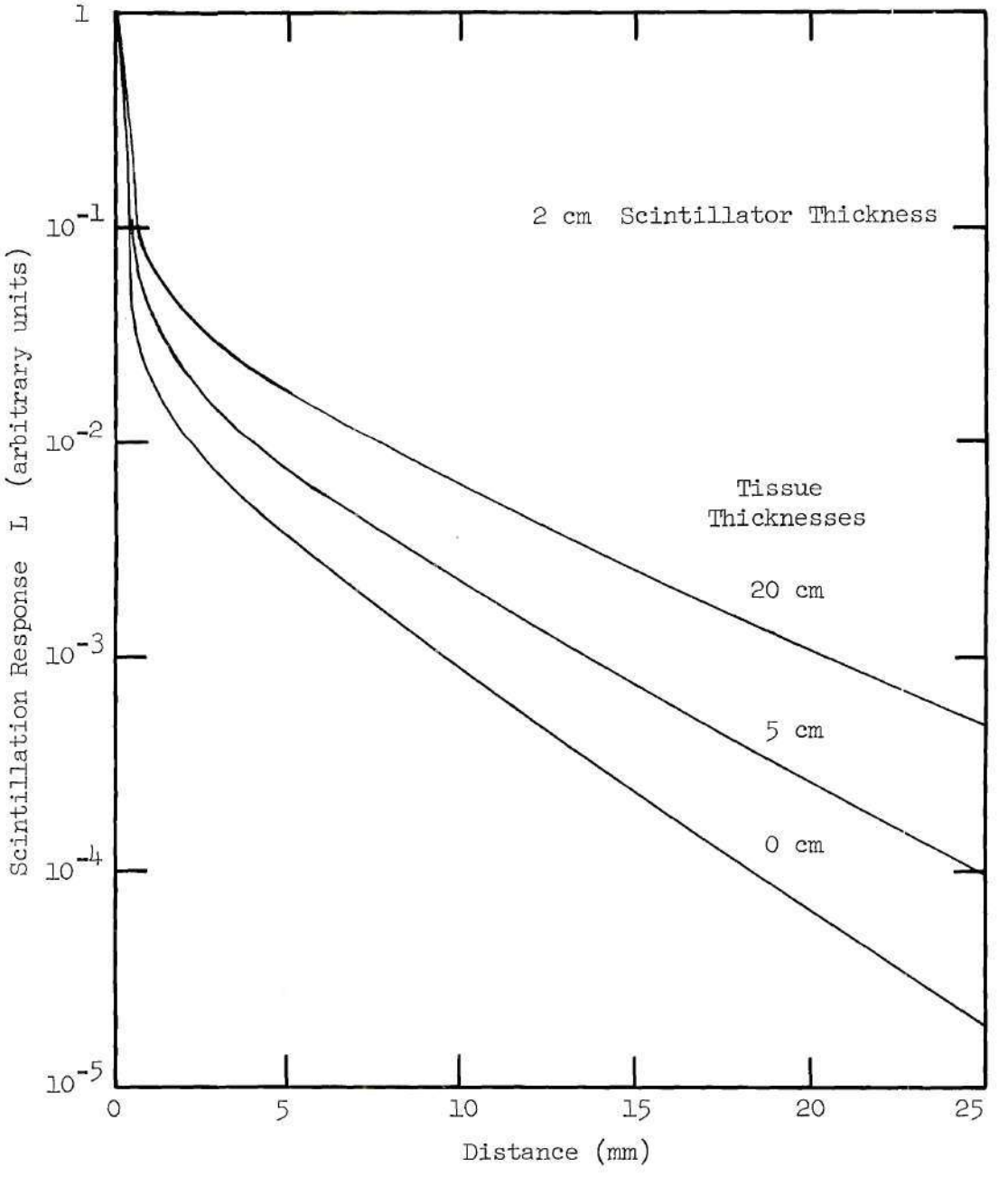

Figure 14. Line-Spread Functions for ^{252}Cf Neutrons Detected in an Organic Scintillator

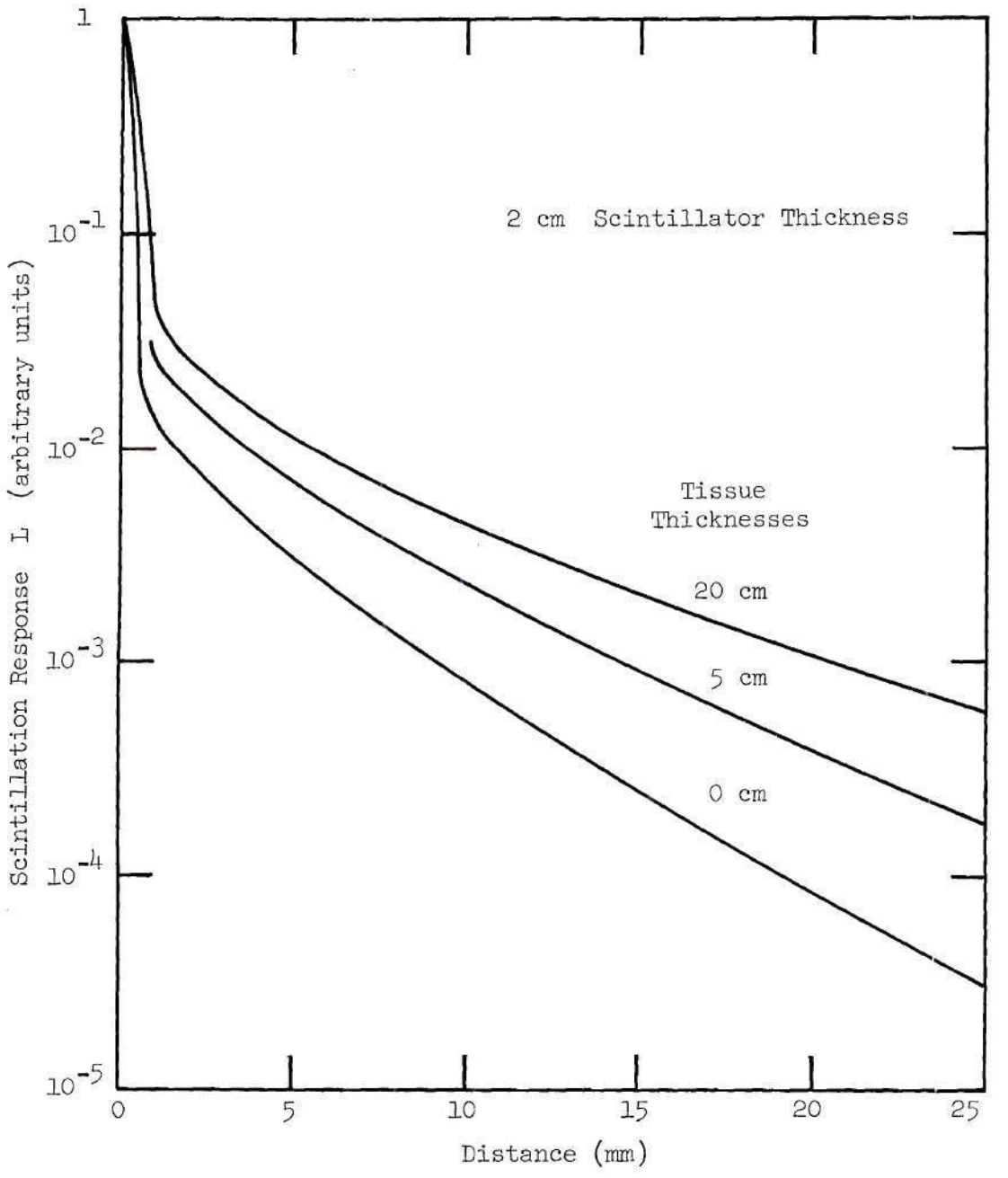

Figure 15. Line-Spread Functions for 14-MeV Neutrons Detected in an Organic Scintillator

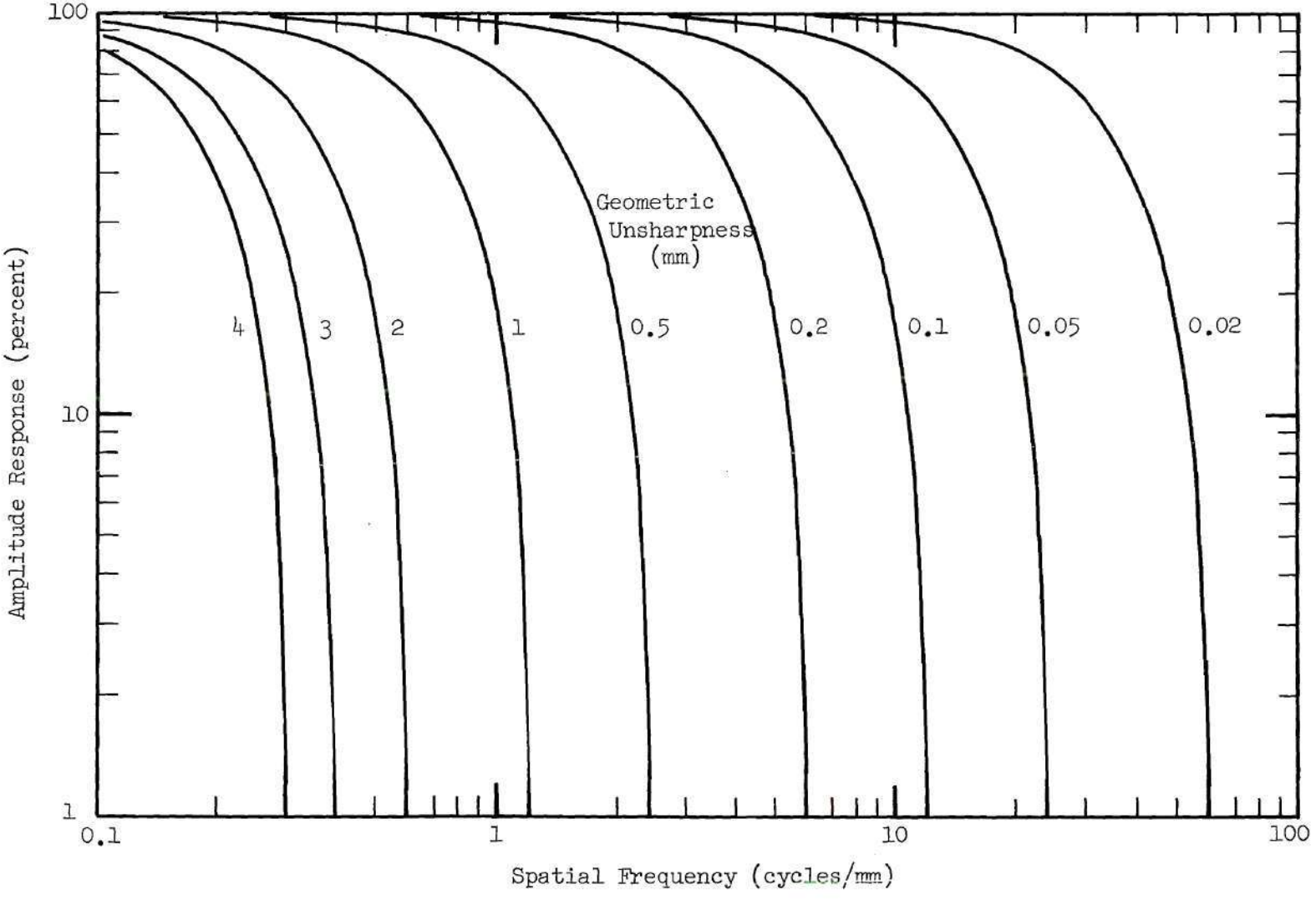

Figure 16. Modulation Transfer Functions for Various Values of Geometric Unsharpness (U_F)

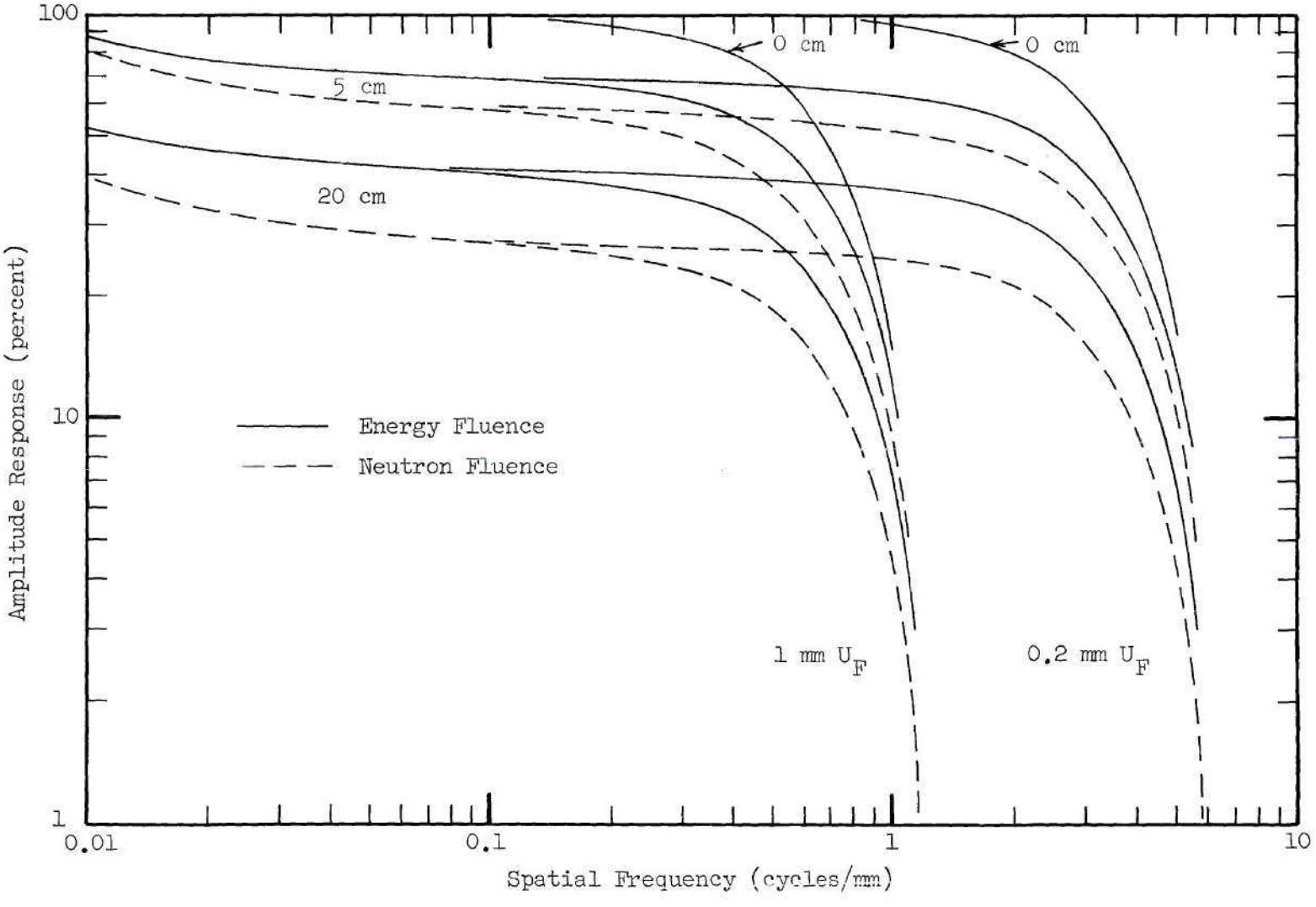

Figure 17. Modulation Transfer Functions for Scatter of ^{252}Cf Neutrons in Tissue

representative values of unsharpness were specified for these calculations. It should be recalled that a value of unsharpness for the detection of primary neutrons must be defined in order for the MTF calculations to have any physical meaning. This follows from the concept of the MTF as a measure of image-forming capability of the primary neutrons. If neither geometric unsharpness nor inherent unsharpness were present, then the value of the line-spread function would be infinite at the point of penetration of the detector plane. Clearly, this is a condition which is physically impossible. The MTF for zero tissue thickness is included from Figure 16 for purposes of comparison. A similar series of MTF's is shown in Figure 18 for 14-MeV neutrons.

Figures 19 and 20 show MTF's for the LSF's for californium-252 and 14-MeV neutrons for 2.0 cm of organic scintillator after the neutrons have been scattered by 0.0, 5.0, and 20.0 cm of standard-man tissue. No geometric unsharpness was included in these calculations because with an imperfect imaging system, having an inherent unsharpness of 0.5 mm, the inclusion of geometric unsharpness was not necessary.

Analysis of MTF's

Comparisons of Figures 17 and 19 for ^{252}Cf neutrons and Figures 18 and 20 for 14-MeV neutrons reveal several significant points. From the shape of the scintillator MTF's it is apparent that response is not identical to the energy-fluence MTF's. This can be attributed to the nonlinear scintillation response as a function of proton energy.

It is apparent from the MTF's that resolving-power measurements alone will not accurately indicate the image-forming quality of fast-neutron radiography systems. The resolution, which is approximately

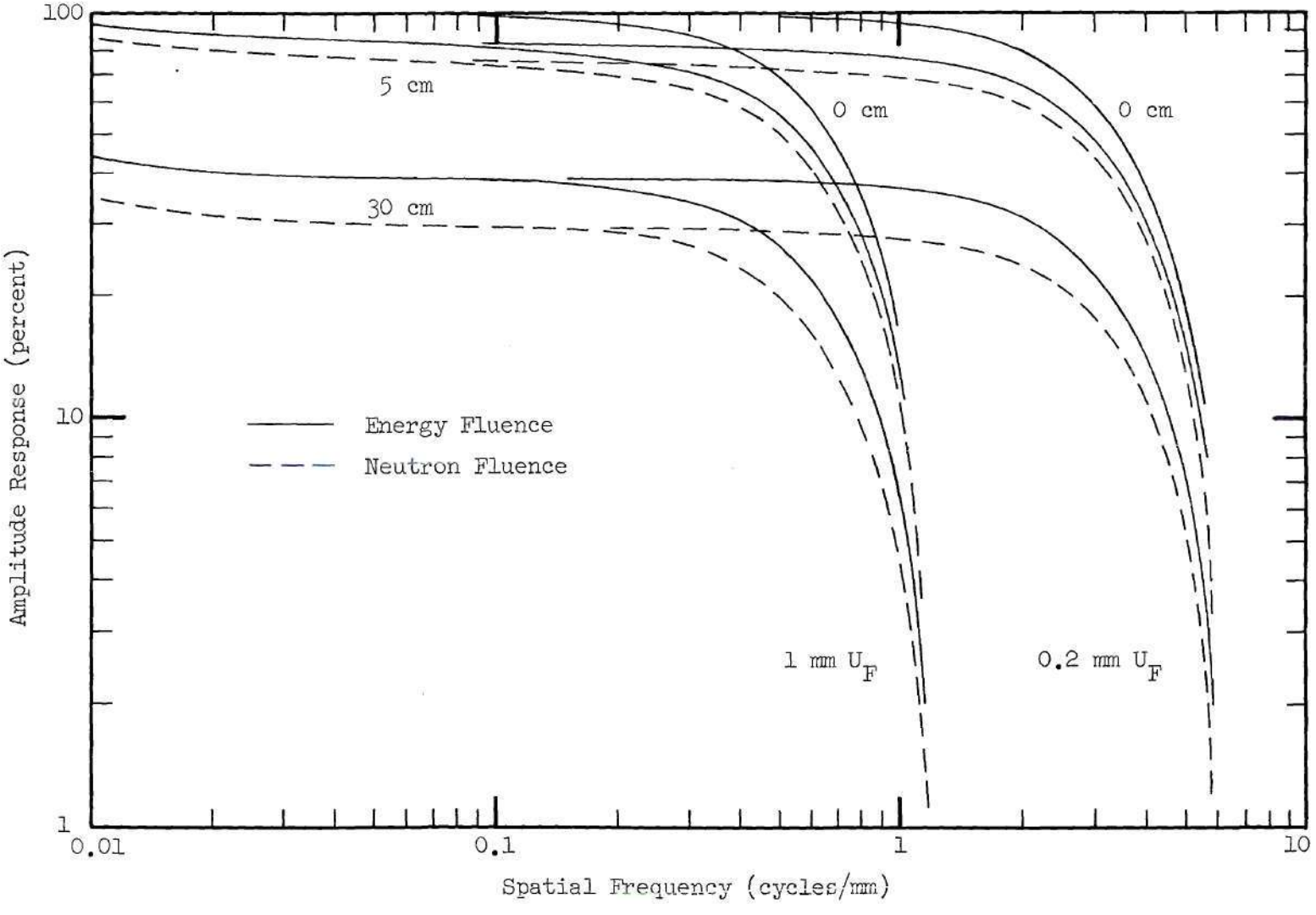

Figure 18. Modulation Transfer Functions for Scatter of 14-MeV Neutrons in Tissue

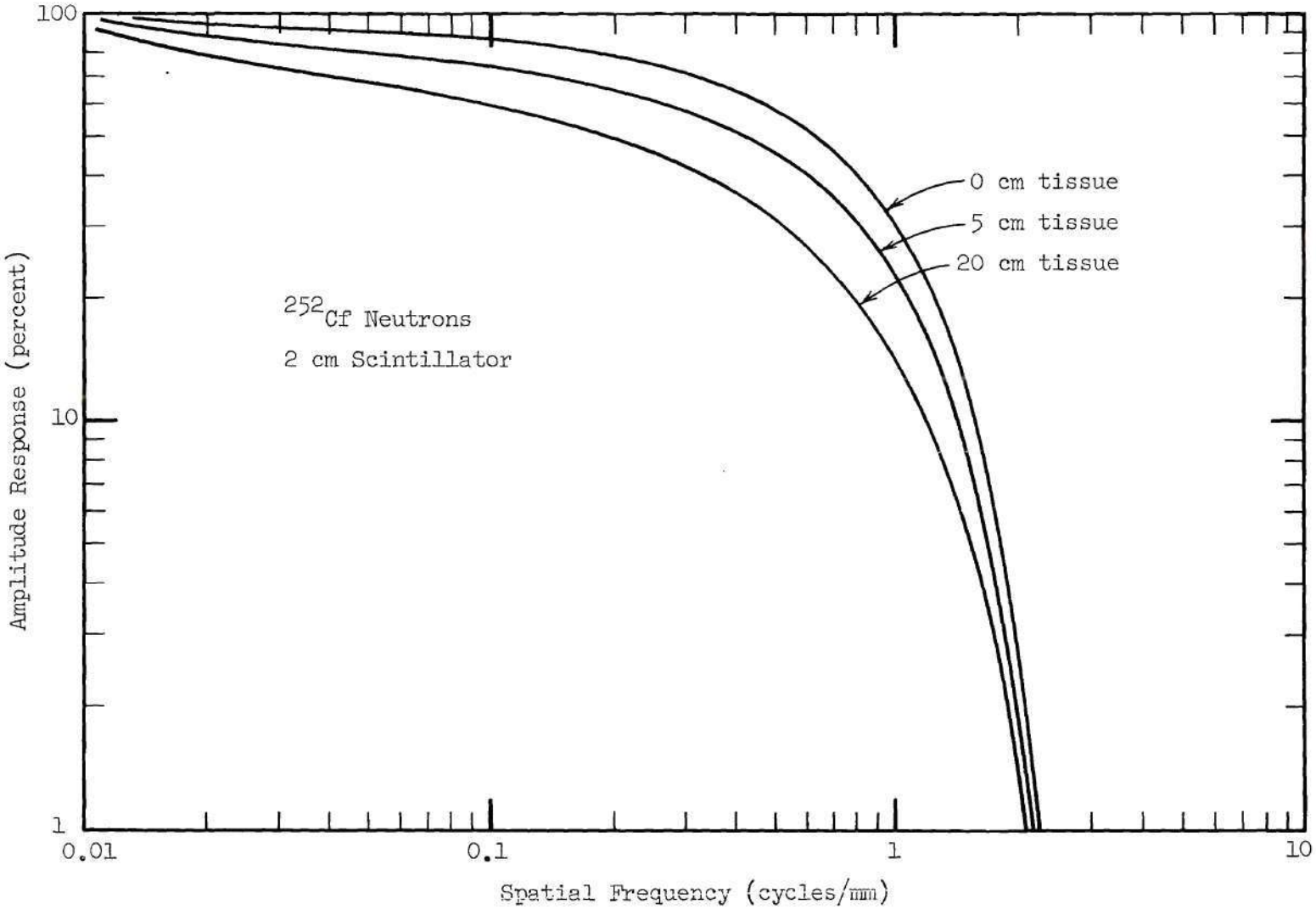

Figure 19. Modulation Transfer Functions for Detection of ^{252}Cf Neutrons in Organic Scintillators

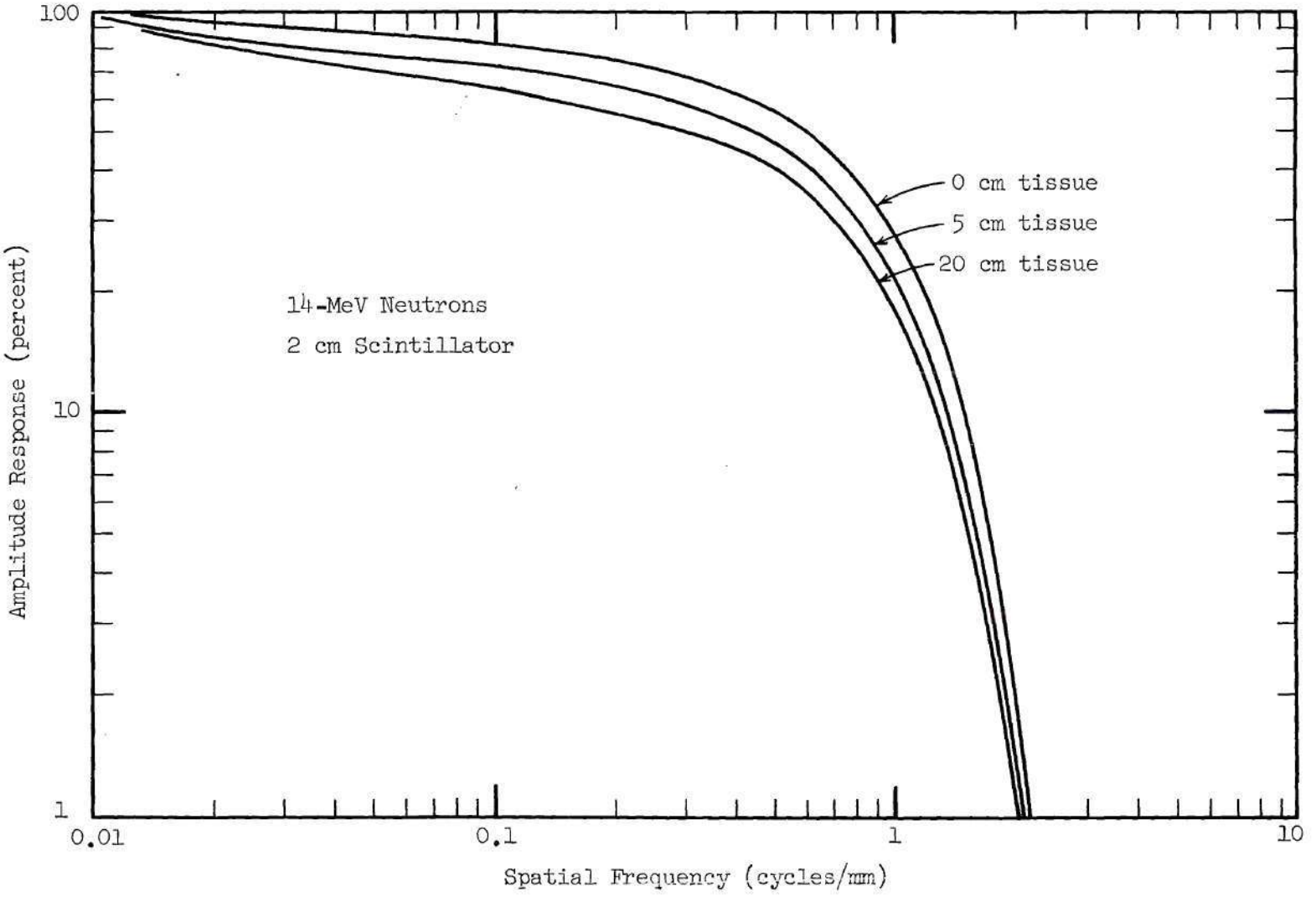

Figure 20. Modulation Transfer Functions for Detection of 14-MeV Neutrons in Organic Scintillators

equal to the spatial frequency at 5.0 percent amplitude response, has about the same value regardless of the amplitude distortion at lower frequencies caused by scattered neutrons. The contrast reduction at lower frequencies will have a pronounced effect on the image-forming quality. Under statistically-limited imaging conditions, such as can be anticipated for fast-neutron radiography of living subjects where both exposure time and dose need to be minimized, the number of events that must be recorded to produce comparable images is inversely proportional to the square of the contrast [89]. Stated in another manner, the product of inherent unsharpness and geometric unsharpness will define the resolution of the system, but the definition which is defined as the clarity with which details are reproduced will be strongly influenced by the amount of amplitude distortion over the entire range of spatial frequencies.

The accuracy of the MTF's was not affected appreciably by the statistical nature of the Monte Carlo calculations because the number of neutron histories was adjusted for each problem so that the standard deviations of the data were kept below about five percent. A more significant but undeterminable effect on accuracy was due to the uncertainties in the neutron cross sections and the composition of biological tissues. Other limitations are due to the assumptions of detector response proportional to number and energy fluences.

In a real system the image-forming quality would be affected by other factors such as the type and form of collimation employed, the scatter from materials other than the object which surround the detector, and the unsharpness due to image intensifiers, videorecorders, etc.

These effects, although real, are removed from the scope of the present research because they cannot be generalized very well and should be examined for each specific system under consideration.

Synthetic and Experimental Radiographs

Angular Distributions of Scattering

Monte Carlo analyses of the differential fluence as a function of scattering angle were made for ^{252}Cf and 14-MeV neutrons incident on Plexiglas of thicknesses of 5.0 cm and 20.0 cm. Figures 21 and 22 show calculations of the cumulative distribution functions as a function of scattering angle of the number and energy fluence of scattered neutrons for Plexiglas spheres of 5.0 and 20.0 cm diameter. For comparison, the dotted lines indicate the shape of the cumulative distribution functions for scattering that is isotropic in the laboratory system with one half the scattering at angles less than 90 degrees. Both ^{252}Cf and 14-MeV neutrons are scattered predominantly in the forward direction. Approximately 90 percent of the scattered fluence, both number and energy, for 14-MeV neutrons is scattered in the forward direction. For a ^{252}Cf source a shift toward isotropicity is seen with the increase in thickness from 5.0 cm to 20.0 cm. For 5.0 cm of Plexiglas, about 90 percent of the number and energy fluence is scattered in the forward direction. Approximately 73 percent of the fluence is scattered forward from 20-cm thick Plexiglas.

These results indicate that, for a 14-MeV source, little improvement in image-quality would be realized by separation of the detector from the object. With ^{252}Cf, some improvement might result from this separation for the radiography of thick tissues.

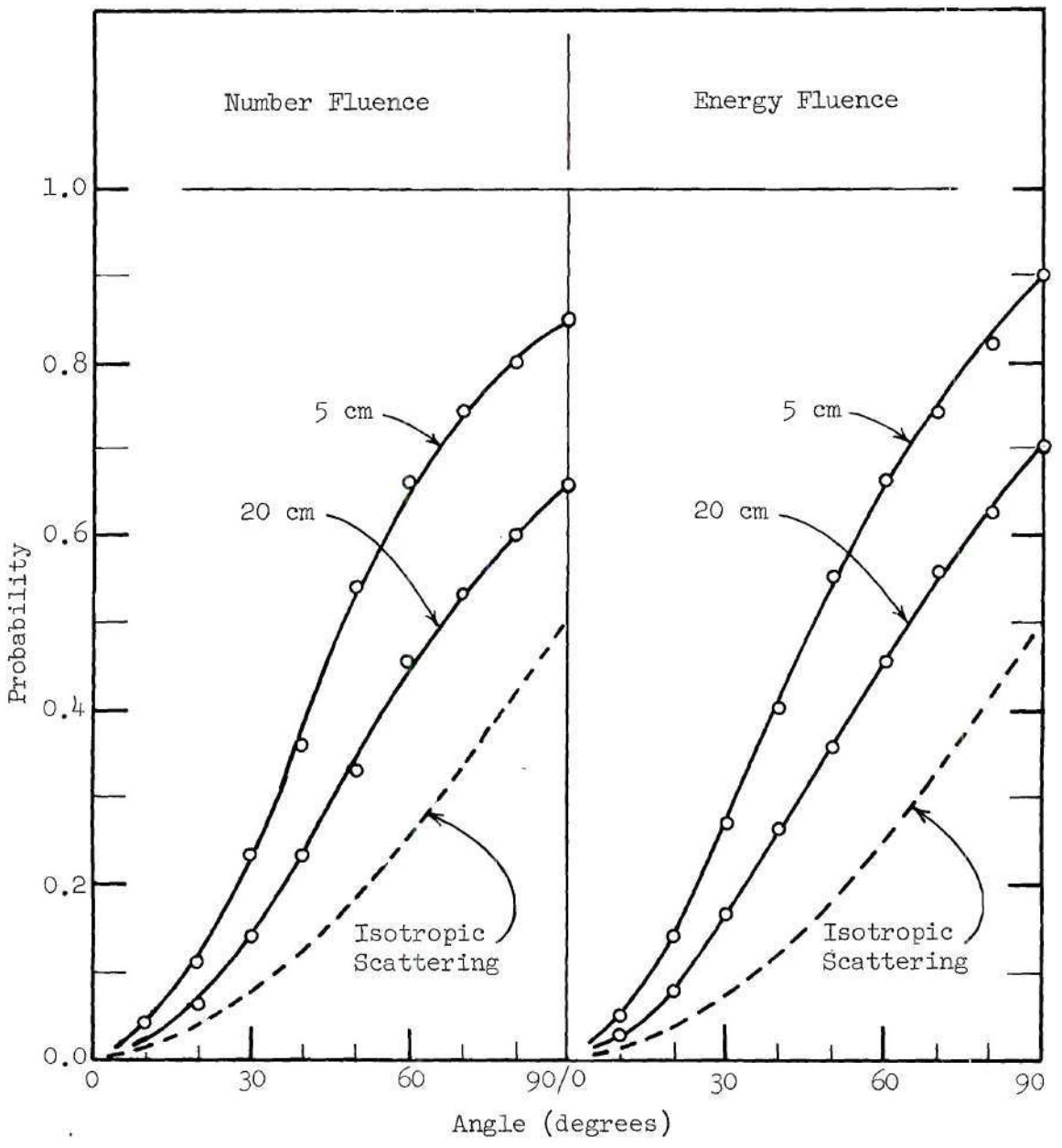

Figure 21. Cumulative Distribution Functions of Scattered ^{252}Cf Neutrons

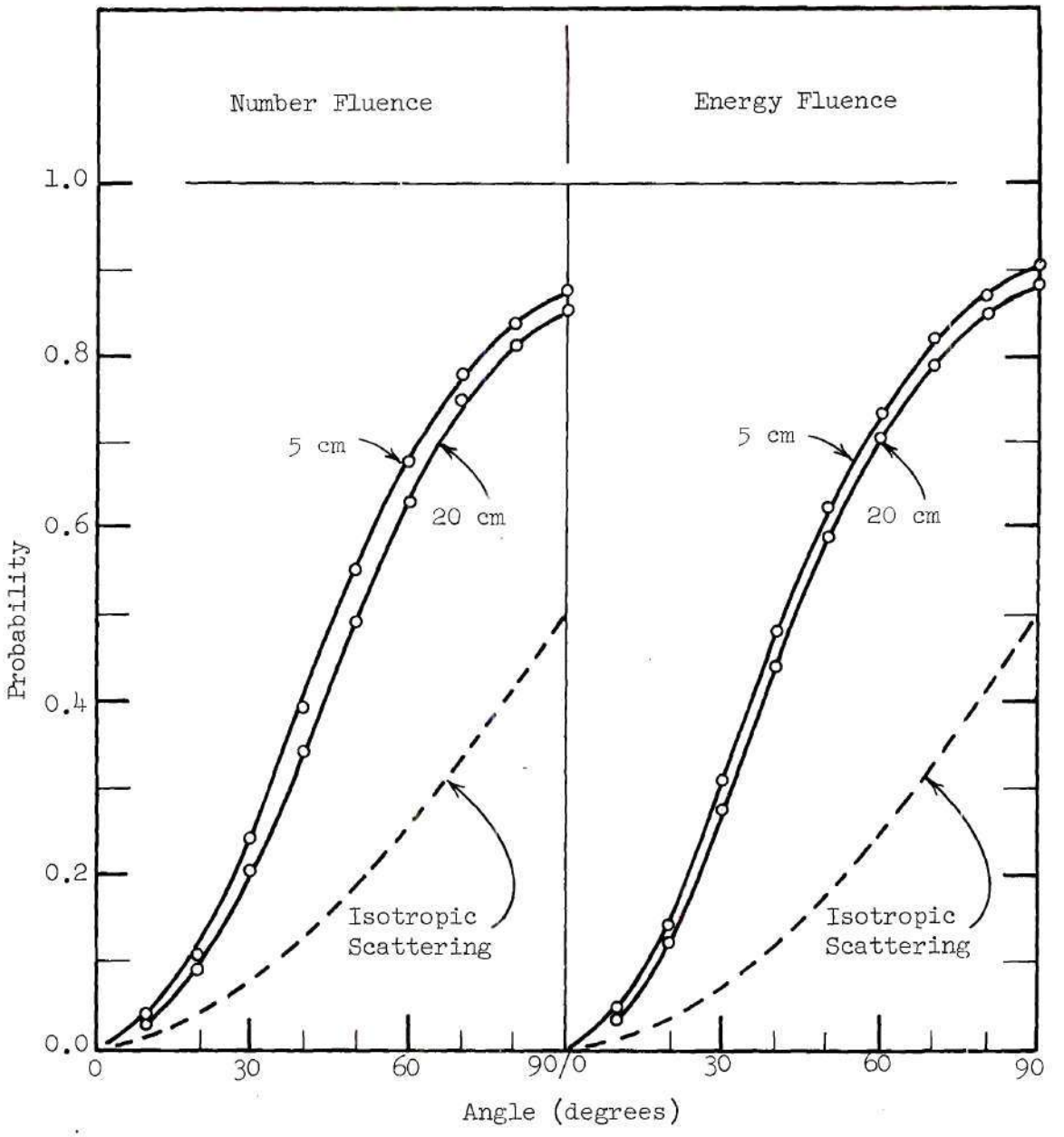

Figure 22. Cumulative Distribution Functions of Scattered 14-MeV Neutrons

Radiographs

After calculating the neutron penetration of the Plexiglas object, it is then necessary to know the probable energy deposition in the photographic emulsion for each neutron. It is this energy deposition that results in the transformation of the beam image into the visible image. As discussed in Chapter IV, section Synthetic Radiographs, energy is deposited in the photographic emulsion by protons that are ejected from a thin sheet of Plexiglas that is located adjacent to the photographic emulsion. If the Plexiglas is assumed to be thin, i.e. much less than one mean free path, then the interaction probability per neutron is uniform at any depth and is proportional to the hydrogen elastic scattering cross section σ_s. After an interaction depth is selected from a uniform distribution, the angle and energy of proton recoil must be selected. Elastic scattering of neutrons by hydrogen is essentially isotropic in the center-of-mass system for energies less than 14 MeV. It can be shown that the relation between the proton angle of scattering θ in the laboratory system is related to the center-of-mass scattering angle φ by the relation

$$\theta = \frac{\pi - \varphi}{2} \tag{5.1}$$

Because the probability of scattering around φ is

$$p(\varphi)\, d\varphi = \frac{2\pi r^2 \sin\varphi\, d\varphi}{4\pi r^2} = \frac{\sin\varphi\, d\varphi}{2} \tag{5.2}$$

$$p(\theta)\, d\theta = -\sin 2\theta\, d\theta = \frac{1}{2}\, d(\cos 2\theta) \tag{5.3}$$

Integration gives the probability of proton scattering between angle θ_1 and θ_2 as

$$P = \int_{\theta_2}^{\theta_1} \frac{1}{2} d(\cos 2\theta) = \frac{1}{2}\left[\cos 2\theta_1 - \cos 2\theta_2\right] \tag{5.4}$$

After a scattering angle θ is selected from the probability density function $P(\theta)$, the energy E_p may be calculated from

$$E_p = E_n \cos^2\theta \tag{5.5}$$

After the interaction depth and angle and energy of proton recoil are known, the next step is to determine if the proton can escape the radiator and deposit energy in the emulsion. For protons in Plexiglas the range data reported in the literature are inconsistent and incomplete. Therefore, calculations for the range R_1 were made from the relation [86]

$$\frac{1}{R_1} = \frac{W_H}{R_H} + \frac{W_C}{R_C} + \frac{W_O}{R_O} \tag{5.6}$$

where W_i are the weight fractions of H, C, and O. Figure 23 shows a plot of the points calculated using Equation 5.6. The solid line in Figure 23 was calculated from Equation 5.7 which was empirically derived to give the best fit to the plotted points.

$$R_1 = 0.00187\,[E_p + 0.11]^{1.775} \tag{5.7}$$

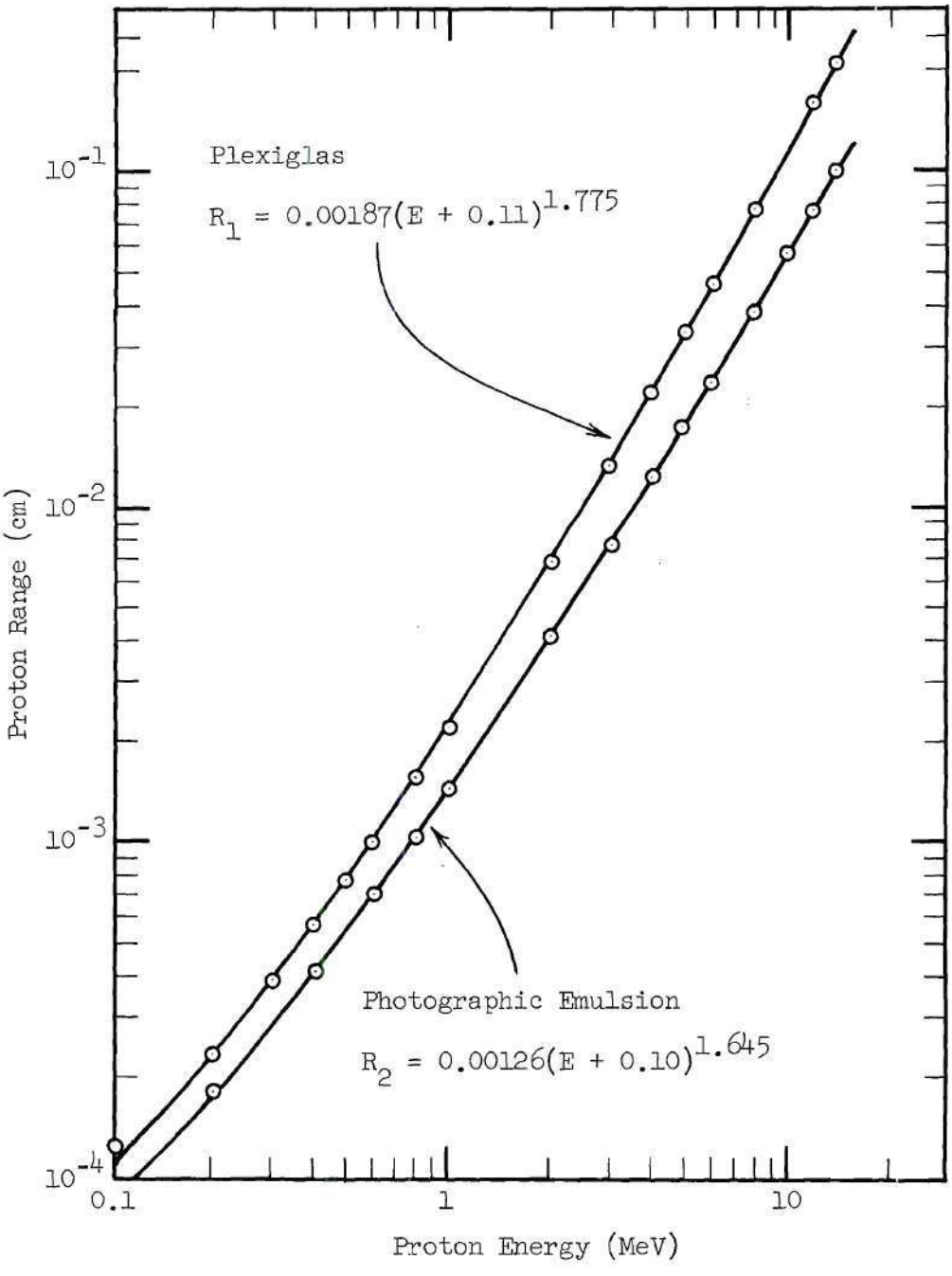

Figure 23. Ranges of Protons in Plexiglas and in Photographic Emulsion

This equation fits the points within ± 3 percent over the range of proton energies of 0.1 MeV to 14 MeV. If the range of protons in the Plexiglas radiator is sufficient to permit escape and subsequent penetration of the emulsion, the escape energy may be found from insertion of the residual range into the inverse of Equation 5.7

$$E_p = 34.4\ R_1^{0.5634} - 0.11 \qquad (5.8)$$

Data of Barkas [87] were used for the range-energy relation for protons in a "standard emulsion" of density 3.815 g/cm^3. These data points are also shown in Figure 23. A similar empirical relation

$$R_2 = 0.00126\ [E + 0.10]^{1.645} \qquad (5.9)$$

was fitted to these points with a precision of ± 4 percent over the range of 0.1 MeV to 14 MeV. From these data, the energy deposition for a proton of a given energy and entrance angle was calculated. If the path length in the emulsion was greater than the range R_{max}, then the exit energy calculated from the inverse of Equation 5.9

$$E_p = 58.0\ R_2^{0.6080} - 0.10 \qquad (5.10)$$

was subtracted from the entrance energy to obtain the energy deposited in the emulsion.

In order to make the analysis efficient, the probability density functions of energy depositions for a given incident neutron were

calculated on a PDP-8/I computer, and this information was supplied to the Univac-1108 analysis code in the form of cumulative distribution functions. Probability density functions of energy deposition in the emulsion were obtained for neutron energies of 2.0 to 14 MeV in steps of one MeV and for scattering angles from zero to 90 degrees in five-degree increments and for interaction thicknesses of 0.0025 cm to 0.22 cm in increments of 0.005 cm. Six representative probability density functions are shown in Figure 24. The corresponding cumulative distribution functions were then used for the Univac-1108 analysis of neutron histories.

In this manner, an estimate was made by Monte Carlo calculations of the weighted energy fluence of neutrons impinging on the detector. Then an estimate was made of the proton energy deposition density in the emulsion as a function of perpendicular distance from the center-line of the image. This array of numbers forming the energy-density trace was converted to punched paper tape and inserted into the PDP-8/I computer. The data were smoothed by an averaging procedure and scaled to an integer array whose elements had values from zero to an arbitrary maximum number N. A series of exposures with various values for N indicated that N = 25 was the best choice. Another series of exposures demonstrated that the best averaging procedure combined the three points on either side of each data point to produce a smoothed energy-density function. An oscilloscope display then was used to obtain a photographic image of the Plexiglas phantom. The Y-deflection voltage was increased in 1000 equal steps, while at each Y position, the sweep was triggered the number of times between zero and N proportional to the value of the emulsion energy-density trace.

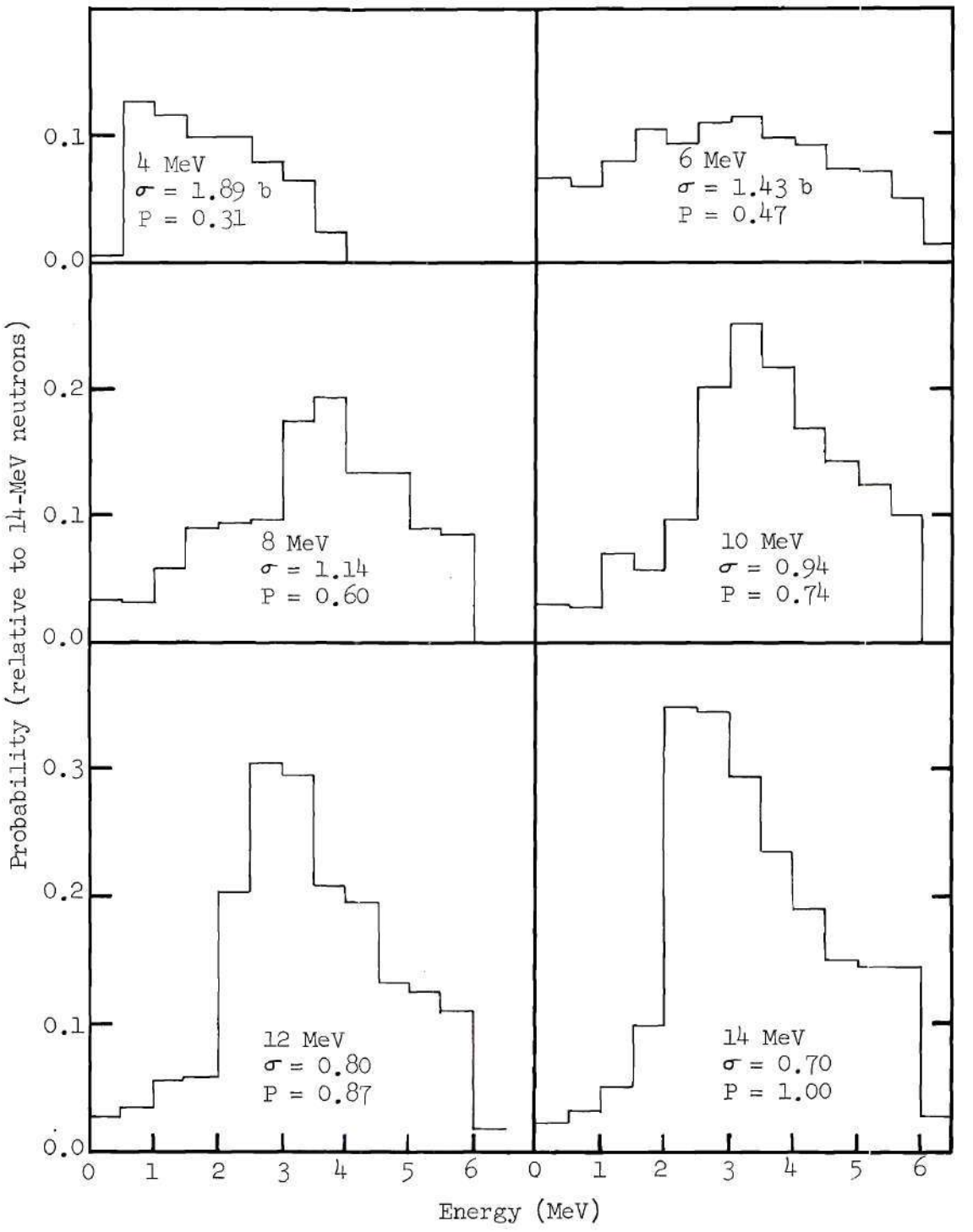

Figure 24. Probability of Energy Deposition in the Photographic Emulsion for Selected Energies of Incident Neutrons

Each Plexiglas block contained an axial hole 1.9 cm in diameter. Using a total attenuation coefficient for 14-MeV neutrons in Plexiglas of 0.119 cm^{-1}, the maximum ideal object contrast C was calculated to be 0.11. The computer code separated the emulsion response to primary neutrons from the response to scattered neutrons and printed out this information in addition to the total response. In this manner, an estimate could be made of the degradation in the image quality by scattered neutrons. Contrast calculations were made using the relative exposure values that were obtained from the corresponding optical densities on the characteristic curves. Figure 25 shows the data for NS-54T film. A close correlation exists in the data for film exposures to fast neutrons [53] and the data for film exposures to light produced by the oscilloscope display. The results were normalized at an optical density of 2.0 (the upper limit of density that is useful in medical radiography) and at 0.375 (the density corresponding to no exposure to fast neutrons).

The contrast values are summarized in Table 5. Synthetic radiographs for a ^{252}Cf source were included for comparison. The synthetic radiographs showed obvious statistical fluctuations, even though each calculation included the histories of 400,000 neutrons. The radiographic contrast for the primary neutrons was close to the theoretical value of the object contrast of 0.11. The image degradation of the synthetic radiographs was apparent when the response estimates of scattered neutrons were included, but the inclusion of this factor alone did not result in contrasts as low as was observed experimentally. The descrepancy could have resulted from the degradation of the image

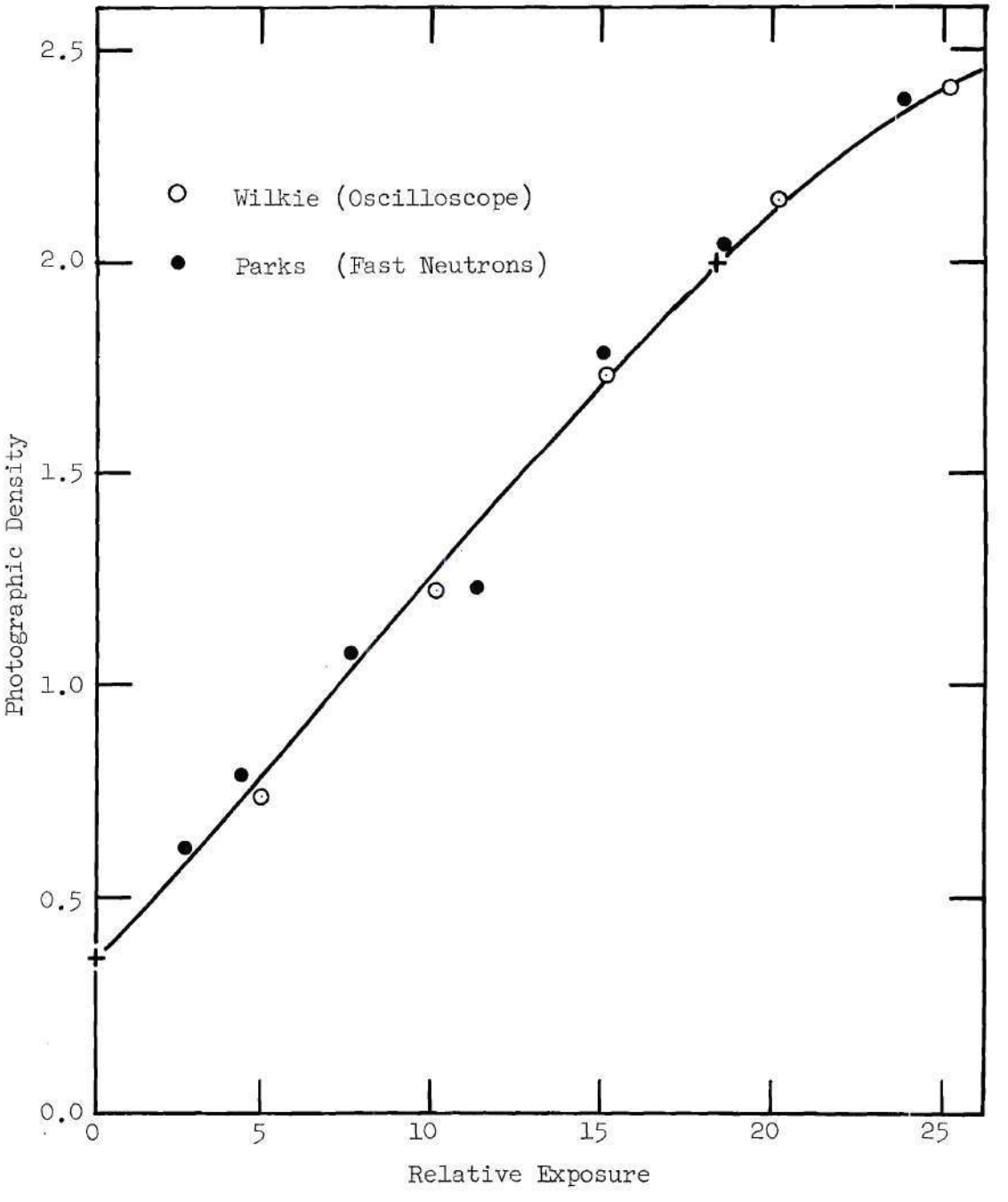

Figure 25. Characteristic Curves for NS-54T Film

Table 5. Object Contrast in Synthetic and Experimental Radiographs

Neutron Source	Plexiglas Thickness (cm)	Detector Separation (cm)	Contrasts		
			Experimental	Theoretical	
				Total	Primary
14-MeV	5	0	0.0400	0.091	0.112
	5	50	0.0315	0.057	0.088
	15	0	0.0243	0.096	0.108
	15	50		0.101	0.116
^{252}Cf	5	0		0.110	0.146
	15	0		0.112	0.174

by the film response to gamma rays from the capture of the neutrons by hydrogen. This factor was not included in the synthetic radiographs. The difference also could have been due partly to inaccuracies in the assumptions inherent in the mathematical model of the emulsion response function. It should be emphasized that the enhanced contrast in the synthetic radiographs was not a result of inaccuracies in the calculations of the fluences of primary and scattered neutrons penetrating the object. Figure 26 shows density plots for an experimental radiograph for 5.0-cm thick Plexiglas compared with the corresponding density plots for synthetic radiographs for ^{252}Cf and 14-MeV neutrons.

Dosimetry Calculations

Figure 27 presents broad-beam, centerline, depth-dose calculations for phantoms containing H, C, N, and O in the proportions of standard man tissue composition.

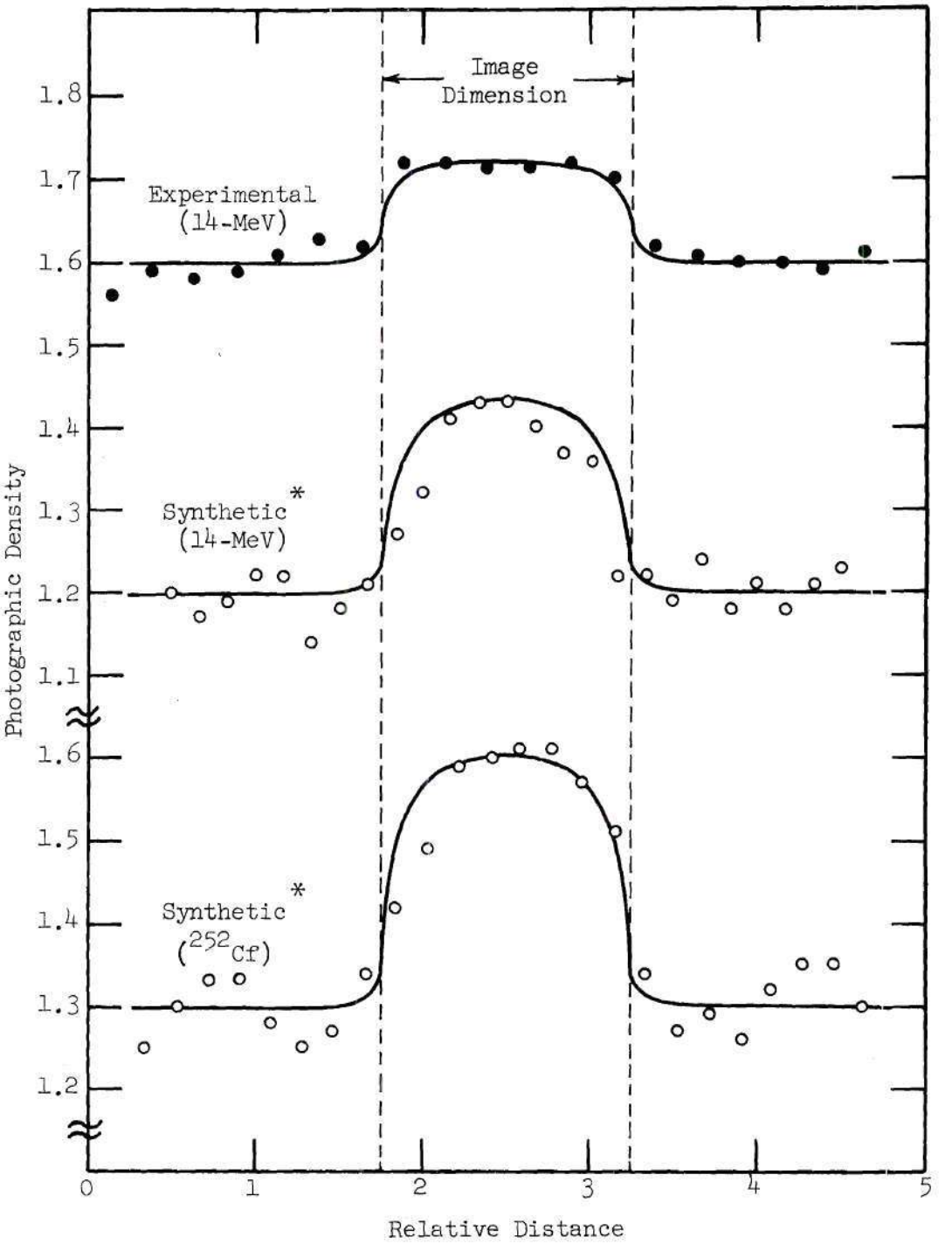

Figure 26. Comparison of Experimental and Synthetic Radiographs

* NOTE: These curves are not directly related to neutron fluence.

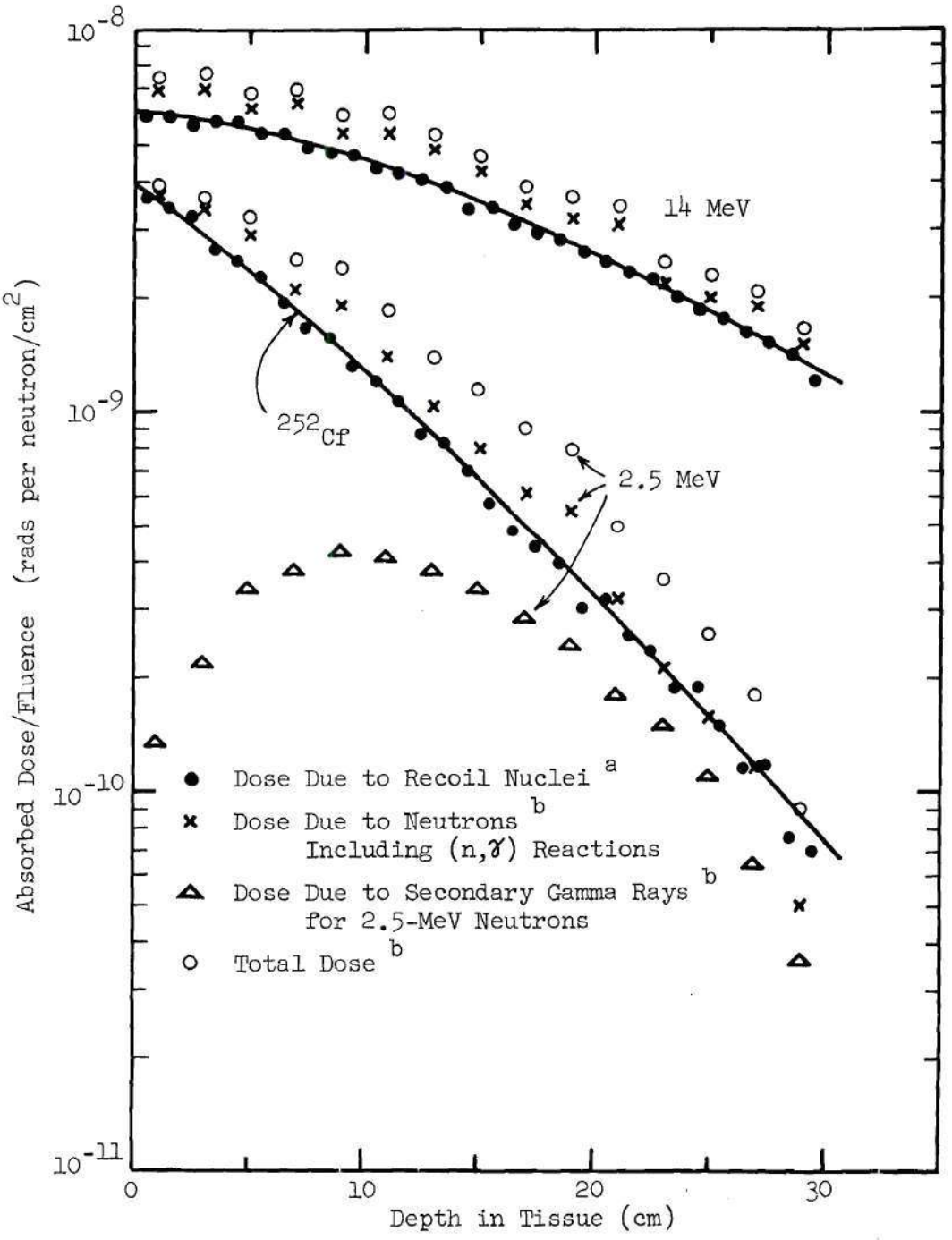

Figure 27. Comparison of Centerline Depth-Dose Calculations
[a]This Work, [b]Snyder [83]

Snyder's data [83] are plotted for comparison with data obtained with the calculational model developed for the current research. The efficiency and rigor with which inelastic interactions are treated in the author's work permitted the examination of large numbers of neutrons for each problem as well as the examination of heterogeneous phantoms. Snyder's data include estimates of the dose from (n,α) reactions and gamma-ray interactions, but the inclusion of these factors in the current research would have required a sacrifice in the precision of the dose estimates as well as a reduction in the number and variety of different systems studied due to considerations of computer economics. It is evident from Figure 27 that a simple correction could be made if the higher dose estimate were thought to be more accurate. The ^{252}Cf data and the 2.5-MeV data are only qualitatively comparable due to the continuous energy distribution of the ^{252}Cf neutrons.

Homogeneous Tissue

Two broad-beam studies and six narrow-beam studies were completed. These are described in Table 6 which also gives the corresponding figure numbers. Calculations for 14-MeV neutrons at 125 cm SSD were made for the purpose of comparison with the experimental measurements of Brennan [88]. These data were obtained with a 14-MeV generator at the Lawrence Radiation Laboratory. The theoretical and experimental curves are in close agreement with the minor differences being attributable to a higher experimental source energy of the LRL generator (15 MeV average energy).

Table 6. Computed Doses in Elliptical, Homogeneous Phantons

Figure	Source	Field Size	SSD	No. of Neutrons
28	^{252}Cf	5 cm	50 cm	25 K
29	^{252}Cf	10 cm	100 cm	40 K
30	^{252}Cf	Broad	∞	100 K
31	14-MeV	5 cm	50 cm	40 K
32	14-MeV	5 cm	125 cm	50 K
33	14-MeV	10 cm	100 cm	50 K
34	14-MeV	10 cm	125 cm	50 K
35	14-MeV	Broad	∞	100 K

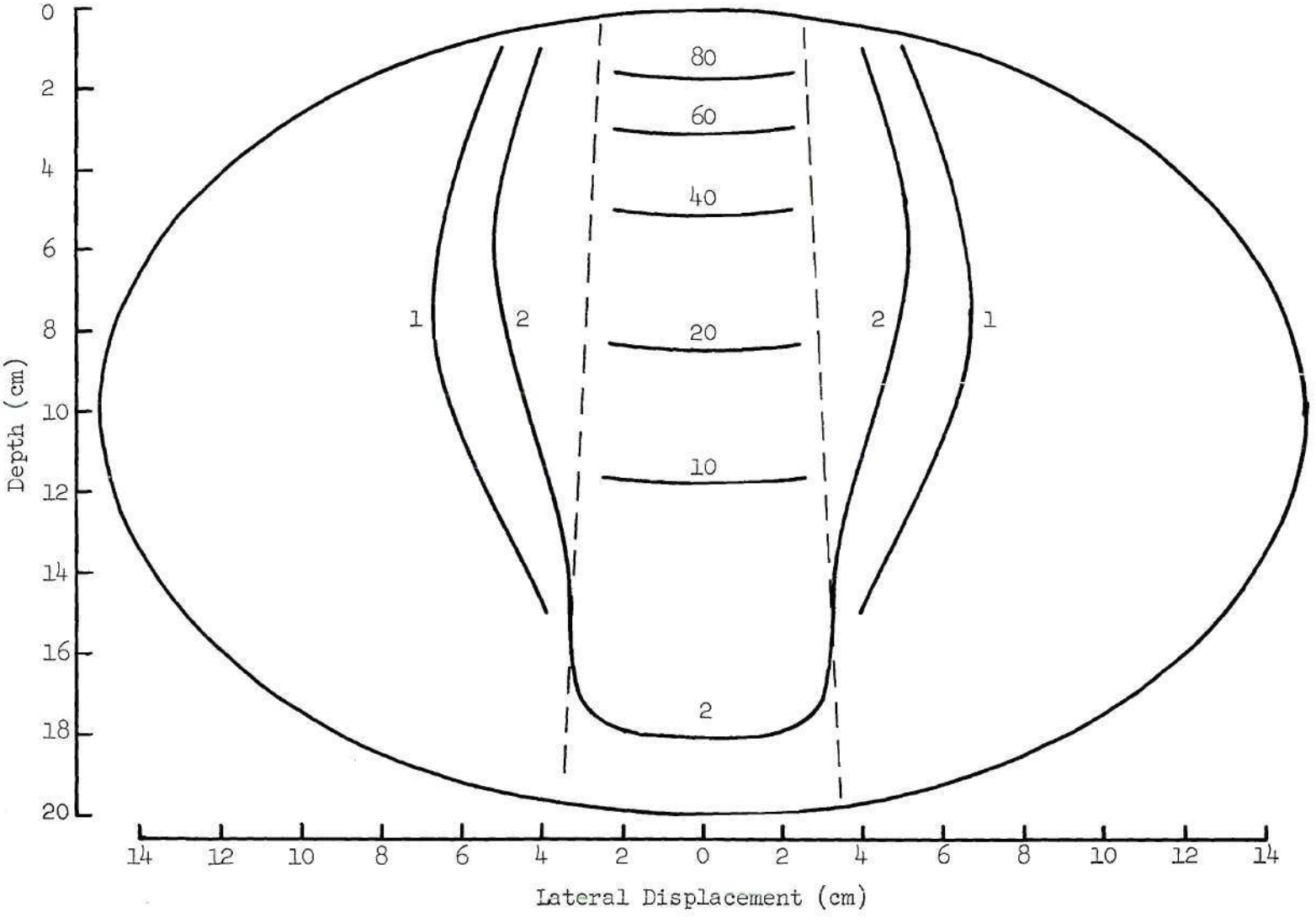

Figure 28. Isodose Contours for ^{252}Cf Neutrons for 50-cm Source-to-Skin Distance and 5.0-cm Field Diameter

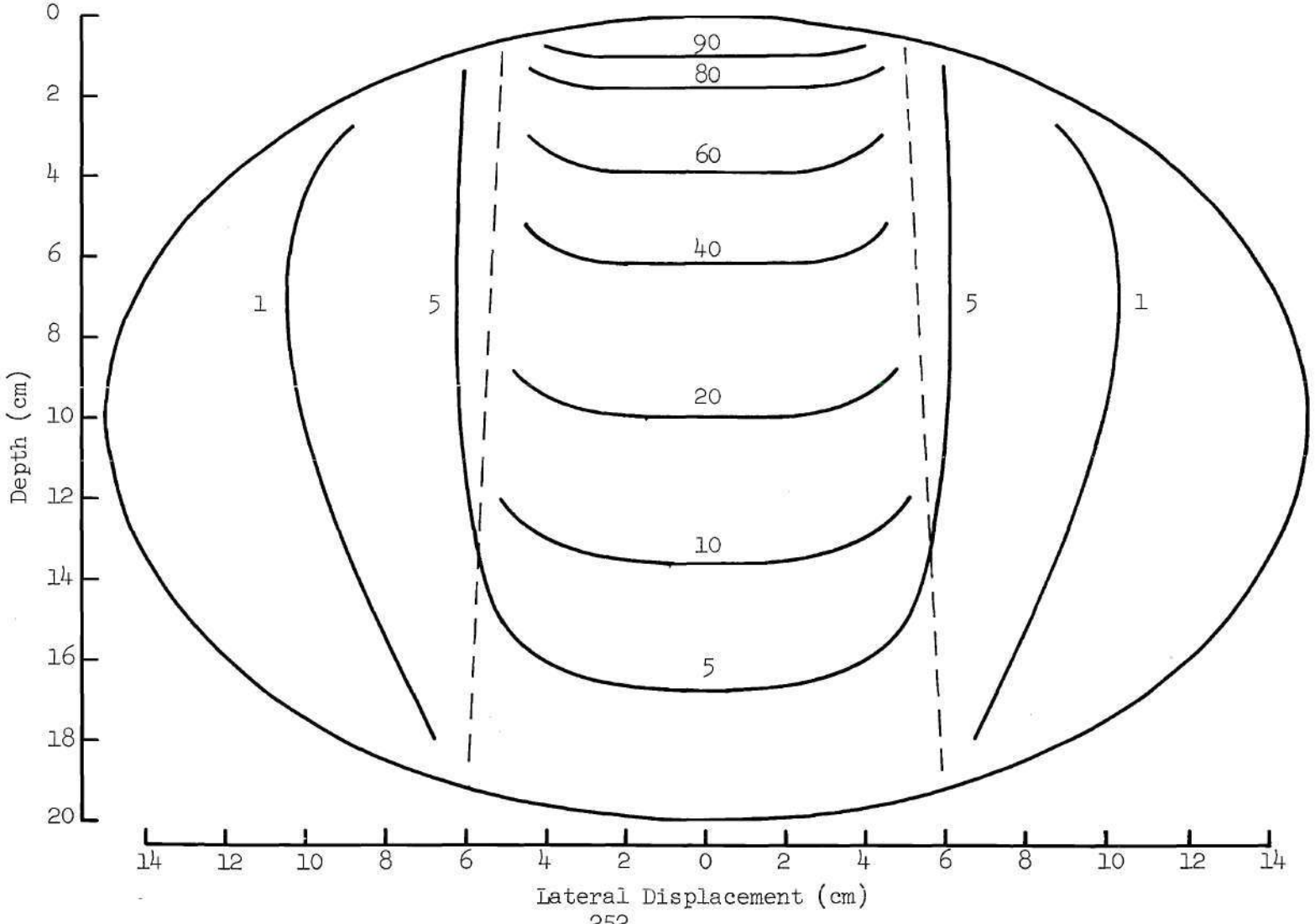

Figure 29. Isodose Contours for ^{252}Cf Neutrons for 100-cm Source-to-Skin Distance and 10-cm Field Diameter

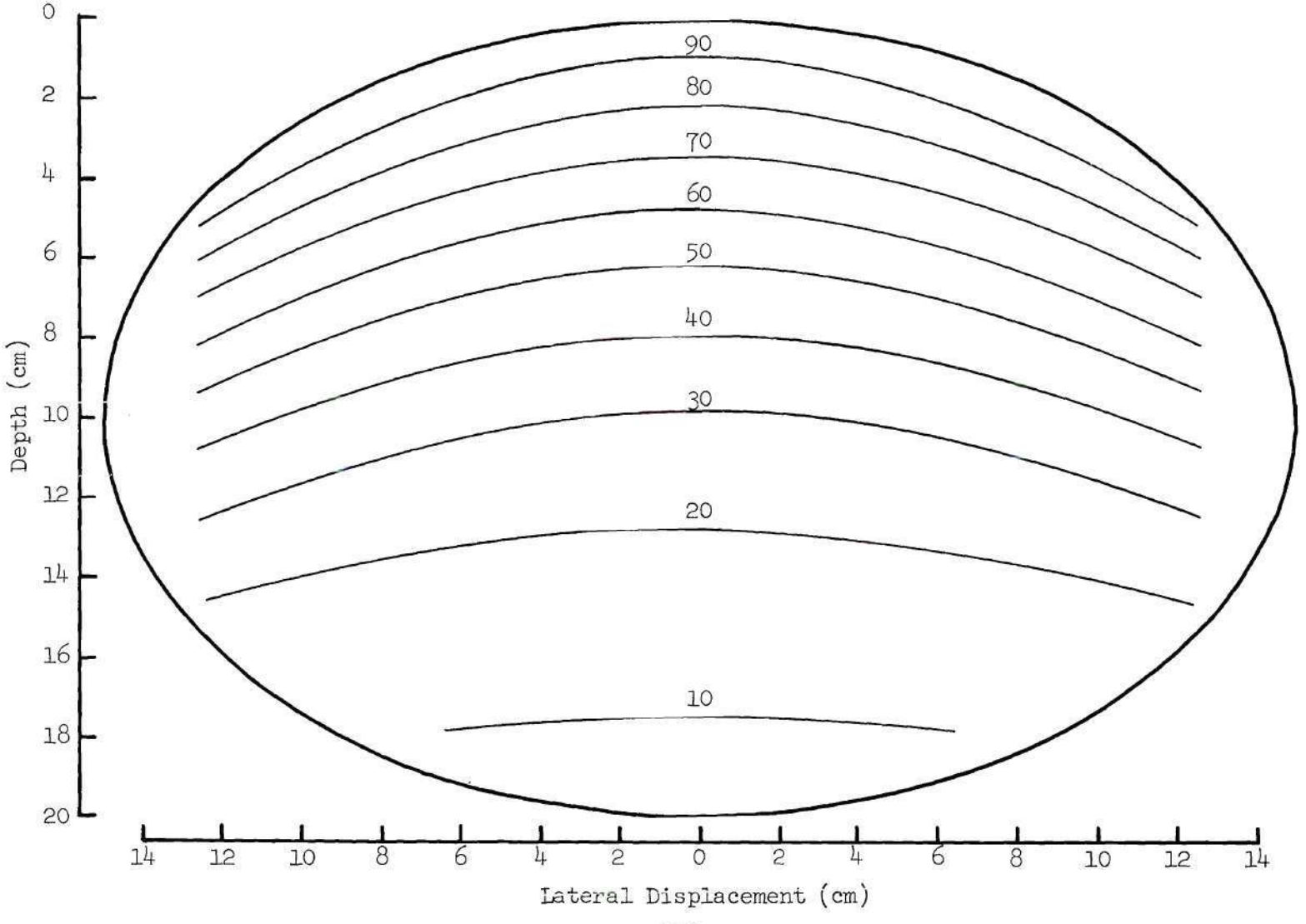

Figure 30. Isodose Contours for ^{252}Cf Neutrons for Broad-Beam Geometry

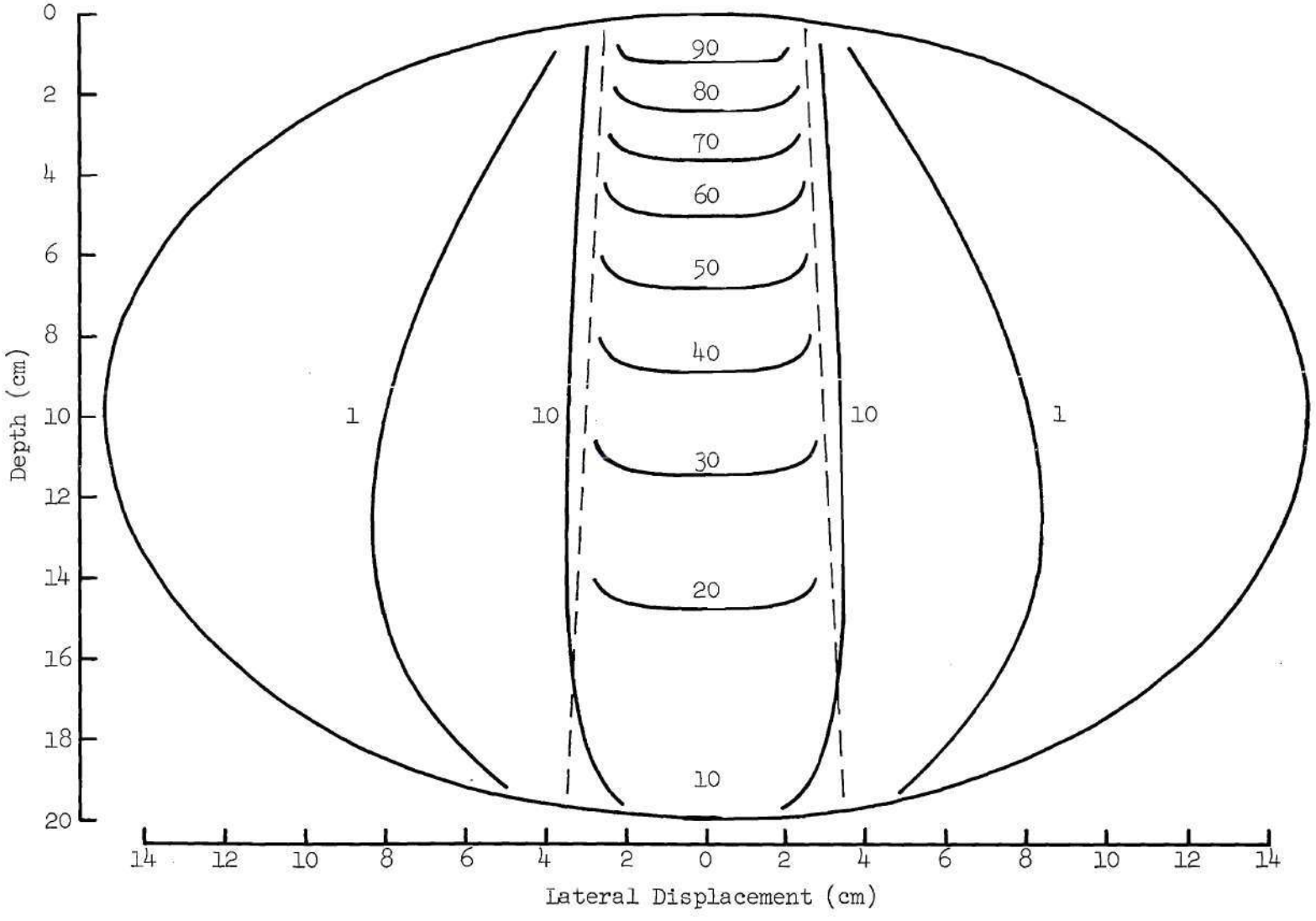

Figure 31. Isodose Contours for 14-MeV Neutrons for 50-cm Source-to-Skin Distance and 5.0-cm Field Diameter

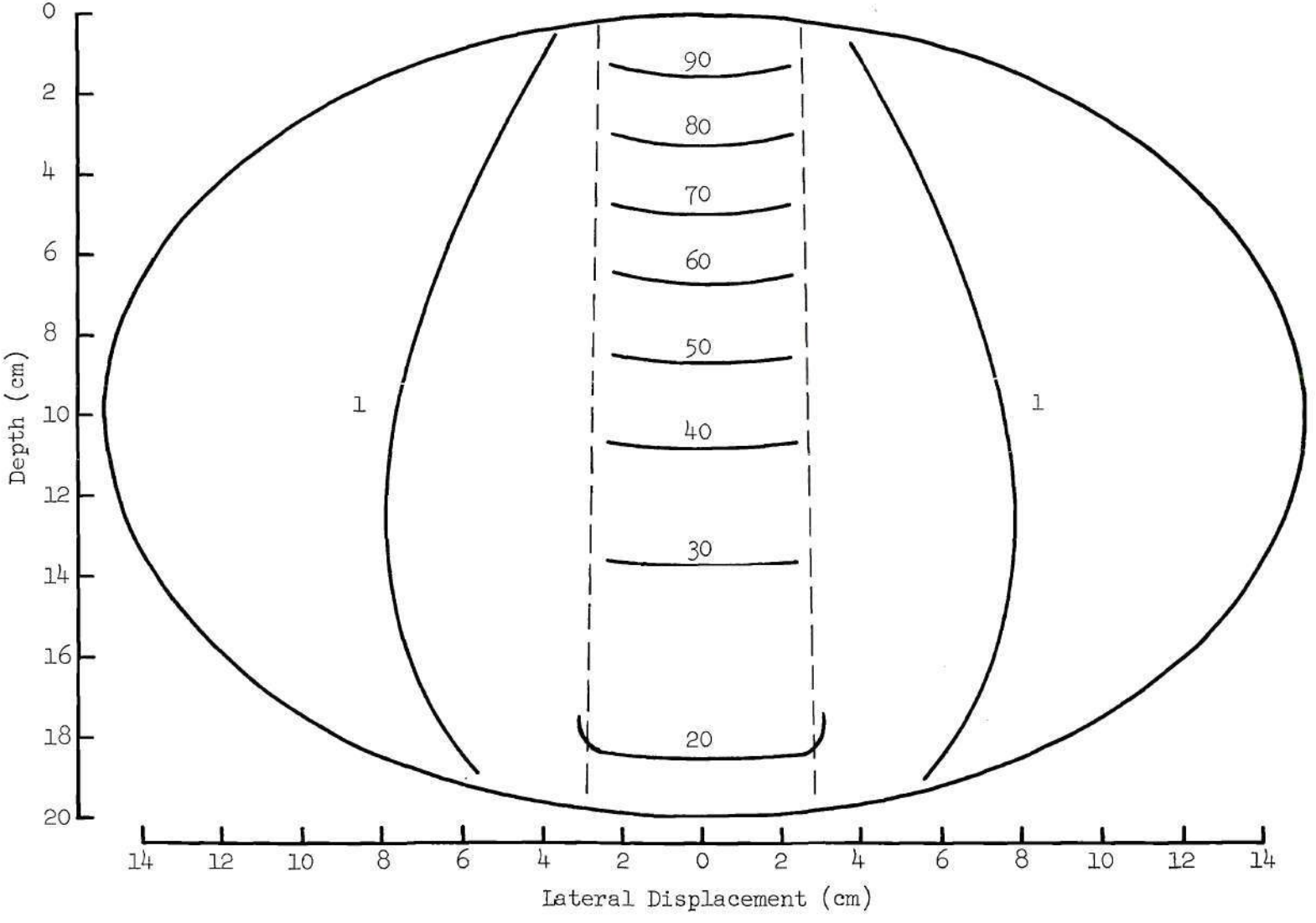

Figure 32. Isodose Contours for 14-MeV Neutrons for 125-cm Source-to-Skin Distance and 5.0-cm Field Diameter

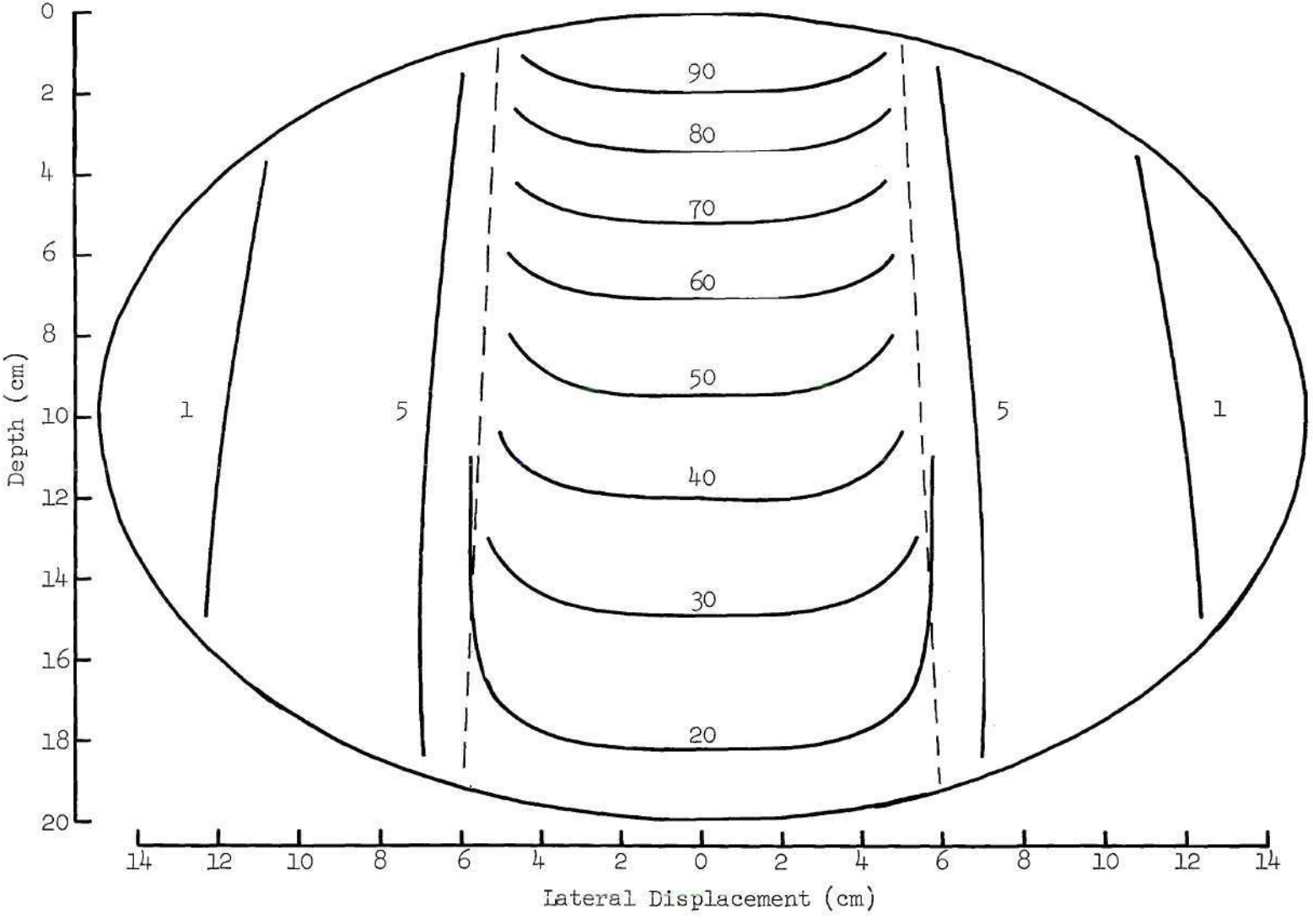

Figure 33. Isodose Contours for 14-MeV Neutrons for 100-cm Source-to-Skin Distance and 10-cm Field Diameter

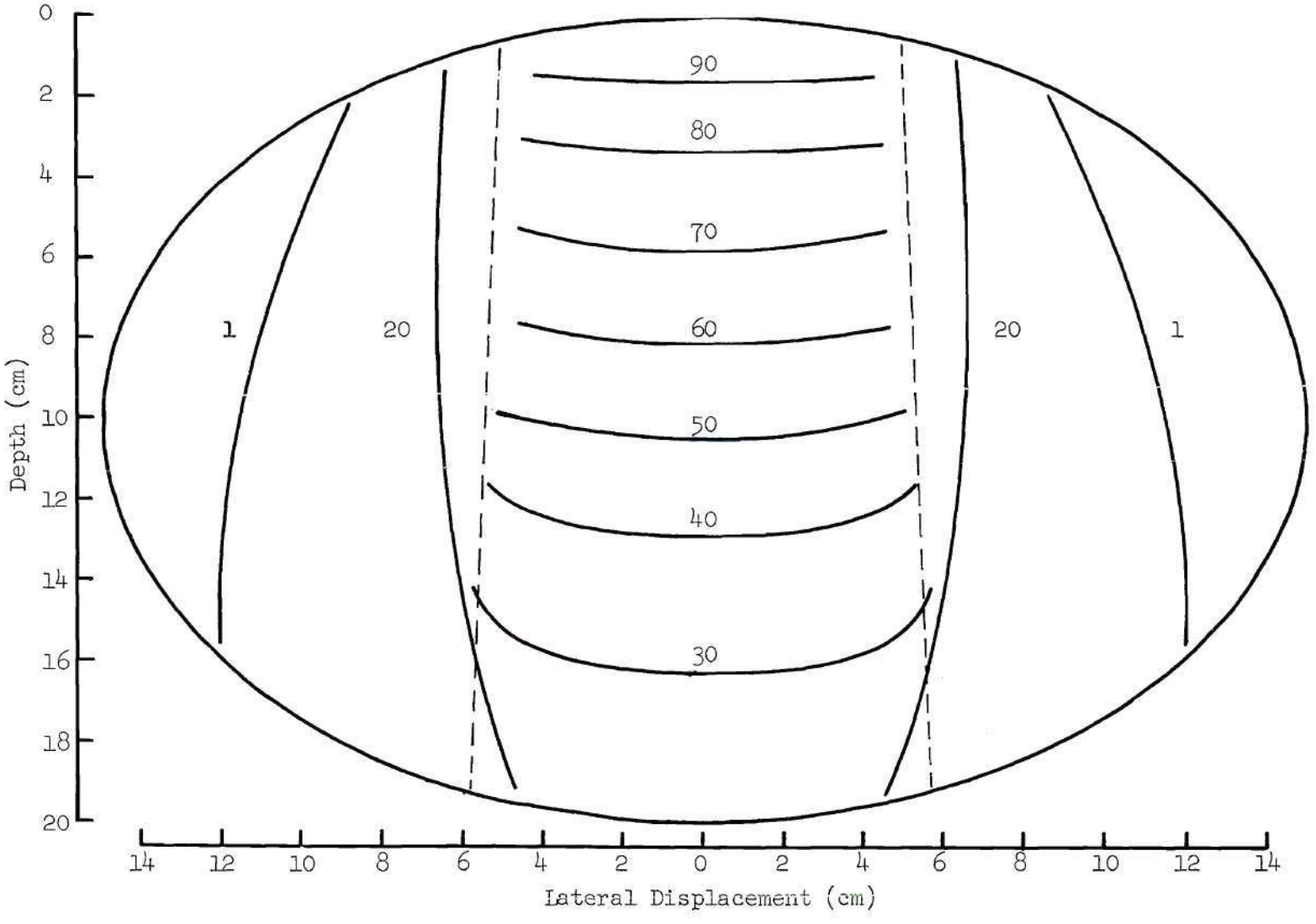

Figure 34. Isodose Contours for 14-MeV Neutrons for 125-cm Source-to-Skin Distance and 10-cm Field Diameter

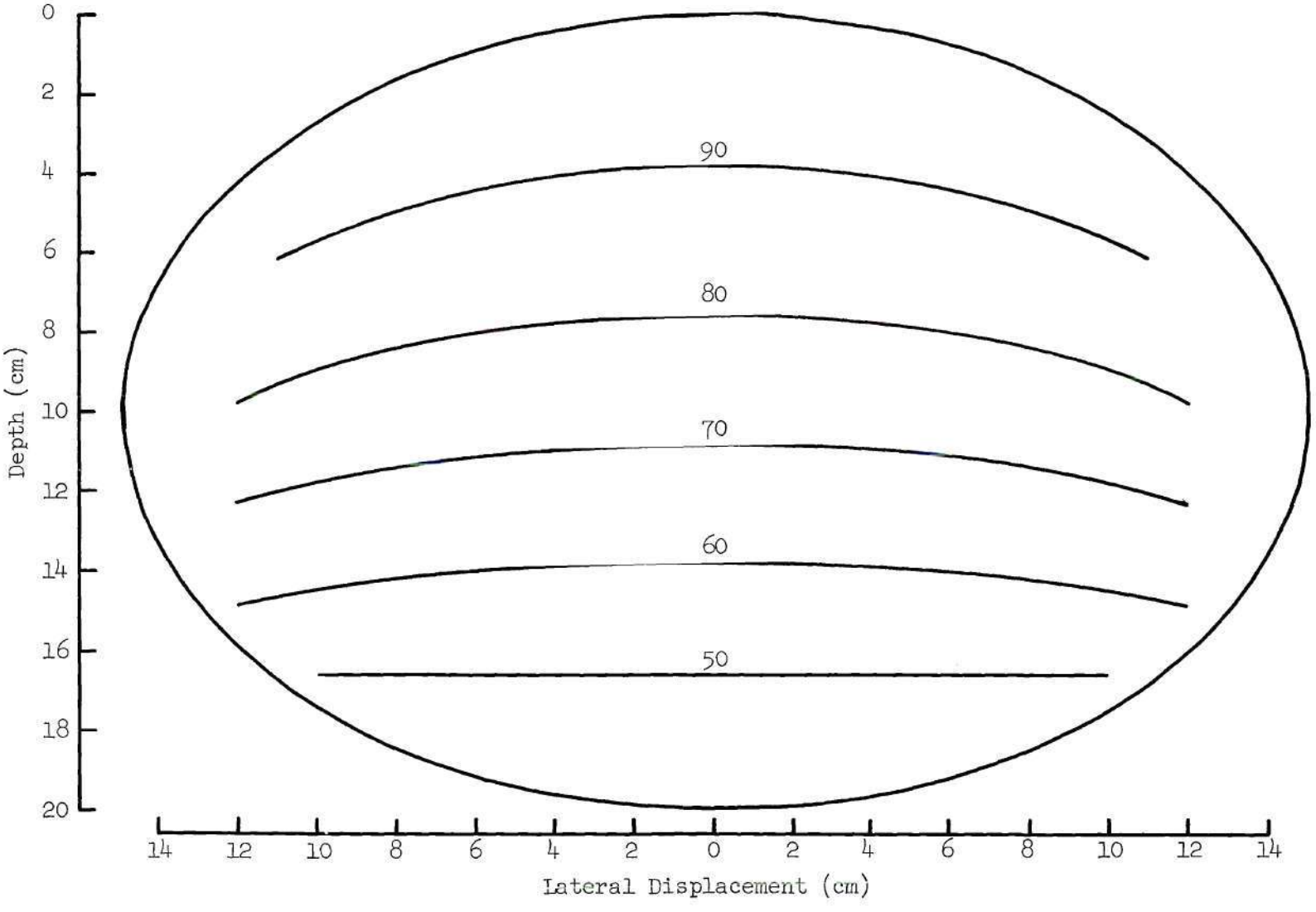

Figure 35. Isodose Contours for 14-MeV Neutrons for Broad-Beam Geometry

The basic mechanisms of energy loss are of importance if the dosimetry is to be related to biological damage. The types of interactions and their relative frequency and dosimetric significance are shown in Table 7. It is evident that, although hydrogen accounts for only 10 percent of the mass of most biological tissues, neutron interactions with hydrogen are more probable than any other interaction. As a consequence, most biological damage will be caused by recoil protons. Oxygen recoils account for about 25 percent of the dose for 14-MeV neutrons. These results were calculated for a 20-cm thick slab of standard man tissue.

Heterogeneous Tissue

Broad-beam isodose analyses were made for a human chest phantom containing muscle, heart, bone, and lung tissues with the geometry determined from a realistic model [85]. Histories for 130,000 ^{252}Cf neutrons and histories for 140,000 14-MeV neutrons were calculated. The average dose was computed for each type of tissue in the several regions, and these results are presented in Table 8. No values are shown for muscle because the dose ranged from maximum at the front surface to minimum at portions of the exit surface, and an average would be of little interest. This information is presented in Figures 36 and 37, which show the isodose contours in the heterogeneous phantoms. Note the asymmetry caused by the heart tissue in the presence of the less-dense lung tissue.

The significance of these calculations is that they illustrate the need for accurate adjustments of the treatment plans for fast-neutron therapy when the beams are to penetrate low-density tissue or

Table 7. Neutron Energy Loss in Standard Man Tissue

	Total (%)	H	C	N	O	
Atomic Composition	100	63.3	9.5	1.3	25.8	
14 MeV Interactions (%)						
Elastic	95	72	6	0.9	17	
Inelastic	5	--	0.8	0.2	4	
Energy Loss (%)						Avg.
Elastic	72	68	1	0.1	3	1.3
Inelastic	28	--	4	1	22	10.1
^{252}Cf Interactions (%)						
Elastic	99.9	81	5	0.8	14	
Inelastic	0.1	--	0.03	0.006	0.002	
Energy Loss (%)						Avg.
Elastic	98	90	3	0.3	6	0.24
Inelastic	2	--	0.6	0.2	0.8	6.9

Table 8. Average Doses in Heterogeneous Tissues

Tissue Description	Californium-252		14-MeV	
	Avg. % Max.	Std. Dev.	Avg. % Max.	Std. Dev.
Heart	56	± 0.8	81	± 2.0
Left Lung	45	± 1.1	74	± 2.5
Right Lung	57	± 1.6	82	± 2.3
Sternum	61	± 1.8	62	± 2.0
Vertebra	12	± 0.8	31	± 1.3
Spinal Cord	15	± 1.3	46	± 3.4
Left Ribs	26	± 1.8	41	± 2.2
Right Ribs	25	± 0.8	41	± 2.0

Note: Maximum Doses: ^{252}Cf. . . . 3.8×10^{-9} rads/neutron-cm^{-2}

14-MeV . . . 6.0×10^{-9} rads/neutron-cm^{-2}

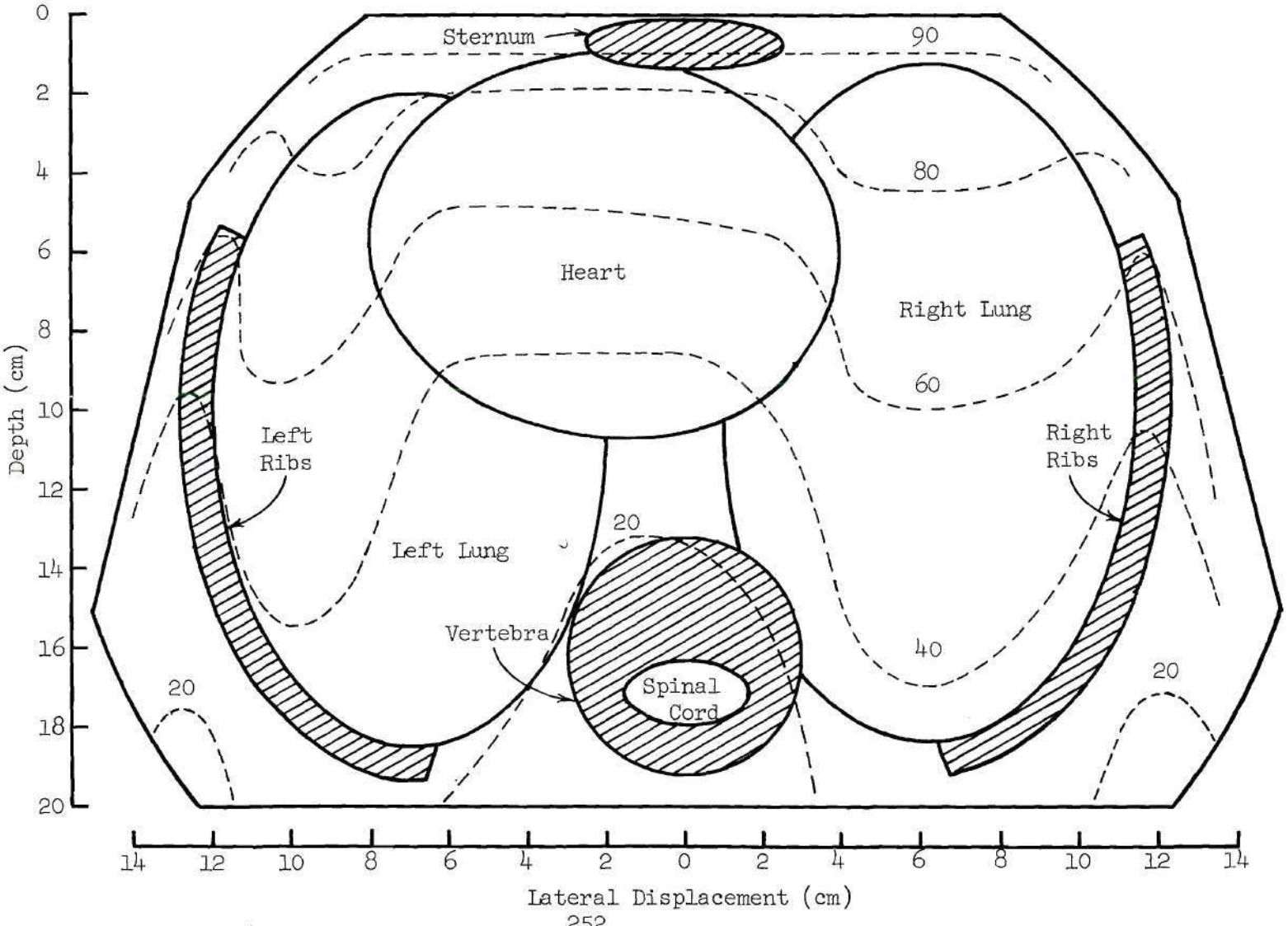

Figure 36. Isodose Contours for ^{252}Cf Neutrons for Broad-Beam Geometry in a Heterogeneous Phantom

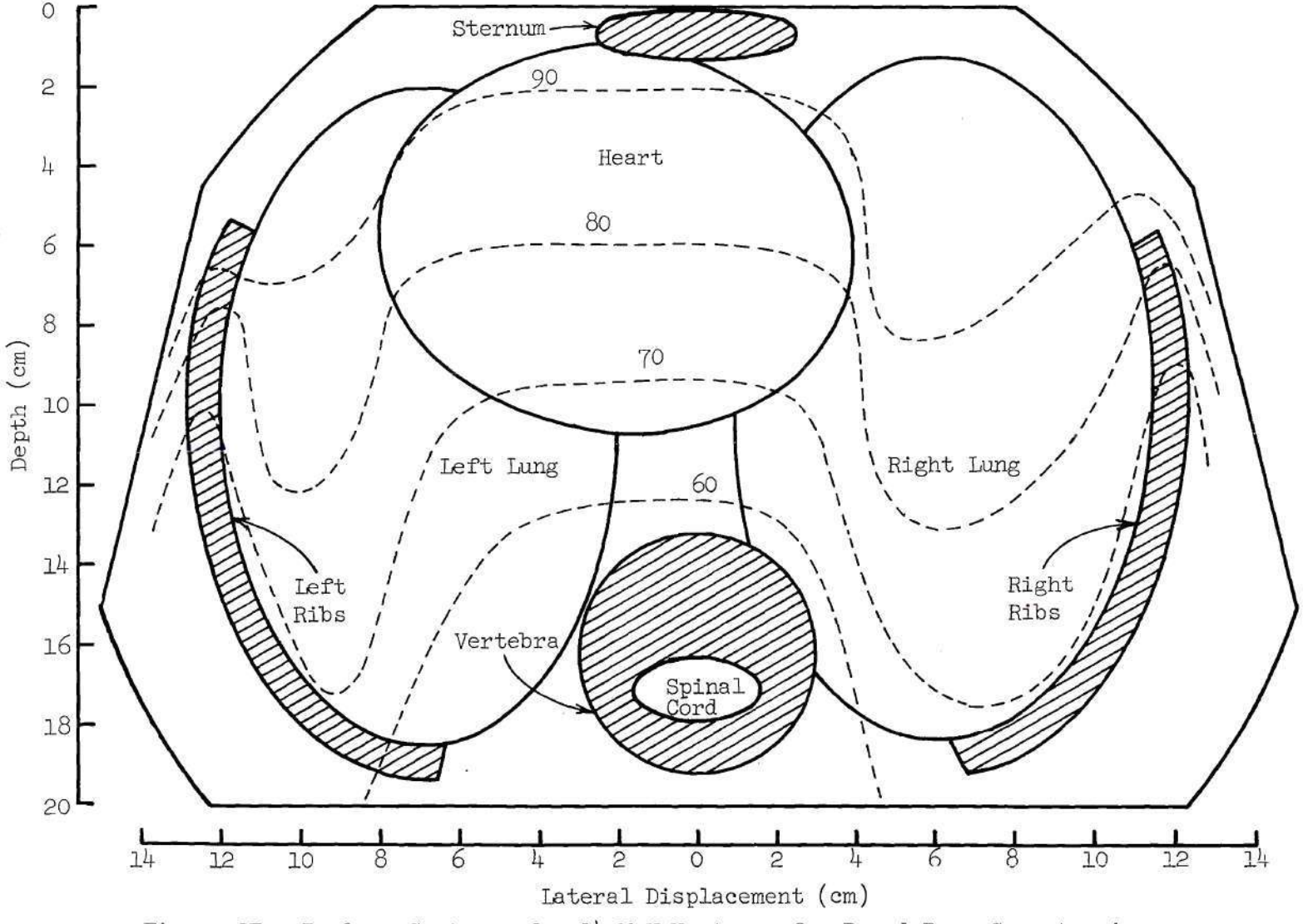

Figure 37. Isodose Contours for 14-MeV Neutrons for Broad-Beam Geometry in a Heterogeneous Phantom

air. Figure 38 shows the difference in the depth dose for homogeneous elliptical phantoms and the heterogeneous model where the path in the heterogeneous model is parallel to the centerline but displaced to the right by 6.0 cm thus penetrating the right lung.

Dose Limitations

The doses that would be required for radiography will depend on the type of source, the thickness of tissue, the attenuation properties of the inclusions of interest and the surrounding tissue, and the acceptable radiographic quality. Estimates of the doses that might be required can be made from considerations of the number of events of equal importance that must be detected per unit area in order to distinguish this area from an adjacent area of equal size. It can be shown [30] that under low contrast conditions the relation between the number of detections N_d and the contrast C is

$$N_d = \frac{k^2}{2C^2} \tag{5.11}$$

k may be interpreted as the threshold signal-to-noise ratio of a human eye [52] having a value between 2.0 to 5.0 depending on the type of imaging system. Clinically useful information can be attained if the resolution element in the image is one or two mm [89]. For example, if a scintillation-type imaging device is employed that has an inherent resolution of 1.0 mm and a k^2 of 20, then the surface dose in rads for 14-MeV neutrons may be estimated from

$$D = \frac{7.0 \times 10^{-6} \ (SSD + X)^2 \ \exp(-X/10)}{\varepsilon \ C^2 \ (SSD)^2} \tag{5.12}$$

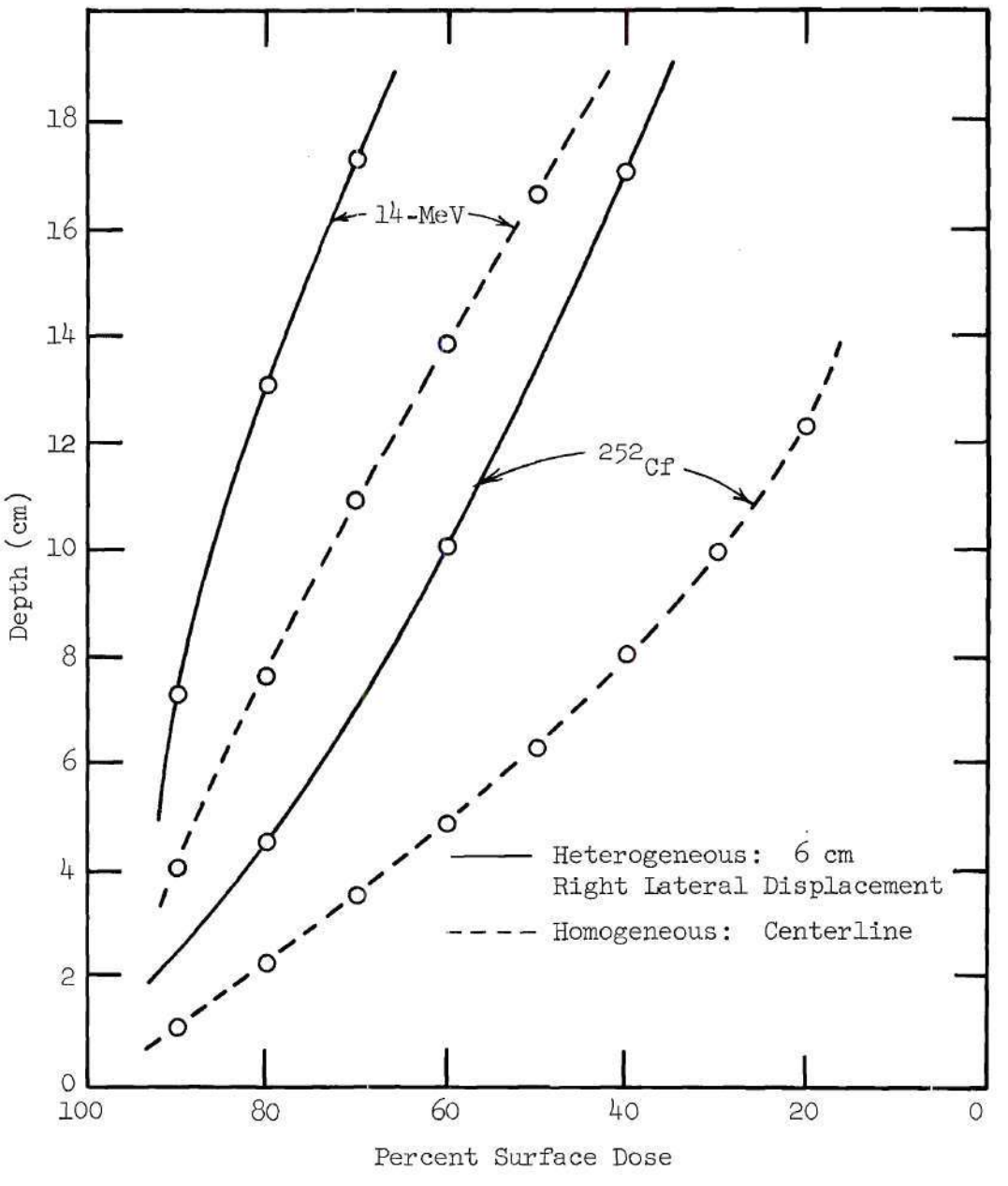

Figure 38. Depth Dose in Homogeneous and Heterogeneous Tissue

where ϵ is the detector efficiency, C is the object contrast, X is the overall tissue thickness, and SSD is the source-to-surface distance. Equation 5.12 is based on the assumption of 7.0×10^{-9} rads per unit fluence.

Figure 39 shows calculations of the dose as a function of tissue thickness for unilateral radiography with detector efficiencies of $\epsilon = 0.1$ or 0.01 and for object contrasts of $C = 0.1$ or 0.01. These doses must be considered as minimum estimates if C is the object contrast because the image contrast will be smaller than the object contrast. Geometric reduction in the fluence must always be included in calculations for particular systems as an increase in the dose by the factor $(SSD + X)^2/SSD^2$. Similar dose estimates for ^{252}Cf radiography have been reported by Parks [30]. Dosimetry will probably not be a severely limiting factor for biological radiography for either type of source.

A more limiting restriction will probably be the source intensity. In order to minimize motion unsharpness in the radiography of living subjects, the duration of the exposure must be limited to a few seconds, particularly for chest radiographs. Equation 5.13 gives the required source intensity S in neutrons per second

$$S = 10^9 \ (SSD)^2 \ bD/t \qquad (5.13)$$

where b is a constant equal to 3.1 for ^{252}Cf neutrons or $b = 1.8$ for 14-MeV neutrons, D is the dose in rads that must be delivered to the surface of the tissue to obtain an adequate radiograph, and t is the exposure time in seconds. If the radiograph requires 10 rads at 100 cm SSD and t is limited to 10 seconds, then a source intensity of $10^{13} \times b$

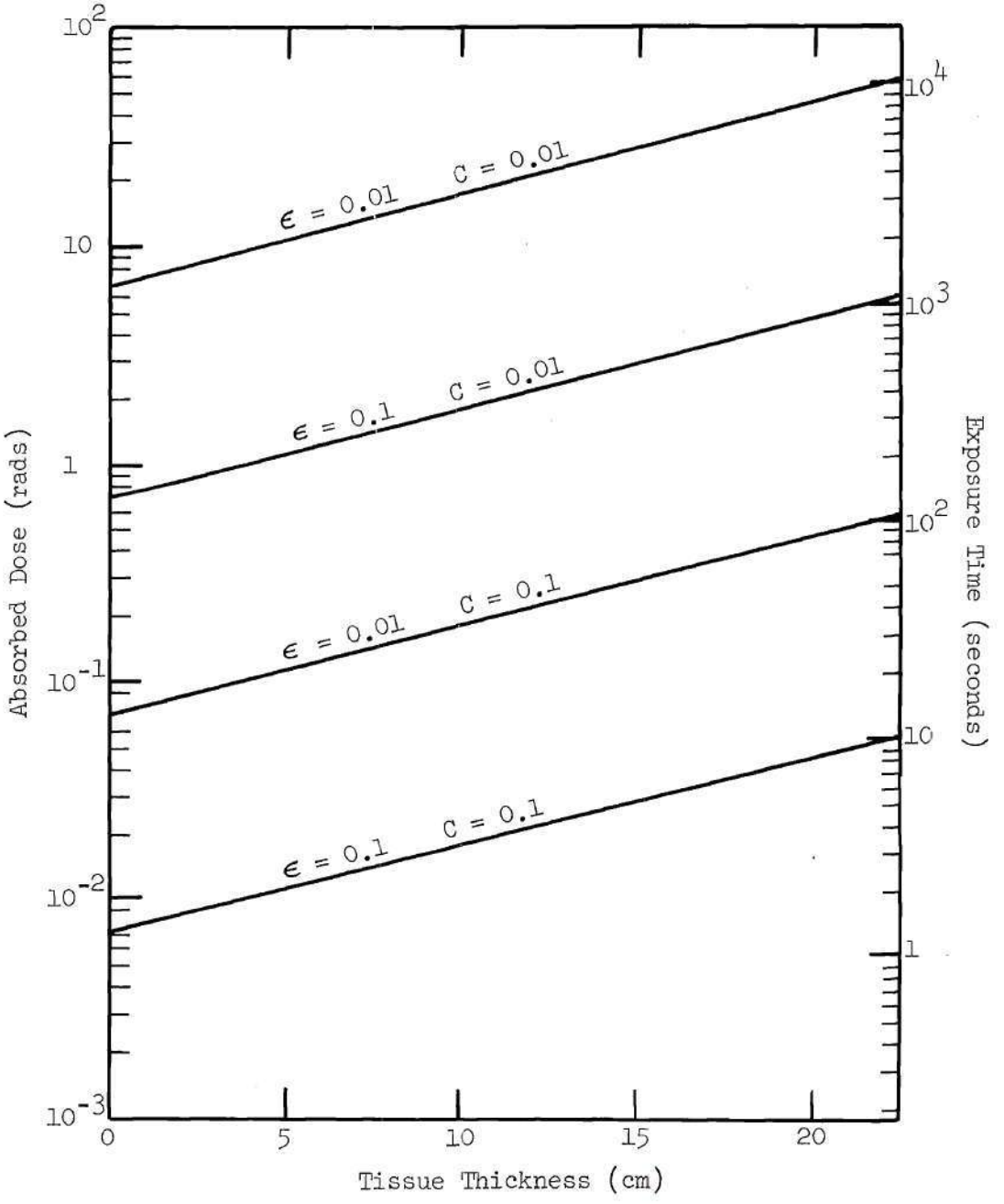

Figure 39. Dose Estimates for Unilateral Radiography with 14-MeV Neutrons

would be required. This intensity could not be met with the presently available sources. As an illustration, for a 14-MeV source of 10^{11} n/sec intensity at an SSD of 100 cm, the exposure time required for radiographs with the system described in the preceding paragraph is plotted as the ordinate on the right of Figure 37. Source intensity is also a limiting factor for neutron therapy [31] where the minimum intensity required is about 5×10^{12} n/sec.

CHAPTER VI

CONCLUSIONS AND RECOMMENDATIONS

Conclusions

The purpose of this research was: 1) to examine the image-forming quality that could be achieved with fast-neutron radiography of biological objects and 2) to examine the dosimetric properties of external fast-neutron beams.

It is concluded that the most suitable neutron sources are the fission of californium-252 and 14-MeV neutrons from the D-T reaction in an accelerator. Fast-neutron radiography may be practically applied to the examination of thick biological tissues containing air inclusions overlaid with bone. The bone will cause little interference in ^{252}Cf radiography, but the attenuation in tissue is a limiting factor for this source. Bone will have a positive contrast in muscle for 14-MeV neutrons, but the bone interference will be less than for radiography with photons at energies below 2.0 MeV.

For the radiography of living objects, the imaging system could be a scintillation type having a detection efficiency in the order of approximately 10 to 20 percent.

It is further concluded that the detection of neutrons that have been scattered in the object will cause little change in the overall resolution of the system, but these scattered neutrons will severely affect the clarity with which the images are formed. This effect will

be most significant for ^{252}Cf neutrons and thick objects. This conclusion is in disagreement with the interpretation of the source of image degradation in fast-neutron radiographs reported in the literature. Other authors have assumed that the poor image quality that has been observed in experimental radiographs is due to the decreased resolution of the system. Due to forward scattering of fast neutrons, little if any improvement in image quality can be expected from the separation of the imaging device from the back surface of the object.

It is concluded that the techniques that have been developed and applied in this research for the theoretical examination of image-forming quality are accurate and informative. These techniques can be applied more generally to the broader applications of fast-neutron radiography such as the examination of non-biological media.

Dosimetry considerations will be important, particularly if wide fields and R.B.E. values of 2.0 or greater are required. However, with the development of an efficient imaging system, the maximum doses can be kept below a few rads for most useful applications. Calculations of the depth-dose patterns in homogeneous tissue for narrow-beam geometries are in agreement with experimental measurements. It is concluded that the mathematical techniques that have been employed for the dosimetry calculations are useful and accurate. It should be pointed out that theoretical dose calculations using these techniques can be applied effectively to specific geometries that are anticipated for neutron therapy. However, it is important to note that the dose patterns in heterogeneous tissues indicate that depth dose based on the homogeneous approximation can be in serious error.

Recommendations

It is recommended that the emphasis in fast-neutron radiography research for biological applications be shifted to the development of efficient and accurate imaging devices. In particular, the need is seen for the development of electronic background suppression which can be used in conjunction with scintillation detection and a storage-type imaging system.

A series of experimental transmission studies should be initiated to clarify bone composition and the neutron penetration of bone.

Theoretical dosimetry calculations should be made for heterogeneous phantoms for the particular situations for which neutron therapy is thought to be potentially useful. The results of Monte Carlo calculations for dosimetry can be very useful, but the calculations themselves cannot be made routinely. Therefore, an investigation should be initiated to develop approximate calculations, possibly based on an empirical model, that could be used to estimate dose patterns without the need for difficult and/or inaccurate experimental measurements or large numbers of complicated computer calculations. The techniques developed in this research would be particularly useful in testing these empirical models.

It is finally recommended that a program be initiated to examine the image-forming quality of thermal-neutron radiography systems. The approach should involve both theoretical calculations, similar to those employed in this research, and experimental measurements of modulation transfer functions. With suitable modifications of the computer codes developed during this research, thermal-neutron dosimetry calculations also could be made.

APPENDICES

APPENDIX A

DESCRIPTION OF BIOLOGICAL MEDIA

Two types of phantoms are used in this research: 1) homogeneous phantoms containing only standard man composition tissue, and 2) heterogeneous phantoms containing muscle, lung, and bone tissues. Table 9 gives the composition of these tissues. Figure 40 shows the relative importance of each element for neutron interactions in terms of the macroscopic total cross sections times the relative abundance in bone tissue assumed to be 50 percent cortex and 50 percent marrow as a function of neutron energy. The figures for lung tissue and muscle tissue are not included because the relative fractions of H, C, N, and O are nearly the same as for standard man tissue. The values for lung may be obtained from Figure 41 for standard man tissue by multiplying each point by the average density of 0.32 gm/cm^3. Figures 42, 43, and 44 are further reductions of the data for standard man tissue to illustrate the shape and relative importance of elastic, nonelastic, and inelastic interactions. Nonelastic interactions are defined as any type of neutron interaction except elastic scattering. All of these data are taken from the 05R cross section library [90].

Table 9. Atomic Compositions of Biological Tissues

Tissue	Density	Element Percent by Weight					
	g/cm^3	H	C	N	O	P	Ca
Standard-Man[a]	1.0	10.0	18.0	3.0	65.0		
Muscle[b]	1.0	10.2	12.3	3.0	72.9		
Lung[c]	0.32	10.2	12.3	3.5	72.9		
Bone[d]	1.42	7.6	16.7	3.7	52.2	6.8	14.8

[a] NBS Handbook 63 [76]

[b] Johns [91]

[c] Ter-Pogossian [52]

[d] Brown [92] and Barton [93] (50 percent cortex, 50 percent marrow)

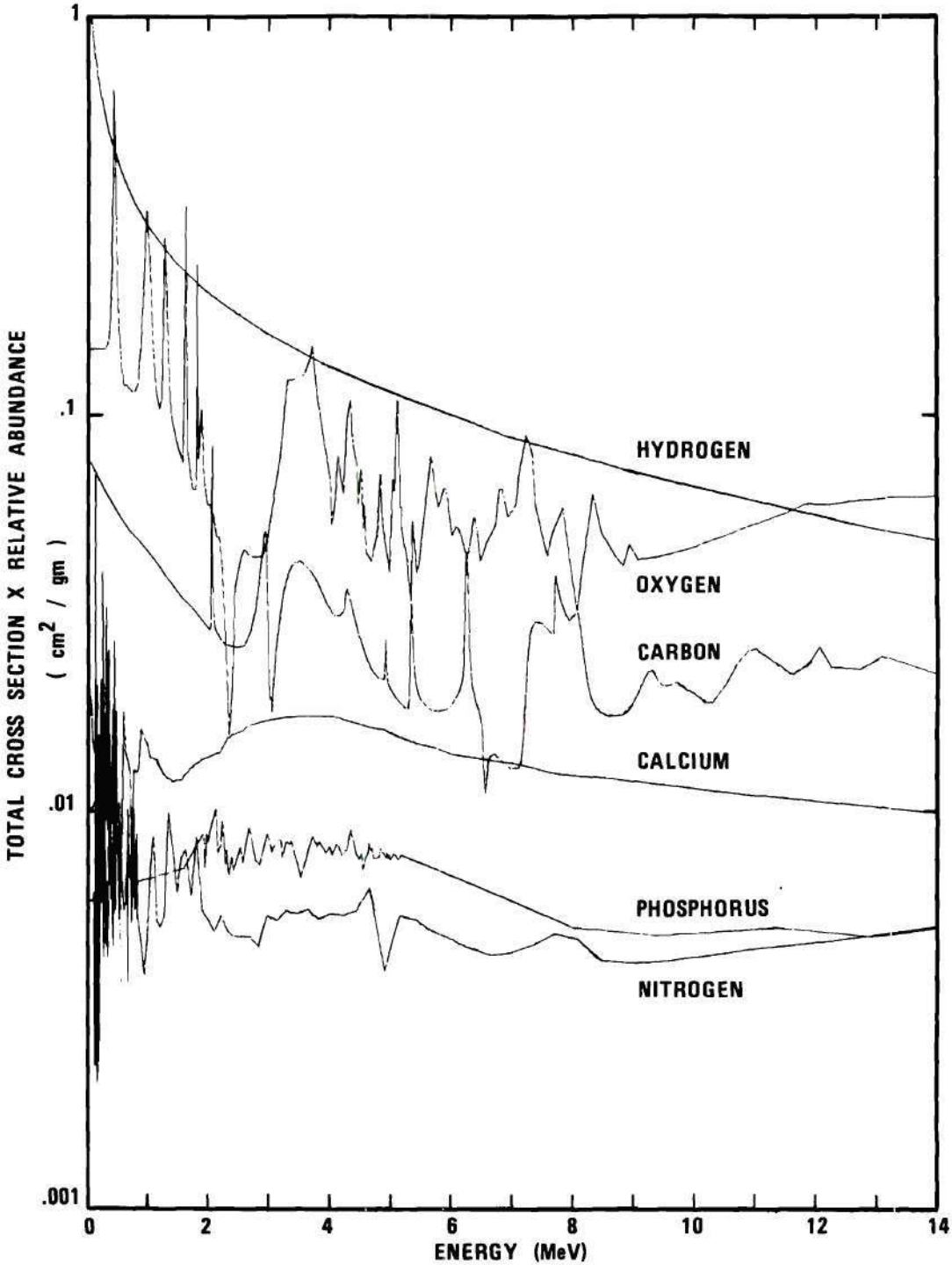

Figure 40. Probability of Neutron Interactions in Bone

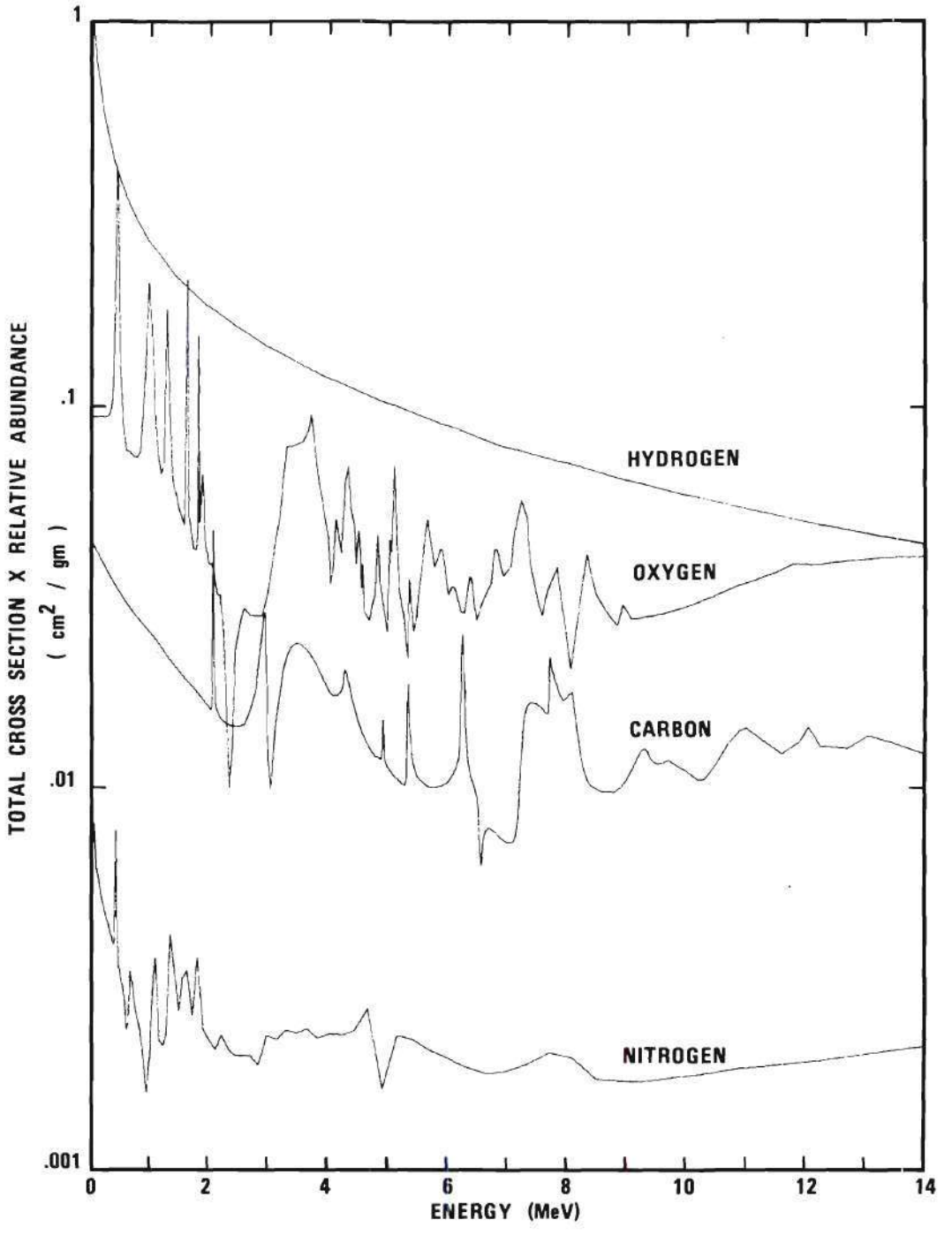

Figure 41. Probability of Neutron Interactions in Standard Man Tissue

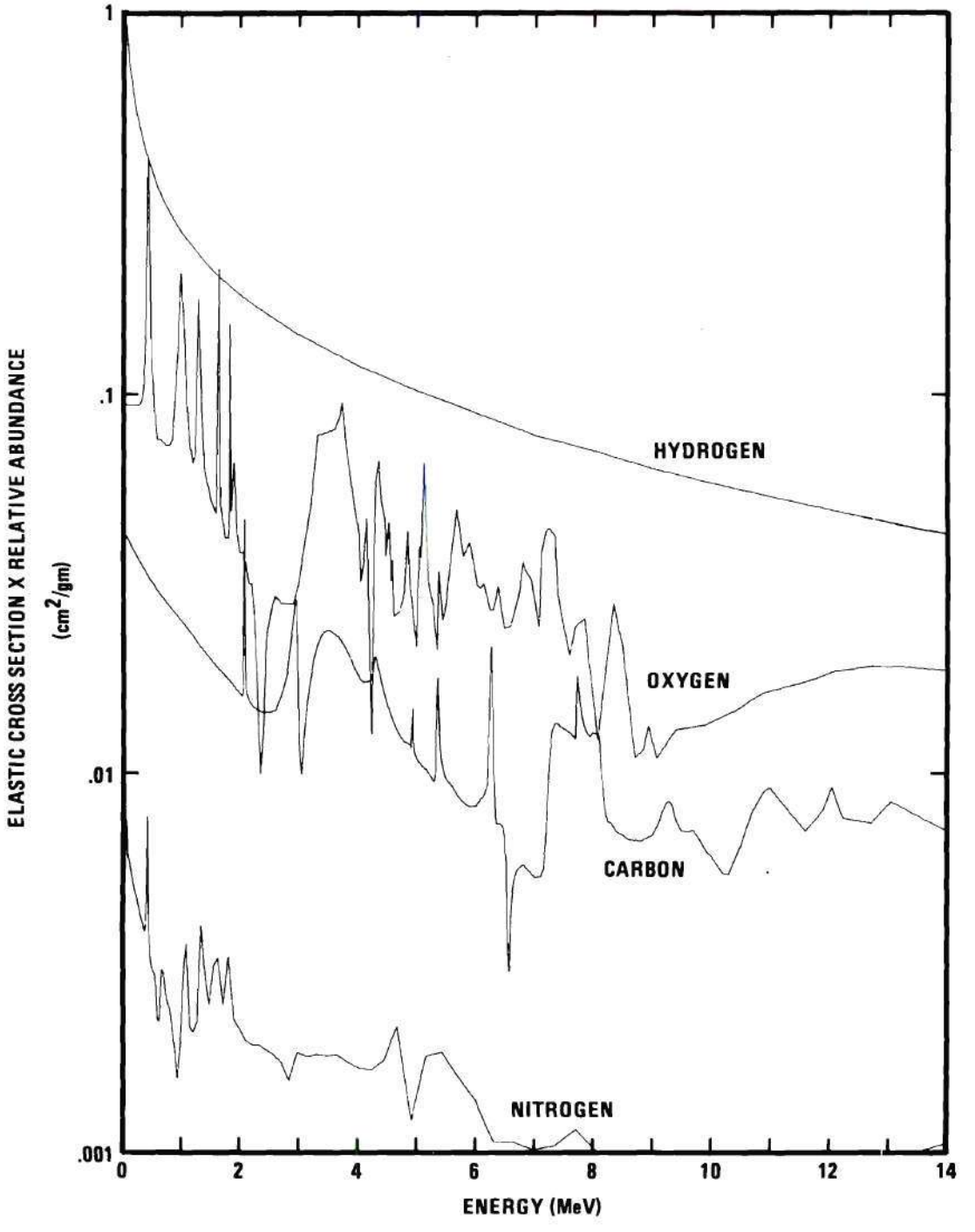

Figure 42. Probability of Elastic Neutron Interactions in Standard Man Tissue

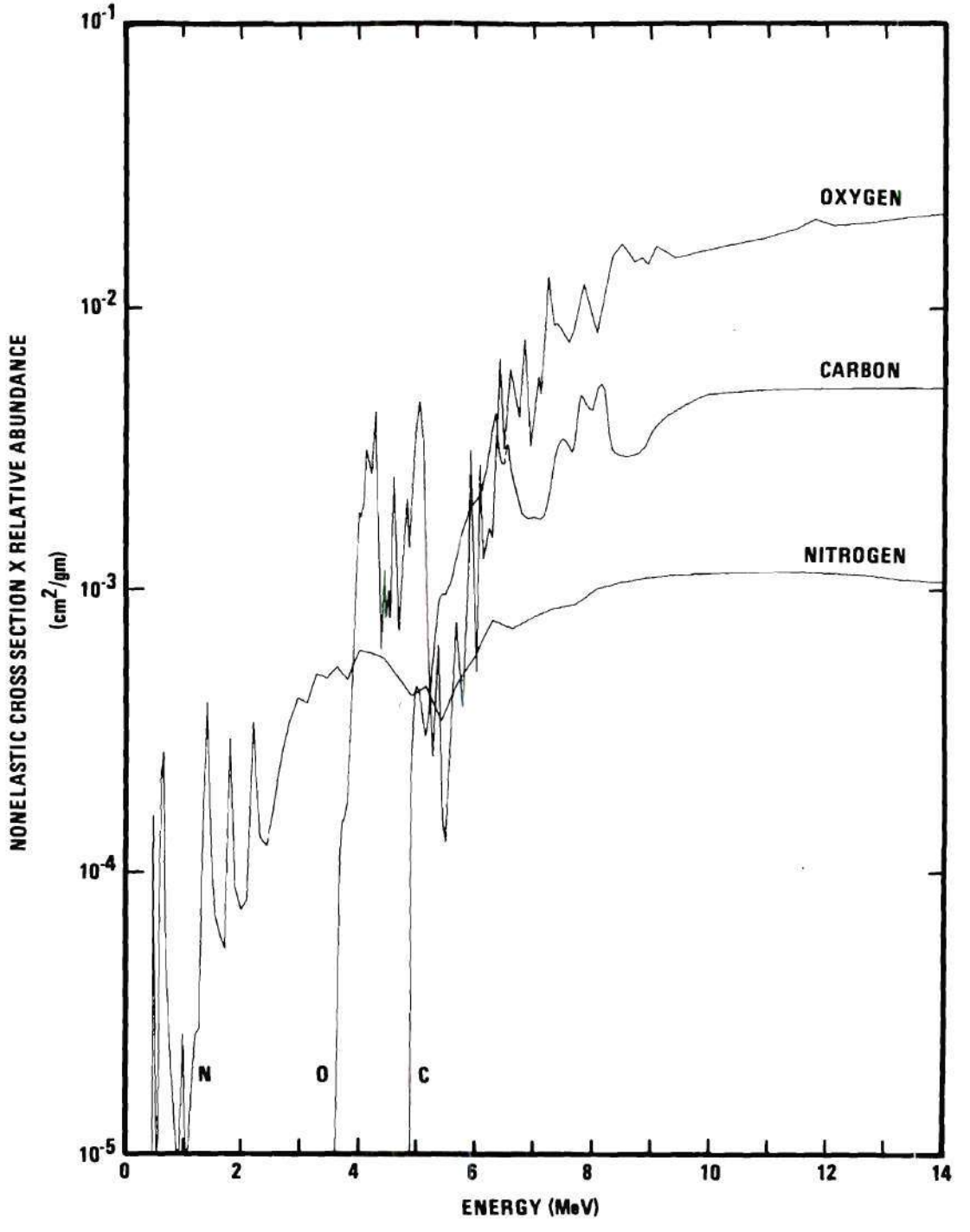

Figure 43. Probability of Nonelastic Neutron Interactions in Standard Man Tissue

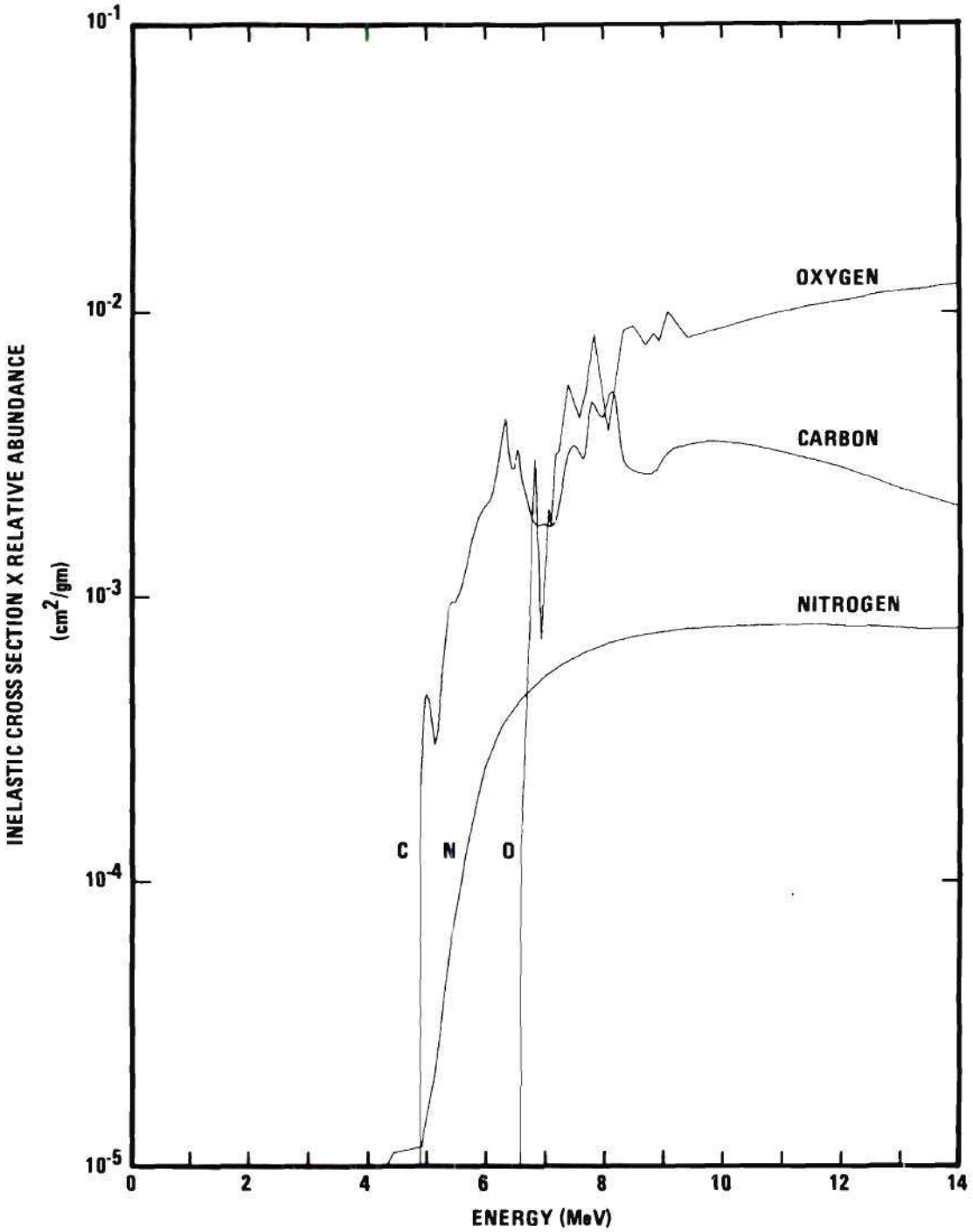

Figure 44. Probability of Inelastic Neutron Interactions in Standard Man Tissue

APPENDIX B

DERIVATION OF THE KINETIC ENERGY OF INELASTICALLY SCATTERED NEUTRONS

A complete description of elastic scattering is easily obtained from the application of the principles of conservation of energy and momentum, and the relations between the various parameters in the laboratory and center-of-mass reference systems are found in many texts. While the same conservation principles apply to inelastic scattering, the derivation of useful equations is complicated by the nonconservation of kinetic energy in the system. The following derivation is given for the convenience of other researchers.

Basic Equations and Notation for the Lab System

Before Collision

After Collision

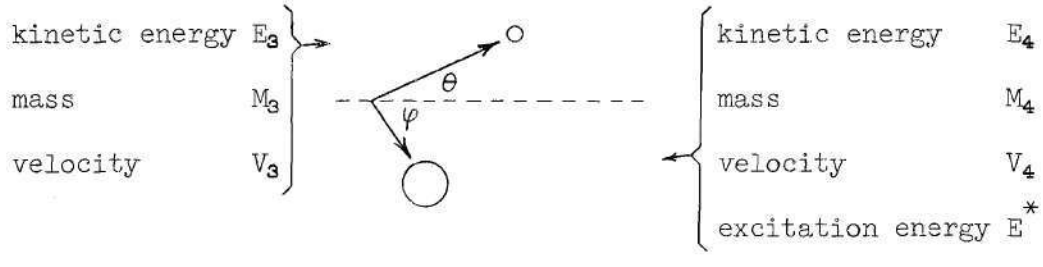

Energy Balance

$$E_1 = E_3 + E_4 + E^* \tag{1}$$

Momentum Balance

x-direction

$$\sqrt{2M_1E_1} = \sqrt{2M_3E_3}\cos\theta + \sqrt{2M_4E_4}\cos\varphi \tag{2}$$

y-direction

$$0 = \sqrt{2M_3E_3}\sin\theta - \sqrt{2M_4E_4}\sin\varphi \tag{3}$$

Basic Equations and Notation for the Center-of-Mass System

Before Collision

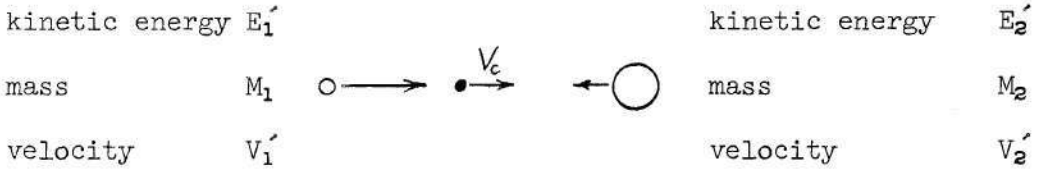

After Collision

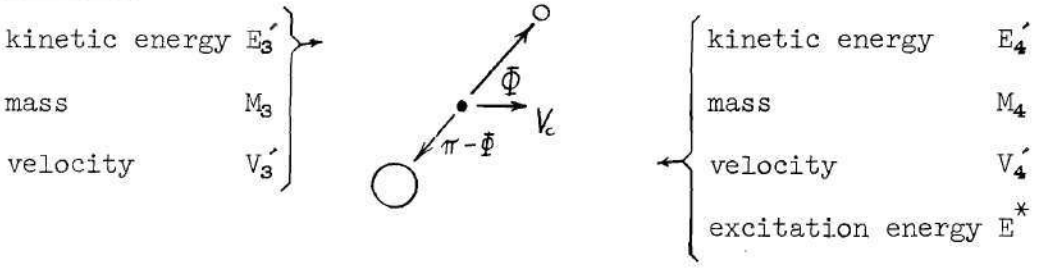

Energy Balance

$$E_1' + E_2' = E_3' + E_4' + E^* \tag{4}$$

Momentum Balance

$$\sqrt{2M_1E_1'} = \sqrt{2M_2E_2'} \tag{5}$$

$$\sqrt{2M_3E_3'} = \sqrt{2M_4E_4'} \tag{6}$$

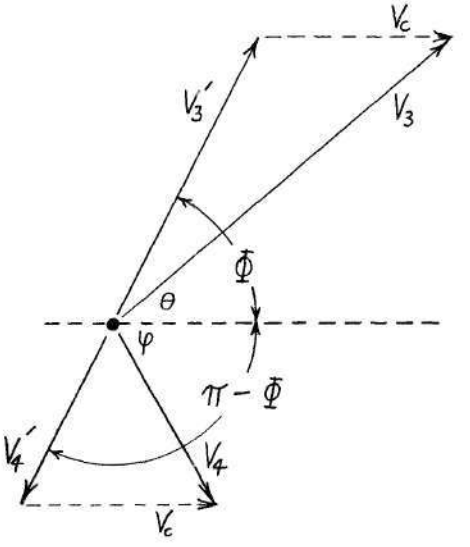

Figure 45. Relation Between the Laboratory and Center-of-Mass Systems (after collision)

Add Equations 2 and 3 after squaring:

$$2M_1E_1 + 2M_3E_3 - 4\sqrt{M_1E_1M_3E_3}\cos\theta = 2M_4E_4 \tag{7}$$

or

$$E_4 = \frac{E_1M_1}{M_4} + \frac{E_3M_3}{M_4} - \frac{2\sqrt{M_1E_1M_3E_3}\cos\theta}{M_4} \tag{8}$$

Substitute Equation 8 in Equation 1:

$$E_3 = E_1 - E^* - \frac{E_1M_1}{M_4} - \frac{E_3M_3}{M_4} + \frac{2\sqrt{M_1E_1M_3E_3}\cos\theta}{M_4} \tag{9}$$

From Figure 45

$$V_3\cos\theta = V_3'\cos\Phi + V_c \tag{10}$$

or

$$\sqrt{2M_3E_3}\cos\theta = \sqrt{2M_3E_3'}\cos\Phi + M_3V_C \tag{11}$$

Substitute Equation 11 for $\cos\theta$ into Equation 9

$$E_3\left(\frac{M_3+M_4}{M_4}\right) = E_1\left(\frac{M_4-M_1}{M_4}\right) - E^* + \frac{\sqrt{2M_1E_1}}{M_4}\left[\sqrt{2M_3E_3'}\cos\Phi + M_3V_C\right] \tag{12}$$

An expression for E_3' may be derived in terms of known parameters. Substitute E_4' from Equation 6 into Equation 4

$$E_3'\left(\frac{M_3+M_4}{M_4}\right) = E_1' + E_2' - E^* \tag{13}$$

But

$$E_1' + E_2' = \tfrac{1}{2}M_1(V_1-V_C)^2 + \tfrac{1}{2}M_2V_C^2$$

$$= \tfrac{1}{2}M_1V_1^2 + \tfrac{1}{2}V_C^2(M_1+M_2) - M_1V_1V_C \tag{14}$$

and because

$$V_C = \frac{M_1V_1}{(M_1+M_2)} = \frac{\sqrt{2M_1E_1}}{(M_1+M_2)}$$

it follows that

$$E_1' + E_2' = \frac{E_1M_2}{(M_1+M_2)} \tag{15}$$

Substitute Equation 15 into Equation 14

$$E_3' = \left(\frac{M_4}{M_3+M_4}\right)\left[\frac{E_1M_2}{(M_1+M_2)} - E^*\right] \tag{16}$$

Substitute Equation 16 into Equation 13

$$E_3\left(\frac{M_3+M_4}{M_4}\right) = E_1\left(\frac{M_4-M_1}{M_4}\right) - E^* +$$

$$\frac{2}{M_4}\left[\sqrt{\frac{M_3 M_4 M_1 E_1\,[\,E_1 M_2 - E^*(M_1+M_2)]}{(M_3+M_4)(M_1+M_2)}}\;\cos\Phi + \frac{M_3 M_1 E_1}{(M_1+M_2)}\right]$$

or

$$E_3 = E_1\left(\frac{M_4-M_1}{M_3+M_4}\right) - \frac{E^* M_4}{(M_3+M_4)} + \tag{17}$$

$$\frac{2}{(M_3+M_4)}\left[\sqrt{\frac{E_1 M_1 M_3 M_4\,[\,E_1 M_2 - E^*(M_1+M_2)]}{(M_3+M_4)(M_1+M_2)}}\;\cos\Phi + \frac{M_3 M_1 E_1}{(M_1+M_2)}\right]$$

Equation 17 is the general relation for the kinetic energy of any reaction product of an inelastic interaction where the nonrelativistic approximation is valid. For inelastic scattering of neutrons, Equation 17 reduces to

$$E_3 = \frac{E_1}{(A+1)}\left[A-1 - \frac{E^* A}{E_1} + \frac{2}{(A+1)}\left\{\sqrt{\frac{A[\,E_1 A - E^*(A+1)]}{E_1}}\;\cos\Phi + 1\right\}\right] \tag{18}$$

where A is the mass number of the target nucleus. The general nonrelativistic expression for the angle of emission of particle three in the lab system may be derived from Equations 11 and 16, and it is

$$\cos\theta = \sqrt{\frac{M_4[\,E_1 M_2 - E^*(M_1+M_2)]}{E_3(M_3+M_4)(M_1+M_2)}}\;\cos\Phi + \frac{M_3}{(M_1+M_2)}\sqrt{\frac{M_1 E_1}{M_3 E_3}} \tag{19}$$

For the case of inelastic scattering of neutrons, Equation 19 reduces to

$$\cos\theta = \frac{\cos\Phi}{(A+1)}\sqrt{\frac{A[\,E_1 A - E^*(A+1)]}{E_3}} + \frac{1}{(A+1)}\sqrt{\frac{E_1}{E_3}} \tag{20}$$

If the center-of-mass energy of the scattered neutron E_3' is selected from the appropriate probability density function, the excitation energy E^* may be calculated from Equation 4 because

$$E_1' = \left(\frac{A}{A+1}\right)^2 E_1$$

$$E_2' = \frac{E_1}{A}$$

and

$$E_4' = \frac{E_3'}{A}$$

Therefore,

$$E^* = \frac{(A+1)}{A}\,(E_1' - E_3') \tag{21}$$

Then if the center-of-mass scattering angle Φ is selected from its probability density function, the energy E_3 and angle θ of the scattered neutron in the laboratory system may be obtained from Equations 18 and 20, respectively. Alternately, $\cos\theta$ may be calculated from the less cumbersome expression

$$\cos\theta = \cos\Phi \sqrt{\frac{E_3'}{E_3}} + \frac{1}{(A+1)} \sqrt{\frac{E_1}{E_3}} \tag{22}$$

APPENDIX C

DERIVATION OF DIRECTION COSINES IN THE LABORATORY SYSTEM FOR INELASTICALLY SCATTERED NEUTRONS

The neutron transport code O5R keeps track of the direction of travel of each neutron by carrying in a data file the three direction cosines in the laboratory system of Cartesian coordinates. Inelastic scattering is assumed to be isotropic in the center-of-mass system, and a transformation must be made from the original laboratory direction cosines to the corresponding center-of-mass direction cosines. A scattering angle is then selected and the proper laboratory direction cosines are calculated.

These transformations involve a rotation about two coordinate axes as follows. Consider a unit vector defined by direction cosines (x,y,z). This vector, which corresponds to the original direction of the neutron, is defined in the center-of-mass system by the direction cosines (x',y',z'). Because vectors are fixed in their phase space independently of the reference coordinate system

$$x\hat{i} + y\hat{j} + z\hat{k} = x'\hat{i}' + y'\hat{j}' + z'\hat{k}' \qquad (1)$$

Or any vector A may be defined by the expression

$$\bar{A} = (\bar{A}\cdot\hat{i})\,\hat{i} + (\bar{A}\cdot\hat{j})\,\hat{j} + (\bar{A}\cdot\hat{k})\,\hat{k} \qquad (2)$$

Let $\bar{A} = \hat{i}', \hat{j}', \hat{k}'$. Then

$$\hat{i}' = (\hat{i}'\cdot\hat{i})\,\hat{i} + (\hat{i}'\cdot\hat{j})\,\hat{j} + (\hat{i}'\cdot\hat{k})\,\hat{k} \qquad (3)$$

$$= L_{11}\,\hat{i} + L_{12}\,\hat{j} + L_{13}\,\hat{k}$$

$$\hat{j}' = (\hat{j}'\cdot\hat{i})\,\hat{i} + (\hat{j}'\cdot\hat{j})\,\hat{j} + (\hat{j}'\cdot\hat{k})\,\hat{k}$$

$$= L_{21}\,\hat{i} + L_{22}\,\hat{j} + L_{23}\,\hat{k}$$

$$\hat{k}' = (\hat{k}'\cdot\hat{i})\,\hat{i} + (\hat{k}'\cdot\hat{j})\,\hat{j} + (\hat{k}'\cdot\hat{k})\,\hat{k}$$

$$= L_{31}\,\hat{i} + L_{32}\,\hat{j} + L_{33}\,\hat{k}$$

where L_{mn} are the cosines of the angles between vectors $\bar{m}$ in the prime system and $\bar{n}$ in the reference system. Substituting (3) into (1) and equating coefficients of $\hat{i}'$, $\hat{j}'$, and $\hat{k}'$ yields

$$x = L_{11}\,x' + L_{21}\,y' + L_{31}\,z' \qquad (4)$$

$$y = L_{12}\,x' + L_{22}\,y' + L_{32}\,z'$$

$$z = L_{13}\,x' + L_{23}\,y' + L_{33}\,z'$$

Or in matrix notation

$$\begin{vmatrix} L_{11} & L_{21} & L_{31} \\ L_{12} & L_{22} & L_{32} \\ L_{13} & L_{23} & L_{33} \end{vmatrix} \cdot \begin{vmatrix} x' \\ y' \\ z' \end{vmatrix} = \begin{vmatrix} x \\ y \\ z \end{vmatrix} \qquad (5)$$

In the current research the convention that is adopted is shown in Figure 46. The positive z' axis in the center-of-mass system is defined by the original neutron direction, and the x' axis is defined to be in the z--z' plane by a positive rotation about the z axis by the

angle Φ followed by a positive rotation by the angle θ about the y' axis. The cosines relating the lab and center-of-mass coordinate systems are

$$
\begin{aligned}
L_{11} &= \cos\theta\cos\Phi = L_{33}\cos\Phi = L_{33}L_{22} \\
L_{21} &= -\sin\Phi = -L_{32}/R \\
L_{31} &= \sin\theta\cos\Phi = L_{31} \\
L_{12} &= \cos\theta\sin\Phi = L_{33}\sin\Phi = L_{33}L_{32}/R \\
L_{22} &= \cos\Phi = L_{31}/R \\
L_{32} &= \sin\theta\sin\Phi = L_{32} \\
L_{13} &= -\sin\theta = -R \\
L_{23} &= 0 = 0 \\
L_{33} &= \cos\theta = L_{33}
\end{aligned}
\tag{6}
$$

where $R = \sqrt{|1 - L_{33}^2|} = \sin\theta$.

A new direction is chosen for the neutron by selection of: 1) a random asmuthal angle ψ which is distributed uniformly on the interval $(0,2\pi)$, and 2) a random polar angle α whose cosine is uniformly distributed on the interval $(-1,1)$(see Figure 47). Then the direction of the scattered neutron in the center-of-mass system is x',y',z' where

$$
\begin{aligned}
x' &= \sin\alpha\cos\psi \\
y' &= \sin\alpha\sin\psi \\
z' &= \cos\alpha
\end{aligned}
\tag{7}
$$

Conversion of this unit vector back to the lab system follows from the substitution of Equations 7 into Equations 4

$$x = L_{33}\, L_{22}\, x' - L_{22}\, y' + L_{31}\, z' \qquad (8)$$

$$y = L_{33}\, L_{32}\, x' / R + L_{31}\, y' / R + L_{32}\, z'$$

$$z = -L_{33}\, x' + L_{33}\, z'$$

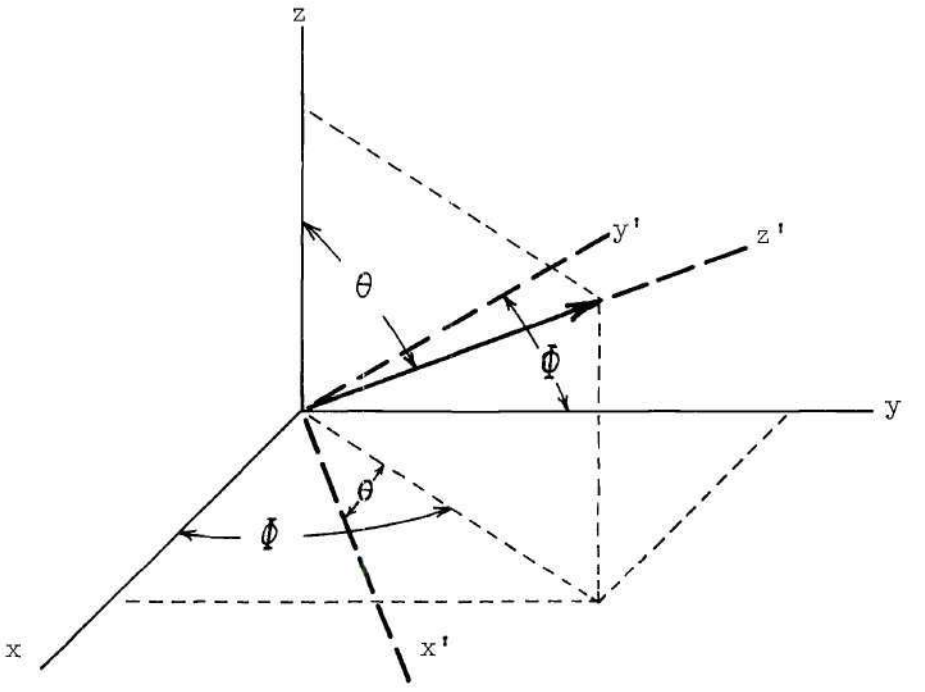

Figure 46. Coordinate System for Neutron Scattering

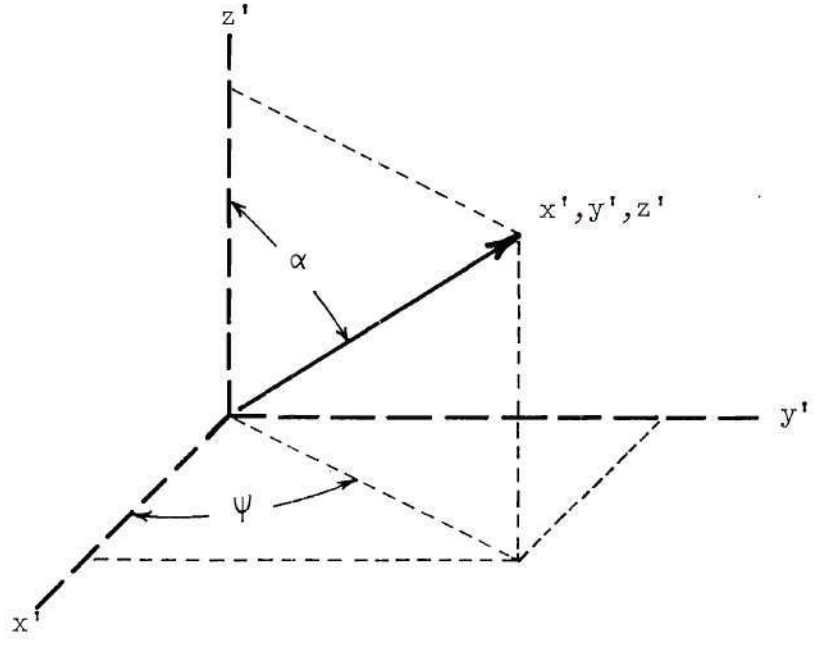

Figure 47. Coordinate System for Neutron Scattering

APPENDIX D

EQUATIONS FOR THE MATHEMATICAL DESCRIPTION OF HUMAN CHEST CROSS SECTION

The mathematical description of the chest model requires 18 equations of lines in the X-Y plane. The general form of these equations is

$$C_1x^2 = C_2y^2 + C_3xy + C_4x + C_5y + C_6 = 0$$

Because many of the lines intersect, only part of the locus of each equation may be required for the definition. Table 10 gives the parameters C_i for each of the 18 lines (see Figures 36 and 37).

Table 10. Coefficients for the Quadric Equations Presented in Figures 36 and 37

#	Coefficients					
	C_1	C_2	C_3	C_4	C_5	C_6
1				4.32	- 1.0	69.25
2				- 4.32	- 1.0	69.25
3	252.8	252.8			-5056.	- 38632.
4	353.4	353.4		-2121.	-3393.	-113596.
5	353.4	353.4		2121.	-3393.	-113596.
6	252.8	252.8			-5056.	- 38632.
7	67.24	25.0		941.4	- 485.0	3966.
8	72.25	28.09		- 895.9	- 573.0	3670.
9	23.23	35.81	3.113	49.02	-1004.	6295.
10	0.49	6.25			- 241.3	2325.
11	9.0	9.0			- 68.40	48.96
12	0.64	2.56			- 14.85	19.89
13	81.0	33.64		1134.	- 652.6	4409.
14	86.49	37.21		-1072.	- 759.1	3978.
15	176.9	176.9		6934.	-1344.	39218.
16	176.9	176.9		-6934.	-1344.	39218.
17					1.0	
18				1.0		- 20.0

BIBLIOGRAPHY*

1. W. C. Röntgen, "On a New Kind of Rays," Sitzgsber. Physik.-Med. Ges. Würzburg 137 (December, 1895).

2. O. Glasser, Wilhelm Conrad Röntgen and the Early History of the Roentgen Rays, Thomas Publishers, Springfield, 1934.

3. J. MacIntyre, Archives of Skiagraphy 1, 31 (1897).

4. J. B. Hamilton, "The Roentgen Rays," an editorial, J. Am. Med. Assoc. 26, 336 (1896).

5. H. Becquerel, "Sur les Radiations Émises par Phosphorescence," Compt. rend. 122, 420 (1896).

6. R. F. Mehl, "Nondestructive Testing by Gamma Rays," J. Am. Soc. Nav. Engrs. 43, 371 (1931).

7. H. T. Russell, "Reactor Production of ^{109}Cd: Isotopic Composition and Use as an X-ray Source," Nuclear Applications 1/2, 151 (1965).

8. Modern Developments in Electron Microscopy, B. M. Siegel, ed., Academic Press, New York, 1964.

9. J.-J. Trillat, Exploring the Structure of Matter, Interscience Publishers, New York, 1959.

10. A. M. Koehler, "Proton Radiography," Science 160, 303 (1968).

11. R. A. Bell and P. J. Clements, "A Non-Destructive Measurement of the Fluctuations in Area Density of a Graphite Block Using a 147 MeV Proton Beam," U.K.A.E.A. Report AERE-5732 (1968).

12. H. Kallmann, "Neutron Radiography," Research 1, 254 (1948).

13. O. Peter, "Neutronen-Durchleuchtung," Z. Naturforsch. 1, 557 (1946).

14. J. Thewlis, "Neutron Radiography," Brit. J. Appl. Phys. 7, 345 (1956).

---

*Abbreviations used herein follow the form of the Style Manual of the American Institute of Physics, 1959 Edition.

BIBLIOGRAPHY (Continued)

15. H. Berger, Argonne National Laboratory Report ANL-6346 (1960).

16. H. V. Watts, "Research on Neutron Interactions in Matter as Related to Image Formation," Armour Research Foundation Report ARF-1164-6 (1960).

17. M. Radwan and D. Sikorska, Conference on Nondestructive Methods of Material Testing, Warsaw, 1961 (Unpublished).

18. M. A. Greenfield and R. L. Koontz, "The Design Basis for Pinhole Gamma-Ray Cameras," Nuclear Applications 2, 415 (1966).

19. H. Berger, Neutron Radiography, Elsevier Publishing Company, New York, 1965.

20. H. L. Atkins, "Biological Applications of Neutron Radiography," Materials Evaluation 23, 453 (1965).

21. M. Brown and P. B. Parks, "Neutron Radiography in Biological Media; Techniques, Observations, and Implications," Am. J. Roent. 106 (3), 472 (1969).

22. M. Brown, J. J. Allen, and P. B. Parks, "Slow Neutron Imaging of Fatty Tissues Through Deuteration with Heavy Water," Biomedical Sciences Instrumentation, Volume 6, F. D. Thomas and E. E. Sellers eds., Instrument Society of America, Pittsburgh, 1968, p. 98.

23. J. P. Barton, "Neutron Radiography Using a Crystal Monochromator," J. Sci. Instr. 42, 540 (1965).

24. A. R. Spowart, "The Advantages of Epicadmium Neutron Beams in Neutron Radiography," Non-destructive Testing 1, 151 (1968).

25. J. P. Barton, "Radiographic Examination Through Steel Using Cold Neutrons," Brit. J. Appl. Phys. 16, 1833 (1965).

26. E. L. Criscuolo and D. Polansky, "Fast Neutron Radiography," U. S. Naval Ammunition Depot Report AD-275297 (1961).

27. J. Anderson, S. B. Osborn, and R. W. S. Tomlinson, "Neutron Radiography in Man," Brit. J. Radiol. 37, 957 (1964).

28. E. Tochilin, "Photographic Detection of Fast Neutrons: Application to Neutron Radiography," Phys. Med. Biol. 10, 477 (1965).

29. D. E. Wood, "Fast-Neutron Radiography with a Neutron Generator," Am. Nucl. Soc. Trans. 10, 443 (1967).

BIBLIOGRAPHY (Continued)

30. P. B. Parks, M. Brown, and D. S. Harmer, "Problems of Fast Neutron Radiography," Biomedical Sciences Instrumentation, Volume 6, F. D. Thomas and E. E. Sellers eds., Instrument Society of America, Pittsburgh, 1968, p. 118.

31. J. T. Brennan, "Fast Neutrons for Radiation Therapy," Radiologic Clinics of North America 7, 365 (1969).

32. P. Corompt, "Possibilites des Sources Mobiles en Neutrographie," Centre d'Etudes Nucleaires de Saclay Report DR/SAR/67-1, Saclay (1966).

33. E. A. Burrill and M. H. MacGregor, "Neutrons from Accelerators," Nucleonics 18, 64 (1960).

34. B. T. Feld, "The Neutron," Experimental Nuclear Physics, Volume 2, E. Segrè ed., John Wiley and Sons, Inc., New York, 1953, p. 361.

35. A. O. Hanson, R. B. Duffield, J. D. Knight, B. C. Diven, and H. Palevsky, "Thresholds for Photo-Neutron Reactions in Mn, Zn, Mo, Cd, Pr, Nd, Au, Hg, Tl, and Pb," Phys. Rev. 76, 578 (1949).

36. W. C. Reinig, "Advantages and Applications of ^{252}Cf as a Neutron Source," Nuclear Applications 5, 24 (1968).

37. J. P. Nichols, "Design Data for ^{252}Cf Neutron Source Experiments," Nuclear Applications 4, 382 (1968).

38. G. T. Seaborg, "Californium-252: Radioisotope with a Future," Californium-252, Proceedings of a Symposium Sponsored by the New York Metropolitan Section of the American Nuclear Society, October 22, 1968, New York, J. J. Barker ed., U.S.A.E.C. Report CONF-68 1032, 1969, p. 6.

39. R. Booth, "Rotating Neutron Target System," Lawrence Radiation Laboratory Preprint UCRL-70183 (1968).

40. D. Greene and R. L. Thomas, "An Experimental Unit for Fast Neutron Radiotherapy," Brit. J. Radiol. 41, 455 (1968).

41. "Californium-252 Progress, No. 2, " U.S.A.E.C. Savannah River Operations Office Publication, Aiken (1970).

42. E. A. Straker, "Fast-Neutron Collimator Studies. The TSF-SNAP Core Mapping Collimator," Nuclear Applications 6, 168 (1969).

BIBLIOGRAPHY (Continued)

43. R. C. Lawson and D. E. Watt, "The LET Distribution of the Recoil Proton Dose from DD and DT Neutrons," Phys. Med. Biol. 12, 217 (1967).

44. L. Rosen and L. Stewart, "Neutron Emission Probabilities from the Interaction of 14-MeV Neutrons with Be, Ta, and Bi," Phys. Rev. 107, 824 (1957).

45. H. Schober, "The Influence of Shannon's Information Theory on Definition and Measurement of Image Quality," The Reduction of Patient Dose by Diagnostic Radiologic Instrumentation, R. D. Mosely and J. H. Rust eds., Thomas Publishers, Springfield, 1969, p. 237.

46. H. Q. Woodard, "The Elementary Composition of Human Cortical Bone," Health Physics 8, 513 (1962).

47. G. W. Grodstein, "X-ray Attenuation Coefficients From 10 keV to 100 MeV," National Bureau of Standards Circular 583 (1957).

48. National Bureau of Standards Handbook 85, "Physical Aspects of Irradiations," Washington (1964).

49. J. E. Turner, "Calculation of Radiation Dose from Protons to 400 MeV," Health Physics 10, 783 (1964).

50. J. B. Birks, The Theory and Practice of Scintillation Counting, Macmillan Book Company, New York, 1964.

51. S. Pretre, E. Tochilin, and N. Goldstein, "A Standardized Method for Making Neutron Fluence Measurements by Fission Fragment Tracks in Plastics," U. S. Naval Radiological Defense Laboratory Report USNRDL-TR-1089 (1966).

52. M. M. Ter-Pogossian, The Physical Aspects of Diagnostic Radiology, Harper and Row Publishers, New York, 1967.

53. P. B. Parks, Private Communication, Savannah River Laboratory (1970).

54. K. Rossmann, "Image-Forming Quality of Radiographic Screen-Film Systems: Line-Spread Function," Am. J. Roent. 87, 387 (1962).

55. F. H. Perrin, "Methods of Appraising Photographic Systems Part I -- Historical Review," J. Soc. Motion Picture Engrs. 69, 151 (1960).

BIBLIOGRAPHY (Continued)

56. M. J. Feaver, "The Measurement of Radiograph Image Quality," Non-Dest. Test. 1, 173 (1968).

57. F. H. Perrin, "Methods of Appraising Photographic Systems Part II -- Manipulation and Significance of the Sine-Wave Response Function," J. Soc. Motion Picture Engrs. 69, 239 (1960).

58. R. H. Morgan, "The Frequency Response Function: Valuable Means of Expressing Informational Recording Capability of Diagnostic X-ray Systems," Am. J. Roent. 88, 175 (1962).

59. R. H. Morgan, "The Frequency Response Function," Am. J. Roent. 87, 387 (1962).

60. R. H. Morgan, L. M. Bates, U. V. Gopalarao, and A. Marinaro, "The Frequency Response Characteristics of X-ray Films and Screens," Am. J. Roent. 92, 426 (1964).

61. K. Rossmann, "Measurement of the Modulation Transfer Function of Radiographic Systems Containing Fluorescent Screens," Presented at the meeting of the American Association of Physicists in Medicine, Chicago, November, 1964.

62. K. Rossmann and G. Sanderson, "Validity of the Modulation Transfer Function of Radiographic Screen-Film Systems Measured by the Slit Method," Phys. Med. Biol. 13, 259 (1968).

63. K. F. Hansen, "Techniques for Nuclear Shielding Calculations," The Mitre Corporation Report ESD-TDR-63-231 (1963).

64. J. R. Lamarsh, Introduction to Nuclear Reactor Theory, Addison-Wesley Publishing Company, Reading, 1966.

65. J. J. Fitzgerald, G. L. Brownell, and F. J. Mahoney, Mathematical Theory of Radiation Dosimetry, Gordon and Breach Science Publishers, New York, 1968.

66. H. Goldstein, "The Attenuation of Gamma Rays and Neutrons in Reactor Shields," Superintendent of Documents, U. S. Government Printing Office, Washington (1957).

67. A. M. Weinberg and E. P. Wigner, The Physical Theory of Neutron Chain Reactors, University of Chicago Press, Chicago, 1968, p. 104.

68. H. Kahn, "Applications of Monte Carlo," Rand Corporation Report AECU-3259, Santa Monica (1956).

BIBLIOGRAPHY (Continued)

69. H. Kahn, "Use of Different Monte Carlo Sampling Techniques," Symposium on Monte Carlo Methods, H. A. Meyer ed., John Wiley and Sons, New York, 1956.

70. H. Kahn, "Multiple Quadrature by Monte Carlo Methods," Mathematical Methods for Digital Computers, Volume I, A. Ralston and H. S. Wilf eds., John Wiley and Sons, New York, 1967, p. 249.

71. D. C. Irving, R. M. Freestone, Jr., and F. B. K. Kam, "05R, A General-Purpose Monte Carlo Neutron Transport Code," Oak Ridge National Laboratory Report ORNL-3622 (1965).

72. S. G. Buccino, C. E. Hollandsworth, H. W. Lewis, and P. R. Bevington, "Inelastic Scattering of Neutrons from Medium and Heavy Nuclei," Nuclear Physics 60, 17 (1964).

73. J. M. Blatt and V. F. Weisskopf, Theoretical Nuclear Physics, John Wiley and Sons, New York, 1952.

74. W. Houser and H. Feshbach, "The Inelastic Scattering of Neutrons," Phys. Rev. 87, 366 (1952).

75. J. B. Singletary and D. E. Wood, "Scattering of 14-MeV Neutrons by Carbon," Phys. Rev. 114, 1595 (1959).

76. National Bureau of Standards Handbook 63, "Protection Against Neutron Radiation up to 30 Million Electron Volts," Washington (1957).

77. C. T. Brown, Private Communication, Advanced Research Corporation, Atlanta (1969).

78. J. B. Birks and F. A. Black, "Deterioration of Anthracene under α-Particle Irradiation," Proc. Phys. Soc. (London) A64, 511 (1951).

79. J. R. Prescott and A. S. Rupall, "The Specific Fluorescence of Plastic Scintillator NE-102," Can. J. Phys. 39, 221 (1961).

80. T. J. Gooding and H. G. Pugh, "The Response of Plastic Scintillators to High-Energy Particles," Nucl. Instr. Meth. 7, 189 (1960).

81. T. N. E. Greville, "Spline Functions, Interpolation, and Numerical Quadrature," Mathematical Methods for Digital Computers, Volume II, A. Ralston and H. S. Wilf eds., John Wiley and Sons, New York, 1967, p. 156.

BIBLIOGRAPHY (Concluded)

82. M. R. Raju, J. T. Lyman, T. Brustad, and C. A. Tobias, "Heavy Charged-Particle Beam," Radiation Dosimetry, Second Edition, Volume III, F. H. Attix and E. Tochilin eds., Academic Press, New York, 1969, p. 151.

83. W. S. Snyder, Private Communication, Oak Ridge National Laboratory (1969).

84. E. Tochilin and B. W. Shumway, "Dosimetry of Neutrons and Mixed n + γ Fields," Radiation Dosimetry, Second Edition, Volume III, F. H. Attix and E. Tochilin eds., Academic Press, New York, 1969, p. 255.

85. A. C. Eycleshymer and D. M. Schoemaker, A Cross-Section Anatomy, Appleton-Century-Crofts, Inc., New York, 1938, p. 131.

86. G. Friedlander, J. W. Kennedy, and J. M. Miller, Nuclear and Radiochemistry, Second Edition, John Wiley and Sons, New York, 1964, p. 98.

87. W. H. Barkas, Nuclear Research Emulsions, New York, Academic Press, 1963, p. 438.

88. J. T. Brennan, Private Communication, University of Pennsylvania (1970).

89. E. J. Sternglass and E. L. Keller, "High Resolution Electronic Gamma-Ray Imaging," Advances in Dynamic Radioactive Scanning, Y. Wang ed., Thomas Publishers, Springfield, 1968, p. 44.

90. Radiation Shielding Information Center, Private Communication, Oak Ridge National Laboratory (1968).

91. H. E. Johns, The Physics of Radiology, Thomas Publishers, Springfield, 1964, p. 703.

92. M. Brown, Private Communication, Medical College of Georgia (1969).

93. J. P. Barton, "Some Possibilities of Neutron Radiography," Phys. Med. Biol. 9, 33 (1964).

VITA

William Howard Wilkie, Jr. is a native of Asheville, North Carolina. He received the B.S. Degree in Engineering Mathematics, with High Honors, from North Carolina State University in 1960 and the M.S. Degree in Physics from Vanderbilt University in 1964.

Between the years 1962 and 1967, Mr. Wilkie was employed as a Research Associate in the Health Physics Division of Oak Ridge National Laboratory, Oak Ridge, Tennessee. He was primarily engaged in applied research in the general area of internal and external radiation dosimetry. His publications include:

"Measurement of Spectral Distribution of Positron Flux in an Infinite Copper Medium Containing Cu^{64}," Phys. Rev. 135, A1133 (1964)(with R. D. Birkhoff).

"Environmental Studies: Radiological Significance of Nuclear Rocket Debris," U.S.A.E.C. Reports ORNL-TM-1053 (1965), ORNL-TM-1159 (1966), ORNL-TM-1686 (1966)(with others).

"Scintillation Extrapolation Dosimetry of Small Beta-Emitting Sources," Solid State and Chemical Radiation Dosimetry in Medicine and Biology, IAEA, Vienna, 1967, p. 407 (with B. R. Fish).

"Theoretical Modulation Transfer Functions and Dosimetry of Fast-Neutron Radiography," Biomedical Sciences Instrumentation, Volume 6, F. D. Thomas and E. E. Sellers eds., Instrument Society of America, Pittsburgh, 1969, p. 127 (with D. S. Harmer).

Mr. Wilkie was certified in 1968 by the American Board of Health Physics and is a member of the Health Physics Society, the American Nuclear Society, and Sigma Xi. He is married to the former Mary Reynolds of Brevard, North Carolina, and has two sons, Keats and Timothy.